Electrochemical Investigation of Thin Nickel, Copper and Silver Films Interfaced with Yttria-Stabilized Zirconia

By

Michèle A. Fee

A thesis submitted to the Faculty of Graduate and Postdoctoral Studies in partial fulfillment of the requirements for the degree of

Master of Applied Science

In

Department of Biological and Chemical Engineering

Faculty of Engineering

University of Ottawa

Résumé

L'étude électrochimique de films minces de nickel, de cuivre et d'argent en contact intime avec l'oxyde de zirconium dopé à l'oxyde de yttrium (YSZ) a été faite afin de déterminer leur réaction à la polarisation électronique en milieu dilué en oxygène à 350 °C et leur viabilité pour la promotion électrochimique de catalyseurs (EPOC). Des disques polycristallines d'YSZ (8 mol % Y_2O_3-ZrO_2) ont été synthétisées en laboratoire sur lesquelles les films ont été déposés par évaporation sous vide (PVD). L'épaisseur critique de ces films sur l'YSZ a été déterminée *in-situ* en mesurant leur résistance. Par la suite, des films de 50 et 100 nm en cuivre et en nickel ont été étudiés en utilisant la voltamétrie cyclique d'électrolyte solide (SECV). Puisque les films d'argent de telle épaisseur sont instables, un film de 800 nm a été utilisé pour cette étude. Ces matériaux répondent différemment à la polarisation et forment des oxydes selon les modèles de Wagner et Mott-Cabrera.

Abstract

The electrochemical investigation of nickel, copper and silver thin films interfaced with yttria stabilized zirconia (YSZ) solid electrolyte was accomplished to determine their response to polarization in dilute oxygen environments at 350 °C and assess their viability for electrochemical promotion of catalysis (EPOC). Polycrystalline YSZ (8 mol % Y_2O_3-ZrO_2) pellets were synthesized in the lab and films deposited onto them using evaporative physical vapor deposition (PVD). The critical thickness of copper, silver and nickel thin films were foundusing *in-situ* resistance measurements. Following this, 50 and 100 nm copper and nickel films were studied using solid electrolyte cyclic voltammetry (SECV) to determine their response to polarization. Given that silver thin films at such thicknesses are thermally unstable, a film of 800 nm was used in this study. The materials were found to respond to polarization in different ways, forming oxides according to Wagner and Mott-Cabrera oxidation models.

Acknowledgements

Firstly, I would like to thank my supervisors, Dr. Elena Baranova and Dr. Arnaud Weck, for their patience, guidance and for allowing me to pursue this research despite the many obstacles.

Secondly, I would like to thank my friends Holly, Pat, Sarah, Jamie and Dom, for the lunches, the travels, the walks, the drives, the movies and drinks and dinners. Also, thank you for scrapping me off the floor when I didn't think I could take it anymore.

Thirdly, I would like to thank many my lab-mates for being helpful, supportive, patient and edifying: Holly, Paul, Max, Rima, Evans, Audrey, Andrew, Spy, Anis, Yaser, Mishaal, Marina, Elisa, Mahyar, Yanick, Patrick. Particular thanks go to Yannick for training me on the evaporator and to Holly for all those whiteboard discussions.

Fourthly, I would like to thank Louis, Gerard, Franco and Leo for their technical support.

Fiftly, I would like to thank Francine and Sylvie, without whom, my project would have been so much harder.

Sixthly, I would like to thank the Yun Liu for SEM training and Sander Mommmers for XPS results.

Lastly, I would like to thank my family.

Table of Contents

List of Figures

Chapter 2

Chapter 3

Chapter 4

Chapter 5

Chapter 6

Chapter 7

List of Symbols

Symbol	Designation	Unit(s)
A	Surface area	m^2, cm^2
A_1	Logarithmic oxidation rate constant	-
A_C	Area projected onto sphere of equal mass-flux	cm^2
A_S	Surface area of deposit	cm^2
A_V	Amplitude of electrical potential oscillation in AC current	mV, V
A_i	Amplitude of current oscillation in AC current	mA, A
a_i	Activity of species i	-
B_1, B_2	Logarithmic oxidation rate constants	-
C_i	Concentration of species i	$mol.cm^{-3}$
C	Capacitance	F
CE	Counter electrode	-
D_i	Diffusion coefficient	$cm^2.s^{-1}$
d	Diameter of gas particle	nm
E_{Diff}	Free energy of diffusion	$J.mol^{-1}$
E_F	Fermi level	-
E_i	Initial potential of cyclic voltammetry scan	mV, V
E_p	Peak electrochemical potential	V
E_s	Switching potential of cyclic voltammetry scan	mV, V
e	Charge of an electron	$C.mol^{-1}$
F	Faraday's constant, 96 485	$C.mol^{-1}$
ΔG^*	Gibbs free energy of formation of smallest stable nuclei	J
ΔG_v	Gibbs free energy of formation per unit volume condensed material	$J.cm^{-3}$
ΔG_i^0	Standard Gibbs energy of formation of species i	J.mol
ΔH_f^0	Standard enthalpy of formation	$kJ.mol^{-1}$
I	Current	mA, A
i_o	Exchange current density	$\mu A.cm^{-2}$
i_p	Peak current density	$\mu A.cm^{-2}$
i	Current density	$\mu A.cm^{-2}$
J_i	Molar flux of species i	$mol.cm^3$
k_B	Boltzmann constant, 1.38×10^{-23}	$J.K^{-1}$
k	Reaction rate constant	-
l_{tpb}	Three phase boundary length	m.cm-2
M	Molar Mass	$g.mol^{-1}$
ME	Metal electrode material (silver, nickel or copper)	-
$\bar{M}_C$	Mass deposited	g
N^*	Density of stable nuclei	$nuclei.cm^2$
N_A	Avogadro's constant, $6.02x10^{23}$	$atoms.mol^{-1}$
N_G	Electrode-gas interface atoms	mol

Symbol	Designation	Unit (s)
N_M	Surface metal concentration	mol.m^{-2}
n_s	Density of total available nucleation sites	nuclei.cm^{-2}
$P_{O_2,R}$	Partial pressure of oxygen at the reference electrode	kPa
$P_{O_2,W}$	Partial pressure of oxygen at the working electrode	kPa
P_{O_2}	Partial pressure of oxygen	kPa
P_H	chamber pressure	mBar
P_j	Average dipole moment	Debye
p_c	Percolation threshold	-
Q_i	Charge density of process i	µC.cm^{-2}
R_i	Resistance of component i	Ω
$R^{\cdot}$	Deposition rate	mol.s^{-1}
RE	Reference electrode	-
r^*	Radius of smallest stable nuclei	nm
r_0	Open circuit reaction rate	mol.s^{-1}
r_f	Faradaic reaction rate	mol.s^{-1}
r	Promoted reaction rate	mol.s^{-1}
Δr	Change in reaction rate with electrochemical promotion	mol.s^{-1}
T	Gas phase temperature	°C
T_m	Melting point temperature	K
t_H	Hold time	s
V_{WR}	Applied potential between reference and working electrode	V
V_{WR}^0	Open circuit potential	V
WE	Working electrode	-
X	Reactance	Ω
X_i	Catalytic convertion	-
x	Thickness	-
Z_f	Impedance of faradaic process	Ω
Z_i	Impedance of component i	-
Z'	Real component of impedance	Ω
Z''	Imaginary component of impedance	Ω
z	Number of electrons transferred in an electrochemical potential	-

Greek Symbols

Symbol	Designation	Unit (s)
α	Electrophobicity of promoted reactions	-
α_C , α_a	symmetry coefficient for cathodic and anodic charge transfer	-
α_E	Coefficient of evaporation	-
Γ_E	Rate of evaporation	g.s^{-1}
γ_{ij}	Surface tension of i on j (where f=film, s=substrate, v=vapor)	

Symbol	Designation	Unit (s)
ε_o	Permittivity of free space, 8.85×10^{12}	$C.(J.m)^{-1}$
η	Overpotential	V
η_i	Faradaic efficiency of process i	%
θ	Wetting angle of deposit on substrate	degrees
Θ_j	Surface coverage of adsorbed species	-
Λ	Faradaic efficiency	-
λ	Mean free path	nm
μ_i	Chemical potential of component i	$J.mol^{-1}$
$\bar{\mu}_i$	Electrochemical potential of component i	$J.mol^{-1}$
ν	Scan rate	mV.s-1
ρ	Rate enhancement ratio	-
ρ_i	Density of component i (pellet, wire, YSZ)	-
ω_i	frequency of the current oscillation in AC current	Hz
ω_v	Frequency of electrical potential oscillation in AC current	Hz
τ	Time constant of promotion, 63% of full promotion	s
Φ	Work function of catalyst	eV
χ	Galvani potential or surface potential	$J.mol^{-1}$
ψ	Volta potential or outer potential	$J.mol^{-1}$

Chapter 1 Introduction

1.1 Aim of the Work

Metals interfaced with solid electrolyte have a variety of interesting characteristics which make them suitable for applications in catalysis and electrocatalysis. Strong metal support interactions (SMSI) are observed when certain metal catalysts interfaced with ionic conducting supports resulting in modifications or promotion of the catalyst behavior. The ionic conductivity of solid electrolytes when interfaced with the electronic conduction of the metals makes them ideal for electrochemical applications such as solid oxide fuel cells [1–4], oxygen sensors [5, 6], water electrolyzers [7], electrochemical promotion of catalysis (EPOC) [8–14]. This last implements catalyst-support interaction of SMSI in an electrochemical cell providing greater degree of control over the promotion of catalysts and is the focus of this report.

Noble metal films, such as Pt [15–20], Ru/RuO_2 [8, 21, 22], Rh [23–26], Ir/IrO_2 [27], Pd [28–31] are of particular interest in EPOC studies as they are thermally and chemically stable at high temperatures have high electronic conductivities and possess inherent catalytic activity for a variety of reactions. A variety of forms are used in these applications, such as metal pastes, cermets and thin films, each with morphological advantages and disadvantages. Investigation of the interface is favored by electrodes with simple well defined microstructure.

The use of solid electrolyte cyclic voltammetry (SECV) to diagnose EPOC systems was proposed by Vayenas *et al.* [32]. The theory behind the study of anodic and cathodic processes occuring at electrodes using this technique is well studied in aqueous electrochemistry, but has een carefully extended to include solid electrolyte systems. Models for the behavior of specific

electrodes using cyclic voltammetry have been performed for sputtered Pt [32–35], Pd [36] and Ni [37] films on yttria-stabilized zirconia (YSZ).

The following work aims to investigate the interface of silver, nickel and copper evaporatively deposited thin films interfaced with YSZ. The proposed models will build on the existing literature, using cyclic voltammetry techniques.

1.2 **References**

[1] J. Fleig, *Annu. Rev. Mater. Sci.,* 33, 361–382, (2003).

[2] W. Zhu, S. Deevi, *Mater. Sci. Eng. A*, 362, 228–239, (2003).

[3] R. Craciun, *J. Electrochem. Soc.*, 146, 4019, (1999).

[4] S. McIntosh, R. J. Gorte, *Chem. Rev.*, 104, 4845–65, (2004).

[5] J. Riegel, H. Neumann, H. Wiedenmann, *Solid State Ionics*, 153, 783–800, (2002).

[6] E. Shoemaker, M. Vogt, F. Dudek, *Solid State Ionics*, 92, 285–292, (1996).

[7] H. Iwahara, *Solid State Ionics*, 168, 299–310, (2004).

[8] S. Wodiunig, Electrochem. *Solid-State Lett.*, 2, 281, (1999).

[9] C. G. Vayenas, C. G. Koutsodontis, *J. Phys. Chem.,* 128, 182506, (2008).

[10] J. Nicole, D. Tsiplakides, C. Pliangos, X. E. Verykios, C. Comninellis, C. G. Vayenas, *J. Catal.,* 204, 23–34, (2001).

[11] C. G. Vayenas, G. E. Pitselis*, Ind. Eng. Chem. Res.*, 40, 4209–4215, (2001).

[12] A. Jaccoud, thesis, Ecole Polytechnique Federale de Lausanne (2007).

[13] A. Katsaounis, Z. Nikopoulou, X. E. Verykios, C. G. Vayenas, *J. Catal.,* 222, 192–206, (2004).

[14] R. Imbihl, *Prog. Surf. Sci.,* 85, 241–278, (2010).

[15] A. Lucas-Consuegra, F. Dorado, C. Jiménez-Borja, J. L. Valverde, *J. Appl. Electrochem.,* 38, 1151–1157, (2008).

[16] P. Vernoux, *J. Catal.*, 208, 412–421, (2002).

[17] A. Lintanf, *Solid State Ionics*, 178, 1998–2008, (2008).

[18] P. Vernoux, F. Gaillard, C. Lopez, E. Siebert, *J. Catal.*, 217, 203–208, (2003).

[19] D. Tsiplakides, S. Balomenou, A. Katsaounis, D. Archonta, C. Koutsodontis, C. G. Vayenas, *Catal. Today*, 100, 133–144, (2005).

[20] C. Koutsodontis, A. Katsaounis, J. C. Figueroa, C. Cavalca, C. Pereira, C. G. Vayenas, *Top. Catal.*, 39, 97–100, (2006).

[21] D. Theleritis, S. Souentie, a. Siokou, A. Katsaounis, C. G. Vayenas, *ACS Catal.*, 2, 770–780, (2012).

[22] I. Constantinou, I. Bolzonella, C. Pliangos, C. Comninellis, C. G. Vayenas, *Catal. Let.*, 100, 125–133, (2005).

[23] F. Williams, *Electrochim. Acta*, 47, 1259–1265, (2002).

[24] C. Pliangos, C. Raptis, T. Badas, C. G. Vayenas, *Solid State Ionics*, 136-137, 767–773, (2000).

[25] E. A. Baranova, A. Thursfield, S. Brosda, G. Fóti, C. Comninellis, C. G. Vayenas, *Catal. Let.,* 105, 15–21, (2005).

[26] S. Bebelis, H. Karasali, C. G. Vayenas*, J. Appl. Electrochem*., 38, 1127–1133, (2008).

[27] P. Vernoux, F. Gaillard, R. Karoum, A. Billard, *Appl. Catal. B.,* 73, 73–83, (2007).

[28] V. Roche, R. Karoum, A. Billard, R. Revel, P. Vernoux, *J. Appl. Electrochem.*, 38, 1111–1119, (2008).

[29] C. Jiménez-Borja, F. Dorado, A. de Lucas-Consuegra, J. M. G.-Vargas, J. L. Valverde, *Fuel Cells*, 11, 131–139, (2011).

[30] S. Bebelis, H. Karasali, C. G. Vayenas, *Solid State Ionics*, 179, 1391–1395, (2008).

[31] A. Katsaounis, *J. Appl. Electrochem*., 38, 1097–1110, (2008).

[32] C. G. Vayenas, A. Ioannides, S. Bebelis, *J. Catal.,* 67–87, (1991).

[33] A. Jaccoud, C. Falgairette, G. Foti, C. Comninellis, *Electrochim. Acta*, 52, 7927–7935, (2007).

[34] G. Fóti, A. Jaccoud, C. Falgairette, C. Comninellis, *J. Electroceram*., 23, 175–179, (2007).

[35] C. Falgairette, G. Fóti, *Catal. Today*, 146, 274–278, (2009).

[36] C. Jiménez-Borja, S. Souentie, J. González-Cobos, F. Dorado, J. L. Valverde, *J. Appl. Electrochem.,* 43, 417–424, (2013).

[37] S. Souentie, C. Falgairette, C. Comninellis*, J. Electrochem. Soc*., 157, P49, (2010).

Chapter 2 Literature Review

The aim of this chapter is to present the current progress in the field of thin metal films interfaced with yttria-stabilized zirconia (YSZ) as it relates to the electrochemical promotion of catalysis (EPOC) phenomenon. The review is presented in five parts. First, studies of the mechanism for backspillover phenomenon the mechanisms of electrochemical promotion as found in the literature are presented. Then, the studies of the O_2, Me/YSZ system are discussed with relation to application of cyclic voltammetry (CV) studies to develop models for the polarization of thin films. Third, the effect of electrode microscopy addressed. Then, the theory of crystal growth is covered with special attention to the impact of deposition parameters on film microstructure. Lastly, the research objectives for this report are presented based on gaps in the literature reviewed.

2.1 Introduction

The electrochemical investigation of thin films interfaced with solid electrolytes is of interest in the study of electrochemical promotion of catalysis (EPOC) also known as non-Faradaic modification of catalytic activity (NEMCA), which is the most recent and fast growing areas in heterogeneous catalysis [1]. Other applications include solid oxide fuel cell [2, 3], oxygen sensors [4], solid-electrolyte electrolyzers [5, 6], membrane reactors [7, 8].

Solid electrolytes, such as stabilized zirconias (eg, doped with calcia, yttria or scandia), β''-Al_2O_3, $Bi_2V_{1.9}Cu_{0.1}O_{5.35}$ (BICUVOX), $Ce_{1-x}Gd_xO_{2-\delta}$ (ceria-gadolinia, CGO), LSGM and $Na_3Zr_2Si_2PO_{12}$ (NASCON), are solids characterized by fast ion-conduction and low electronic conductivity [9–11]. These materials have gained recent popularity as catalyst supports due to

observed metal-support interactions (MSI) which modify the catalyst activity [1]. Electrochemically driven metal-support interactions have been studied in the form of electrochemical promotion of catalysts. With the application of small electrical potentials (ca. 2V) or low currents (ca. 10 μA) to an electrochemical cell, a pronounced and reversible modification of the catalytic performance is observed. This phenomenon is attributed to the backspillover of conducted species, such as O^{2-} from oxygen conductors, from the ionically conducting support onto the working electrode.

Investigation of this phenomenon using a variety of electrochemical and physical characterization techniques have been undertaken in the literature. The following aims to present the state of the art and provide a backdrop for the research presented in this work.

2.1.1 Metal Support Interactions (MSI) and Catalysis

In a chemical industrial process, the rate and selectivity of a reaction directly impacts the economics of the system. Catalysts are used to facilitate the reaction by providing a common location for the reactants and donating or withdrawing electron density thus lowering the activation energy, E_A, for the reaction. Heterogeneous catalysts have the added benefit of being in a different phase than the reaction species, facilitating its recovery and recycling.

Traditional heterogeneous catalysts consist of an active phase supported on an inexpensive, thermally and chemically stable support. The performance of the active phase is composition and structure-sensitive and can be modified by the use of promoters. Recent investigations have also shown interactions with supports to yield modifications in catalysts activity [1, 12].

The interaction between catalysts and adsorbed species is described by the work function, φ, of the catalysts, which is determined by the nature of the catalysts as well as its environment.

The work function of a metal is defined as the energy required to remove an electron from the Fermi level to a point directly outside the surface, generally accepted as a distance of 1 μm. The modification of work function through electrochemical promotion is discussed below.

Since only the work function is modified, it is important for these systems that the reaction rate not be diffusion limited. To avoid this, reaction species are well mixed and catalysts designed with open microsturctures ranging from microporous materials (pore diameter < 2 nm) to thin films. The availability of active sites to the reaction is given by the dispersion, which is expressed as the ratio of surface atoms to total atoms in the active phase and can range from 80% for supported nanoparticle [13] catalysts to 0.01% for thick films [14].

Strong Metal Support Interactions (SMSI)

Support materials were traditionally assumed to be inert, thermally stable materials with high specific surface area (>100 $m^2.g^{-1}$), such as carbon, silica and alumina. Tauster [12] observed a suppression of chemisorptive properties in group VII noble metal catalysts when supported on titanium dioxide [12]. This effect is found to exist in several catalyst and support systems when the support surface of a local anion deficiency resulting from partial reduction of the surface.

Several models have been developed to explain this strong metal support interaction (SMSI). Schwab [15] and Solymosi [16] proposed a model based on electronic interactions stemming from the metal-semiconductor boundary layer theory which states that the Fermi energy of two adjacent materials must be the same for thermodynamic equilibrium to be established [17]. As a result, the higher work function of the metal would be lowered via electron transfer to the metal in order to match that of the support [12].

Recent work by Vayenas *et al.* suggest an alternative model which links strong metal support interaction to electrochemical promotion of catalysis via the phenomenon of spillover-backspillover[17, 18]. Spillover is described as the mobility of a sorbed species from one phase on which they readily adsorb onto another where they do not directly adsorb. In the case of titania, metal support interactions result from the backspillover of O^{2-} onto the surface of the metallic catalyst clusters.

Electrochemical Promotion

The phenomenon of electrochemical promotion arose from research derived from the work of Wagner [19]. In 1970 Wagner proposed a method by which an oxygen conducting support could be used to measure the oxygen activity at a catalyst's surface [20]. For this technique, a porous catalyst working electrode and inert reference and counter electrode are deposited on either side of a solid electrolyte, with a cell of the form O_2 ,Au|YSZ|*Me*,$O_{2.}$ where Au is the counter electrode and *Me* the working electrode material.

When oxygen is adsorbed onto the working electrode, a measureable electrical potential is generated given by the Nernst equation for that system, given as the open circuit potential (OCV) in equation (2.1)

$$V^0_{WR} = \frac{RT}{4F} \ln\left(\frac{P_{O_2,W}}{P_{O_2,R}}\right) \qquad (2.1)$$

Where $P_{O2,W}$ and $P_{O2,\,R}$ are the partial pressure of air at the working and pseudo- reference electrodes respectively, R is gas constant (8.314 J.(mol K)$^{-1}$), T is the temperature (K) and F is Faraday's constant (96,485 C.mol^{-1}). The open circuit potential (OCV), $V^0{}_{WR}$ is a measure of the cell potential with no external applied potential or current.

In 1981, Vayenas and Stoukides proposed a similar cell, shown in Figure 2.1 in which the activity of O_2 adsorbed onto the surface of a silver catalyst could be controlled by applied electrical potential for the partial oxidation of ethylene [19, 21].

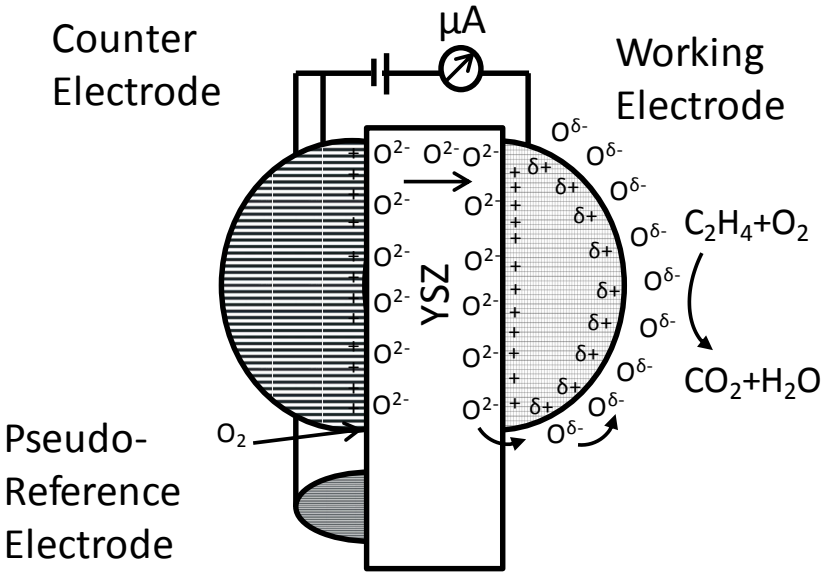

Figure 2.1.Electrochemical promotion catalyst cell configuration

When the reaction is charge transfer limited, the rate of oxygen supplied to the cathode, r_f, follows Faraday's law, shown by equation (2.2).

$$r_f = \frac{I}{4F} \tag{2.2}$$

where, I is the applied current (A).

Surprisingly, in this work performed by Vayenas *et al.* for the epoxidation reaction of ethylene and the rate of production greatly exceeded the Faradaic reaction rate [19, 21]. Figure 2.2 shows typical transient EPOC curve.

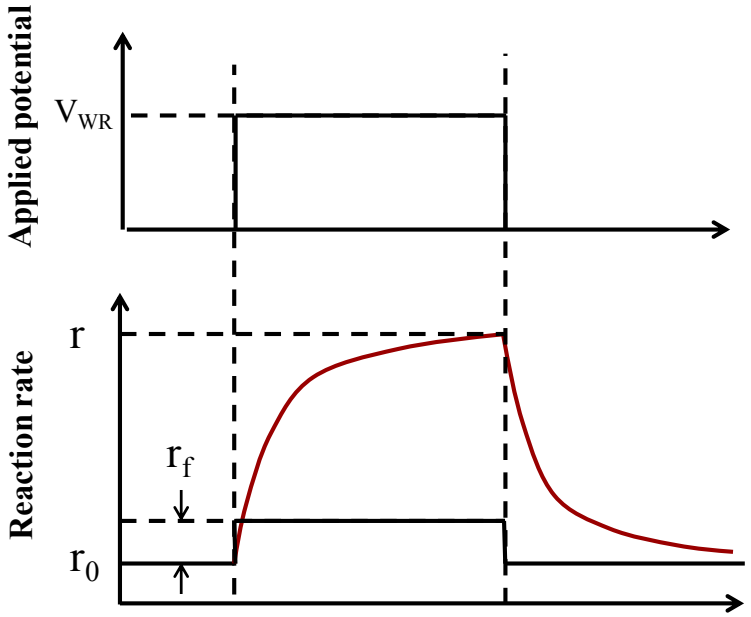

Figure 2.2 Typical EPOC transient

The open circuit reaction rate, r_o, is the reaction rate without external intervention. With application of small currents or small electrical potentials, the reaction rate increases to a value of r.

The phenomenon was referred to as non-faradaic modification of catalyst activity, or NEMCA, but later became known as electrochemical promotion of catalysts, or EPOC, as the mechanism was elucidated. Investigation of this effect was initially conducted with YSZ electrolyte and platinum catalyst paste and gold counter and reference electrodes, but the results were shown to be valid for a wide range of reaction systems [22–30]. These systems are characterized by the Faradaic efficiency and rate enhancement ratios.

The Faradaic efficiency is the degree to which the electrochemically promoted reaction rate exceeds that of the Faradaic reaction rate. Faradaic efficiencies are greater than 1 for electrochemically promoted system and lower than one for electrochemical systems.

$$\Lambda = \frac{\Delta r}{r_f} = \frac{r - r_0}{r_f} \tag{2.3}$$

where r_o is the open-circuit reaction rate, r the actual reaction rate and r_f the Faradaic reaction rate. The rate enhancement ratio is the relation between the open-circuit or unpromoted reaction rate, $r_{0,}$ to the reaction rate under applied potential, r, is shown in equation (2.4).

$$\rho = r/r_0 \tag{2.4}$$

The modification in reaction rate resulting from the change in work function varies exponentially according to equation (2.5) [9, 31]

$$\ln\left(\frac{r}{r_o}\right) = \frac{\alpha e(\Phi - \Phi^*)}{k_B T} \tag{2.5}$$

Where α and Φ* are system specific variables. α is positive for electrophobic reactions and negative for electrophilic reactions and Φ is the workfunction of the unpolarized catalyst [9].

The change in work function resulting from the polarization of the film dependent on the coverage of the promoting on the catalyst and can be calculated from the Helmholtz relation [9], as shown in equation (2.6).

$$\Delta\Phi = \frac{eN_M}{\varepsilon_o}\Delta(P_j\theta_j) \tag{2.6}$$

Where N_M is the surface metal concentration mol.m^{-2}, ε_o is the permittivity of free space 8.85x10^{12} C/Jm, P_j is the average dipole moment (typically 1 Debye) and θ_j is the coverage of the adsorbed species.

The mechanism responsible for this modification of catalytic behavior has been extensively studied in the literature [17, 18, 32–34] and has been linked to the spillover/backspillover of promoting species from the support onto the catalyst film.

The link between strong metal support interactions and electrochemical promotion was was confirmed by comparing the catalytic behavior of only IrO_2 (X_{IrO2}=1), pure titania (X_{IrO2}=0) as well as IrO_2 supported on TiO_2 were compared to values obtained through electrochemical promotion. Promotion of IrO_2 (ρ=12) samples were comparable to the results found for IrO_2-TiO_2, which could showed little ability for electrochemical promotion (ρ =2). This implies that a catalyst exhibiting SMSI already undergoes the phenomenon observed with the application of external current. Investigations by Vayenas *et al.* [17] confirm these results with surface characterization using x-ray photospectroscopy (XPS) to track changes in the O1s peak for each catalyst. Changes in the O1s peaks arising from application of current on the pure IrO_2 samples were consistent with those observed for unpromoted IrO_2. [17] This effective double layer is formed from the backspillover of oxygen species onto metal catalysts which can masking active significant portions of the catalyst, but also provide contact zones with enhanced catalytic properties. Metal atoms in these contact zones may grab oxygen atoms resulting in the formation of partially oxidized metal states and oxygen vacancies on the oxide surface, both of which may be used as active sites for the formation of specific products [35].

This mechanism is shown in Figure 2.3 for strong metal support interaction and electrochemical promotion (discussed below) and can result in the inhibition or enhancement of catalytic performance of the material, depending on the reaction system.

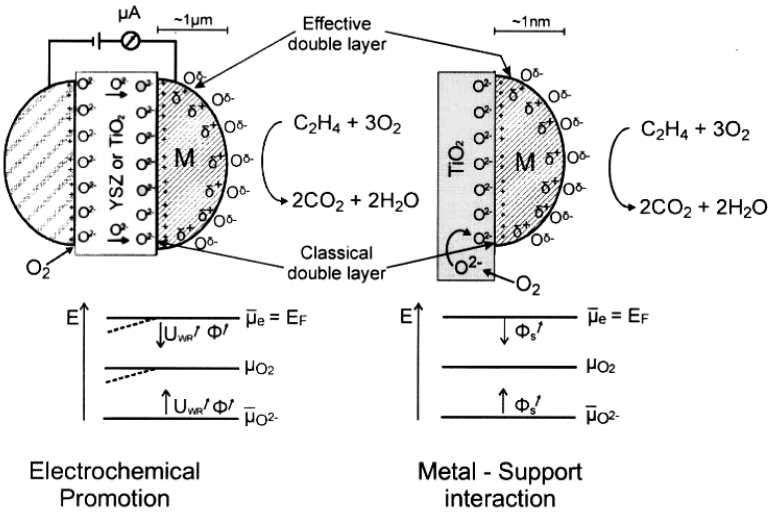

Figure 2.3 Strong metal support interaction and electrochemical promotion [18]

Mechanism

Upon application of a small potential or current to an electrochemical cell as shown in Figure 2.3, the following processes are thought to occur in the case of reduction of ethylene (C_2H_4) on Pt on YSZ.

At the counter electrode, oxygen in the gas stream diffuses to the three phase boundary (tpb) – the intersection of the anode, electrolyte and reaction gases where it is adsorbs, reduced to O^{2-} and transferred to the electrolyte according to equation (2.7)

$$O_2 \rightarrow 2O^{-2}_{YSZ} + 4e^- \qquad (2.7)$$

At the working electrode, three processes are possible with predictable effects on the reaction rate:

(i) Reduction of O^{2-} to O_2 and desorption into the gas phase resulting in no net rate enhancements for the ethylene reduction reaction, given by equation (2.8)

$$2O^{2}_{YSZ} \rightarrow O_{2\,(g)} + 4e^- \qquad (2.8)$$

(ii) Electrochemical reduction of C_2H_4 with O^{2-} to form H_2O and CO_2 resulting in Faradaic reaction rates, given by equation (2.9)

$$6O^{-2}_{YSZ} + C_2H_4 \rightarrow 2CO_{2\,(g)} + 2H_2O + 4e^- \qquad (2.9)$$

(iii) Backspilling of $O^{\delta-}$ onto the electrode surface causes O^{2-} species hop through voids in the zirconia microstructure generated by yttria doping given by equation (2.10)

$$2O^{-2}_{YSZ} \rightarrow 2O^{-\delta} + (4-\delta)e^- \qquad (2.10)$$

While each oxygen desorption, electrochemical reaction and oxygen backspillover may occur on the catalyst surface to varying extents, the non-Faradaic increase in catalytic activity is thought to be caused by the backspilling of $O^{\delta-}$. The current theory purports that the backspilled ions act as promoters, donating electron density resulting in the lowering of catalyst work function [9]. This theory is supported by the observation of two types of adsorbed oxygen species on the catalyst surface during polarization and associated changes in catalyst work function. The presence of a strongly adsorbed, less reactive oxygen species was confirmed by in situ XPS [36], temperature programmed desorption (TPD) [37], cyclic voltammetry (CV) [37, 38] and surface enhanced Raman spectroscopy (SERS) [39–42]. The TPD plot shown in Figure 2.4 illustrates that the appearance of strongly bound $O^{\delta-}$ is not present in the absence of polarization (0 s), and within a time $\tau = 2FN_G/I$, where N_G is the moles of electrode at the gas-electrode interface, (on the order of 2500 s) achieves 63% of its final steady state value for that system indicating that one of the electrochemical steps is very slow. This is confirmed by CV in which with increasing hold times at positive potential, the appearance of two anodic peaks of differing strength are observed.

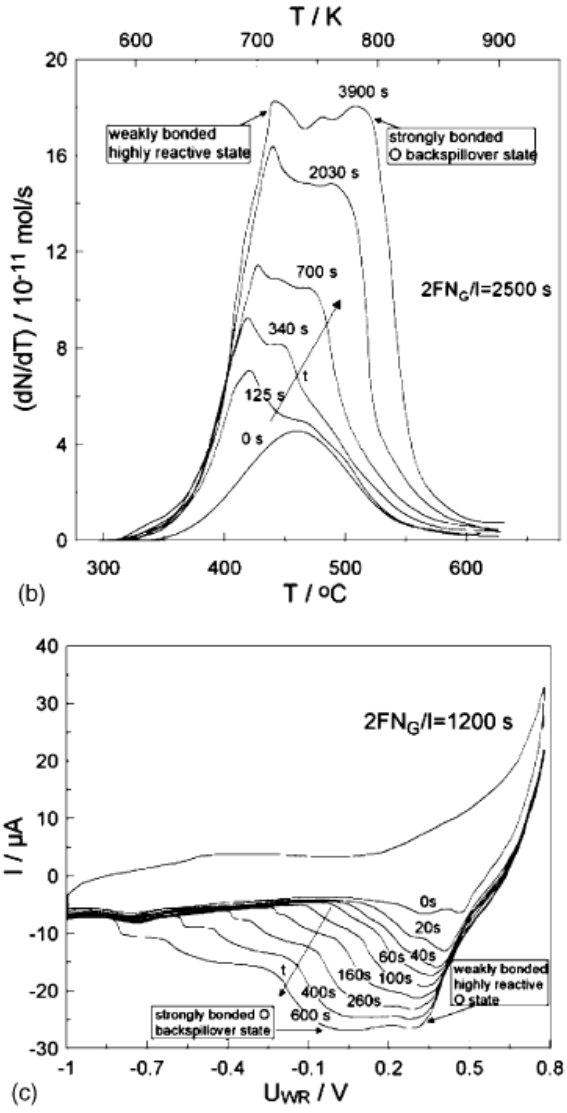

Figure 2.4 CV and TPD of the backspillover of oxygen on Pt/YSZ [43]

The promoting behavior of these strongly adsorbed backspilled oxygen was confirmed by measurement of the catalyst work function using a Kelvin Probe. [31]. Comparisons were made for different supports, NASICON (Na+ super-ionic conductor) and YSZ, and the resulting work functions were found to vary predictably with promoter coverage - decreasing for increasing Na^+ surface coverage and increasing for increasing O^{2-} surface coverage - according equation (2.11).

$$e\,\Delta V_{WR} = \Delta\, e\,\Phi \qquad (2.11)$$

Where, e = 1.602 x10^{-19} C.eV^{-1}, ΔV_{WR} represents the applied potential between the working and reference electrodes and $\Delta e\Phi$ represent the change of the work function of the catalyst surface exposed to reactive gases. An increase in the workfunction caused by the adsorption of electronegative promoters suppresses the adsorption of electrophilic species [9].

Thermodynamics

Thermodynamics of this system can be assesses to determine the driving forces of the processes – both electrochemically driven backsillover and chemically generated potentials. In addition, the derivation of equations (2.5) and (2.11) from thermodynamic basis allow for discussion of the assumptions under which these equations are valid, which may allow for the development and design of appropriate experiments.

The thermodynamic driving force of this reaction is described below for partial ion-blocking polarization as described by Janek *et al.* [44]. Ideally polarizable electrodes are electrodes at which no charge transfer occurs, or blocking electrodes, in which the interface acts as a capacitor. Further distinction is made between ion-blocking and electron-blocking electrodes. For electrochemical promotion, the use of fully polarizable electrodes leads to the development of a double layer, but since solid electrolyte maintain some electronic conductivity, fully polarizable electrodes are not possible [44].

The electrochemical potential of a system is a measure of the energy stored as chemical potential as well as the electrostatic contributions arising from the presence of an electric field. In electrochemistry, this can be expressed as the sum of inner potential or Galvani potential, χ, and the chemical potential of the bulk, μ_i. The Galvani potential includes effect of charged electrons within the bulk as well as the influence of sorbed ions on the surface, as shown in equation (2.12)

$$\bar{\mu}_i = \mu_i + \chi = \mu_i + (-zF\varphi) \tag{2.12}$$

For a symmetrical, non-polarized system, the oxygen reduction reaction (ORR) given by reaction (2.13) is in equilibrium at the three phase boundary, allowing the expression for the interface shown in equation (2.14).

$$O^{2-}(YSZ) \rightleftharpoons O_{ADS}(tpb) + 2e^- \tag{2.13}$$

$$\bar{\mu}_{O^{2-}}(ysz) = \mu_O(tpb) + 2\bar{\mu}_{e^-} \tag{2.14}$$

Across the interface, an expression for the electrical potential is given by equation (2.15)

$$F\Delta\phi = \frac{1}{2}[\mu_O(tpb) - \mu_{O^{2-}} + 2\mu_{e^-}(Me)] \tag{2.15}$$

Figure 2.5 shows the effect of polarization on the generation of electrical, chemical and electrochemical potentials across the cell.

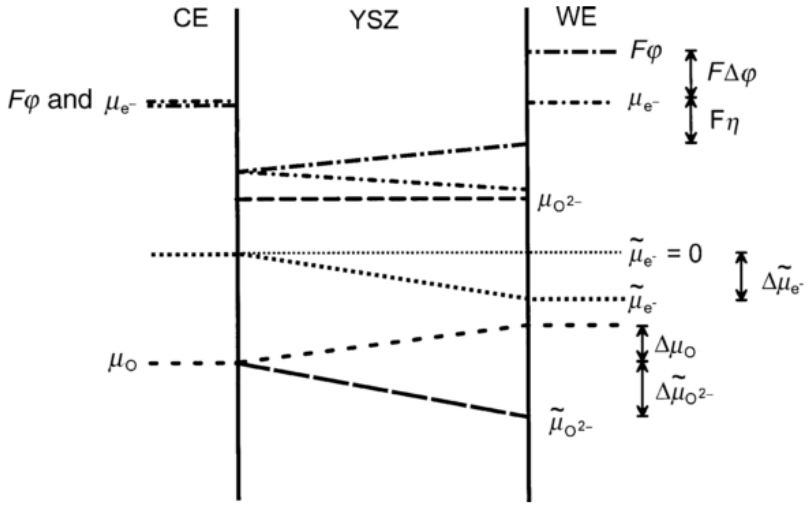

Figure 2.5 Thermodynamics of polarized partially ion-blocking electrode [44]

There is a drop in the electrochemical potential of the O^{2-} species through the electrolyte due to the presence of an electric field, but the chemical potential remains constant due to

constant concentration. A similar decrease in $\bar{\mu}_e$-is observed across the cell due to the applied potential. There is an increase in the chemical potential of adsorbed O species due to the increased concentrations caused by the backspillover of O^{2-} onto the surface of the working electrode. For concentration cells, where the concentration of O_2 at the counter electrode and working electrode are different, there would be an additional chemically driven difference.

The measurable potential between the working and reference electrode is given by equation (2.16), but can be re-expressed as the electrical potential drop through the working and reference electrodes as well as the difference across the solid electrolyte, as given by equation (2.17).

$$V_{WR} = \varphi_{Me}(WE) - \phi_{Me}(RE) \tag{2.16}$$

$$V_{WR} = \Delta\varphi(WE) - \Delta\varphi(RE) + \Delta\phi(SE) \tag{2.17}$$

Under steady state (I=0) the potential drop across the solid electrolyte is negligible ($\Delta\varphi(SE) = 0$), the open circuit potential is given by equation (2.18). Substituting equation (2.15) and assuming an overall chemical equilibrium with respect to adsorption and dissociation ($\mu_o(tpb) = \frac{1}{2}\mu_{o_2}(gas)$, equation (2.19) is obtained.

$$V_{WR}(I = 0) = \Delta\varphi(WE) - \Delta\varphi(RE) \tag{2.18}$$

$$V_{WR}(I = 0) = \frac{1}{4F}\left(\mu_{O2}(WE, gas) - \mu_{O2}(RE, gas)\right) \tag{2.19}$$

An expression for the non-equilibrium electrical potential across the cell is expressed by equation (2.20). Under non-equilibrium conditions, the potential drop across the solid electrolyte is assumed to be negligible due to high bulk conductivities. This assumption can be further

reinforced by the selection of appropriate geometric arrangement of electrodes as discussed in section 2.1.2.

$$V_{WR}(I) = \frac{1}{4F}\left(\mu_O(WE, tpb, I) - \mu_O(RE, gas)\right) \quad (2.20)$$

The overpotential, η, of the system is expressed as the deviation of the measured potential at some applied current, I from the measured potential in the absence of current, given by equation (2.21).

$$\eta = V_{WR}(I) - V_{WR}(I = 0) = \frac{1}{2F}[\mu_o(WE, tpb, I) - \mu_o(WE, tpb, I = 0)] \quad (2.21)$$

This expression of the overpotential does not distinguish between activation losses, mass transfer losses or ohmic losses. The polarization of the electrode leads to the formation of an active oxygen surface species, which follows the reaction rate expression given by equation (2.22)

$$r = r_o a_{O^*}^n \quad (2.22)$$

Where the activity of this surface oxygen, a_{O*} is given by equation (2.23)

$$a_{O^*} = \exp\left(\frac{\mu_o(tpb) - \mu_{O^*}^0}{RT}\right) \quad (2.23)$$

This is related to the chemical potential of backspillover O species at the three phase boundary and the chemical potential of adsorbed O*.

The expression of the ratio of reaction rate r and r_0 is given by equation (2.24)

$$\ln\left(\frac{r}{r_o}\right) = \frac{n[\mu_o(tpb, I) - \mu_o(tpb, I = 0)]}{RT} \quad (2.24)$$

This expression becomes equivalent to equation (2.5) when inserting equation (2.21) and assuming a=2n and $V^*_{WR} = V_{WR}(I=0)$, given by equation (2.25).

$$\ln\left(\frac{r}{r_o}\right) = \frac{2zF[V_{WR}(I) - V_{WR}(I=0)]}{RT} \quad (2.25)$$

The electrochemical potential of the electron is given as the sum of three contributions, the chemical potential, μ_{e^-}, surface potential, χ, and outer potential, ψ,. The workfunction of a catalyst, ϕ, is the expressed as the combination of the chemical potential and surface potential as shown in Figure 2.6.

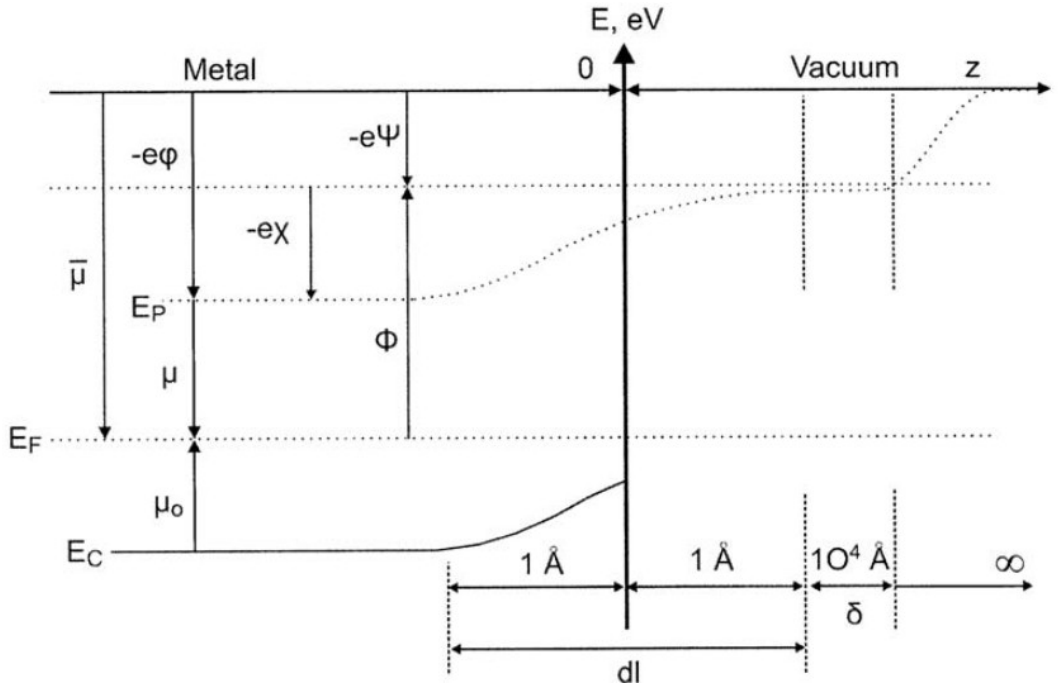

Figure 2.6 Thermodynamics of electrode surface [17]

By definition, equation (2.26) is true.

$$eV_{WR} = -(\overline{\mu}_W - \overline{\mu}_R) \quad (2.26)$$

Equation (2.26) can then be expressed as a function of the outer potential and work function according to equation (2.27) (since $\bar{\mu} = \phi - e\psi$, as shown in Figure 2.6

$$eV_{WR} = \Delta\phi_W + (e\,\phi_w - e\,\phi_R) \quad (2.27)$$

The validity of equation (2.11) then depends on the assumption that $\psi_W - \psi_R = 0$. This condition is met by backspillover such that reduction of the charge inequality present in a polarized film causes the migration of oxygen until the overall charge is equalized.

While this theoretical condition has been found to apply to a variety of solid electrolyte and electrode systems [44], several instances have been reported where data does not follow this trend [9]. It is worth mentioning also that values of ϕ are not spatially uniform over the metal surface as crystallographic planes are well known to have different work function values and thus variations over the catalyst surface are expected, with the sum being spatially uniform [45].

2.1.2 O_2, Me/YSZ System

Basics and Definitions

A solid state electrochemical cell consists of working (WE), counter (CE) and reference (RE) or pseudo-reference electrode in intimate contact with solid electrolyte. In electrochemical promotion cell, shown in Figure 2.1, cathode and anode determined by the applied potential and is governed by the oxidation or reduction processes which occur at them. For example, under applied positive polarization ($V_{WR} > 0$ V), the working electrode acts as an anode wherein the oxidation of the film occurs according to equation (2.28). Concurrent reduction reaction occurs at the counter electrode according to equation (2.29), resulting in the overall reaction given by equation (2.30)

Anode (WE) $$Me \rightleftharpoons Me^{n+} + ne^- \quad (2.28)$$

Cathode (CE) $$\frac{1}{2}O_2 + 2e^- \rightleftharpoons O^{2-} \quad (2.29)$$

Overall $$2Me + \frac{n}{2}O_2 \rightleftharpoons Me_2O_{\frac{n}{2}} \quad (2.30)$$

Since the potential of an electrode is not directly measureable, it is taken with respect to a reference electrode. In aqueous electrochmistry, electrodes such as the standard hydrogen electrode (SHE), based on the H_2/H^+ redox couple, is assigned as E = 0 V. The analogue in solid state electrochemistry is the pseudo-reference electrode based on equation (2.31)

$$\frac{1}{2}O_2 + 2e^- \rightleftharpoons O^{2-} \quad (2.31)$$

This reaction is partial pressure sensitive and depends on the microstructure and geometry of the reference electrode. Concurrent to the electrochemical oxidation and reduction of the working electrode, the oxygen evolution reaction occurs according to equation (2.29).

Backspillover of electrocatalytic reduced oxygen occurs at the interface of metal electrode, YSZ and gas phase, named three phase boundary (TPB). The system of $O_{2(g)}$,Me/YSZ system, where Me is a metal electrode, is well studied in the literature, but determination of the reaction mechanism is not straightforward. Several pathways are possible depending on temperature, oxygen partial pressure, applied polarization, electrode preparation method, microstructure and material. Common proposed mechanisms which appear in the literature appear in Figure 2.7

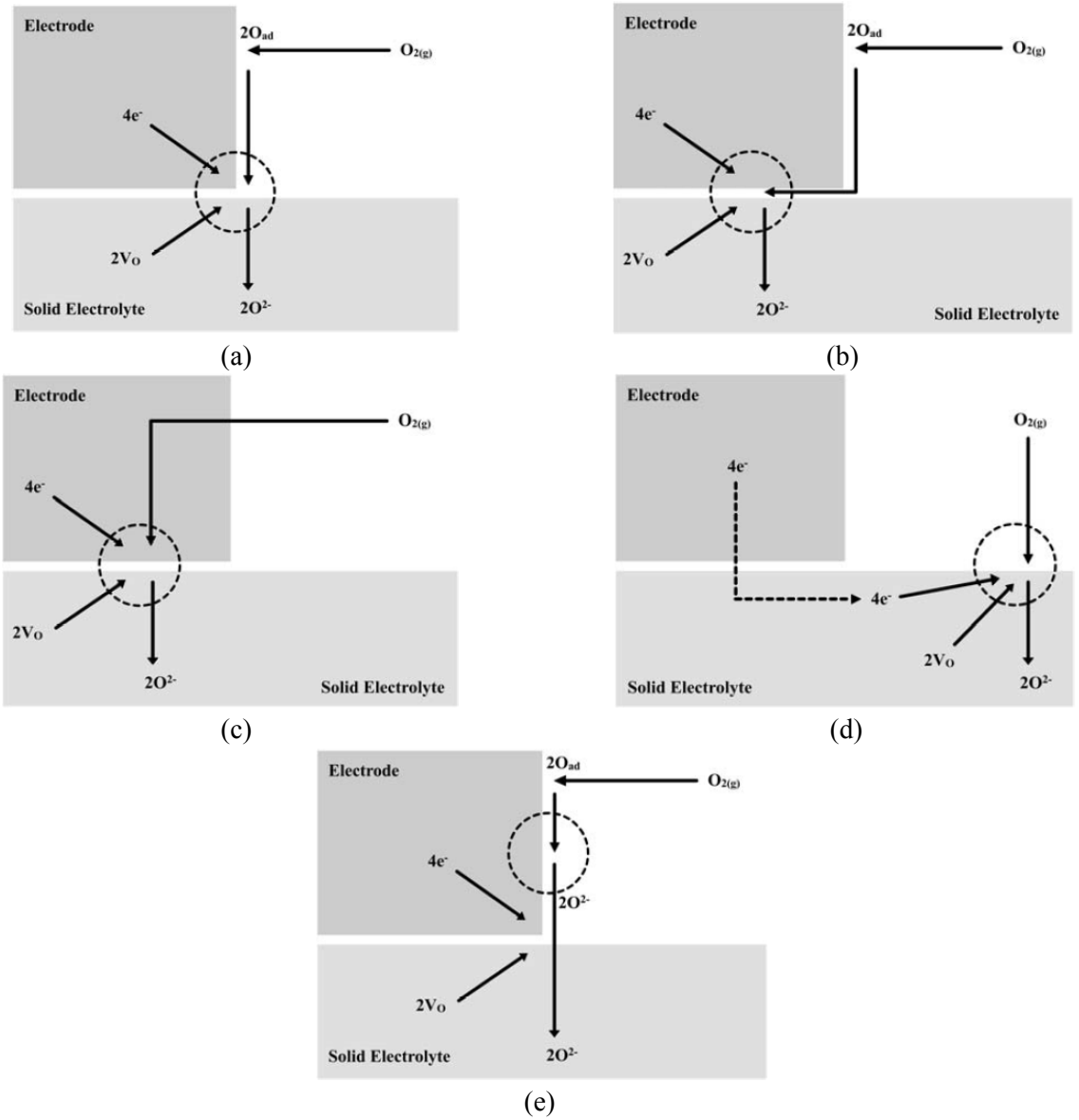

Figure 2.7 Mechanism for the oxygen exchange reaction at the O_2(g) Me/YSZ interface [46]

Many theories are present in literature as to the rate determining step of the oxygen exchange reaction (OER). It is found to be diffusion limiting at low partial pressures, high temperatures (> 800 °C), high overpotentials (|η| > 200 mV) and very thick porous electrodes [46]. The dissociative adsorption and O_{ADS} diffusion as shown by path a, b and e was found to be rate limiting steps in particular for temperatures below 500 °C [46]. Pathway c is discounted for

electrodes with low oxygen solubility, such as Au, Rh, Pt, Pd. At low overpotentials, the process is charge transfer limiting and so the rate of oxygen exchange follows the Butler-Volmer equation. In the case of electrochemical promotion, the rate of the oxygen exchange in only limiting under high overpotentials or high current densities when the rate of regeneration of oxygen voids is slower than their rate of emptying which results in a characteristic blackening of the zirconia substrate [47, 48]. These conditions are avoided by operating at potentials of -2 V to 2 V.

Electrode Configuration

A variety of cell geometries have been used in literature to study electrochemical behaviour of films interfaced with solid electrolytes [49, 50]. A three electrode system is the most commonly used, with the placement and geometry of working, counter and reference electrodes having a bearing on the electrochemical measurements of the system. Geometries should ensure a uniform current density at the working electrode [50] and to this aim a symmetrical arrangement of the counter and working electrode is preferred. The placement of the reference electrode nearest to the working electrode, such as those shown in Figure 2.8, has been shown to achieve most accurate results [49, 50].

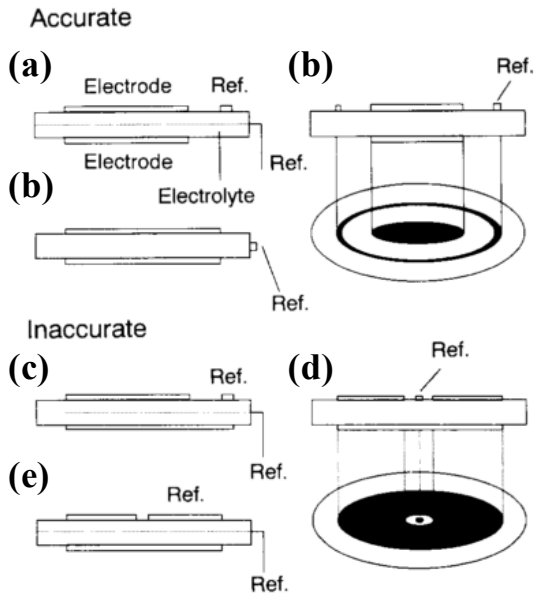

Figure 2.8 Cell geometries for measuring overpotentials in SOFC (modified from [49]**)**

Several studies use this configuration [51–54], however the most commonly used configuration place reference electrode next to the counter electrode [9, 17, 43, 55–60] and so this approach was selected for this study to allow for comparison of results.

2.2 Solid Electrolyte Cyclic Voltammetry (SECV)

2.2.1 Basics and Definitions

Cyclic voltammetry is an electrochemical technique traditionally used to study the kinetics and mechanisms of electrochemical reactions occurring at an electrode. The theory of cyclic voltammetry as developed by Sevcik [61], Randles [62], Delahay [63], Srinivasan and Gileadi [64] as well as Bard and Faulkner [65] is well established for aqueous systems, but requires careful consideration when applied to solid electrolyte cells. The adaptation of aqueous cyclic voltammetry to solid electrolyte cyclic voltammetry [51, 66, 67].

The technique involves changing applied potential between reference and working electrode, V_{WR}, at a constant rate scan rate, ν as shown in Figure 2.9. The resulting current is measured. At very slow scan rates, the curve collapses to the Butler-Volmer equation, given in equation (2.32) and shown in Figure 2.10, as the system approaches equilibrium conditions.

$$i = i_o\left\{\exp\left[\frac{\alpha_a zF\eta}{RT}\right] - \exp\left[-\frac{\alpha_c zF\eta}{RT}\right]\right\} \tag{2.32}$$

where i_o is the exchange current density, α_a and α_c are symmetry coefficients for the anodic and cathodic processes respectively, η is the total overpotential and z is the number of electrons exchanged during the reaction. With increasing scan rates, the capacitance and electron transfer phenomenon appear and can be quantified by variation in the scan rate, upper and lower potentials of the scan and hold time at the starting potential.

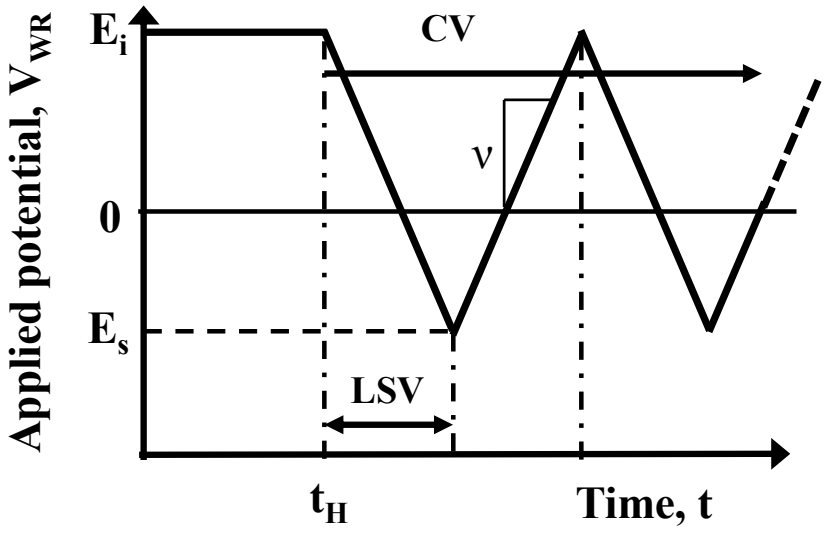

Figure 2.9 Schematic and definitions of linear sweep voltammetry (LSV) and cyclic voltammetry (CV) techniques (adapted from [68]**)**

Where E_i is the initial catalyst potential corresponding to the beginning of the cycle, E_s is the switching potential, ν is the scan rate (mV/s). Cyclic voltammetry can be used to determine the electrochemical reaction occurring at the electrode, their reversibility, the number of steps

involved and adsorption-desorption processes. Figure 2.10 shows a typical cyclic voltammogram for solid state system of Pt/YSZ.

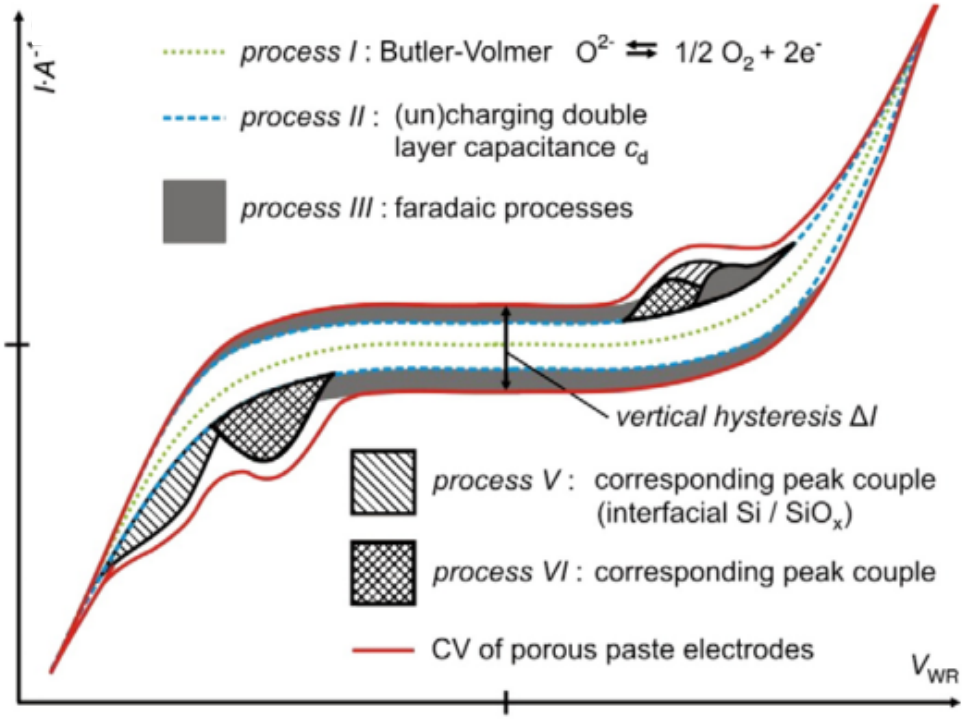

Figure 2.10 Schematic of cyclic voltammogram for Pt/YSZ system [68]

The vertical hysteresis of the scan, indicated by ΔI, gives a measure of the capacitive behavior of the scan. Current peaks generated correspond to oxidation and reduction of species on the electroactive surface of the cell. The amounts of species involved may be determined by integrating the peaks with respect to time and using Faraday's law according to equation (2.33)

$$n = \frac{\int_{t_0}^{t_1} i\,dt}{zF} = \frac{Q_j}{zF} \qquad (2.33)$$

Where Q is the charge associated with process j, z the electrons transferred (for ORR, n=2).

Further information about the mechanism can be extracted from the peak current and potential values. The reversibility and kinetics can be determined from changes in scan rate. A

reversible or Nerstian system is characterized by paired electrochemical peaks of peak current I_p according to equation (2.34).

$$I_p = 0.4463zFA\sqrt{\frac{zFD_{Ox}v}{RT}}C_{Ox,b} \quad (2.34)$$

Where the electrode surface A, cm^2, D_{ox} is the diffusivity in $cm^2.s^{-1}$, v is the scan rate in $V.s^{-1}$ and $C_{ox.b}$ the bulk concentration of active species in $mol.cm^{-3}$. The peak potential, E_p, is independent of the scan rate. The reverse peak is also characterized by I_{pc},=I_{pa} and E_{pa}-E_{pc} =2.3 (RT/zF). For irreversible systems, the peak current and potential are related by equations (2.35) and (2.36).

$$\mathrm{I_p} = 0.4958\ \mathrm{nFa}\sqrt{\frac{\alpha \mathrm{n_a} \mathrm{F} \mathrm{D_{Ox}} \nu}{\mathrm{RT}}}\mathrm{C_{ox,b}} \quad (2.35)$$

$$\mathrm{E_P} = \mathrm{E_o} - \frac{\mathrm{RT}}{\alpha \mathrm{n_a F}}\left[0.78 + \ln\left(\frac{\sqrt{\mathrm{D_{Ox}}}}{\mathrm{k}}\right) + \ln\left(\sqrt{\frac{\alpha\ \mathrm{n_a F}\ \nu}{\mathrm{RT}}}\right)\right] \quad (2.36)$$

Where E_0 is the standard potential of the redox couple, alpha the transfer coefficient, D_o the diffusion coefficient of the oxidized species, k the standard reaction rate [59].

For charge transfer limited reactions, the peak current is found to be linearly proportional to the scan rate according to equation (2.37) and (2.38)

$$I_p = \frac{zFQ_c}{4RT}\nu \quad (2.37)$$

$$E_{Pa} = E_{Pc} \quad (2.38)$$

Linear sweep voltammetry (LSV) is also used in literature to investigate the quantitative non-steady state response of an electrode to stimulus.

2.2.2 Oxidation Models

The mechanism of oxide formation is decided by the nature of the oxide (n-type, p-type), state of the surface as well as the partial pressure of oxygen and temperature. These impact the rate determining step which dictates the rate of formation of oxides. Oxidation rates for metals follow three main forms: logarithmic (inverse logarithmic), linear, and parabolic reaction rates. These are discussed below.

Parabolic

A parabolic rate of oxide formation is dictated by a mechanism in which anion or cation diffusion through a formed scale is rate limiting according to equation (2.39).

$$x = k_p t^{\frac{1}{2}} \tag{2.39}$$

where x is the oxide thickness or mass, k_p is the parabolic rate constant. Wagner proposed a model for the formation of oxidation through displacement of charged species as a rate limiting step. The model applies for compact, stoichiometric oxides where migration of ions or electrons is the rate controlling process. With the adsorption of oxygen onto the metallic surface, a dipole is generated across the M-O bond which drives the migration of positive charged species towards the gas-oxide interface (p-type oxide) or negatively charged oxygen species towards the metal surface (n-type oxide). As the oxide grows thicker, the electrical potential generated increases. This is illustrated in Figure 2.11.

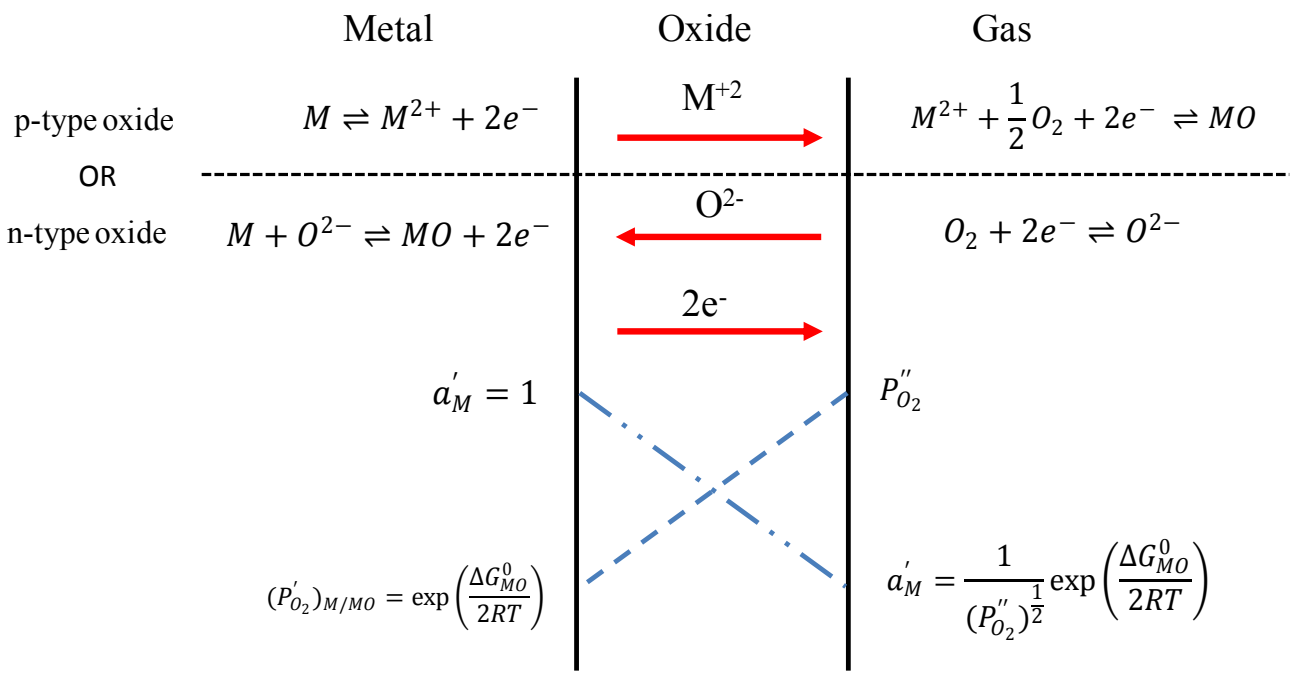

Figure 2.11 Wagner's theory of oxidation

The steady state flux of charged species, i, is expressed as a function of the chemical potential and electric field across the oxide film by equation (2.40)

$$J_i = \frac{D_i C_i}{k_B T}\left\{-\frac{d\mu_i}{dx} + z_i F \frac{d\phi}{dx}\right\} \qquad (2.40)$$

Where μ_i is the chemical potential, D_i the diffusion coefficient of the migrating species, Z_i the charge of the species, $\frac{d\phi}{dx}$ the electrical potential, k_B the Stefan-Boltzman constant and T the temperature. Assuming an overall neutral charge, the flux of anionic or cationic will be equal to the charge of electrons through the oxide and the rate of formation of an oxide can be derived to give equation (2.41)

$$\frac{dx}{dt} = \frac{3 D_i \Delta C_i}{x} V_{Ox} \qquad (2.41)$$

Where V_{OX} is the ratio of moles of metal required to form one mole of oxide (V_{OX}=1)

This equation is valid for thick oxide films (less than 1 μm), but with thinner oxide films, the Nernst-Einstein relation ($qEa<<k_BT$) used in the derivation of Wagner's theory no longer holds and, as shown in Figure 2.12, the growth rate of thin oxide films deviates from this model [69].

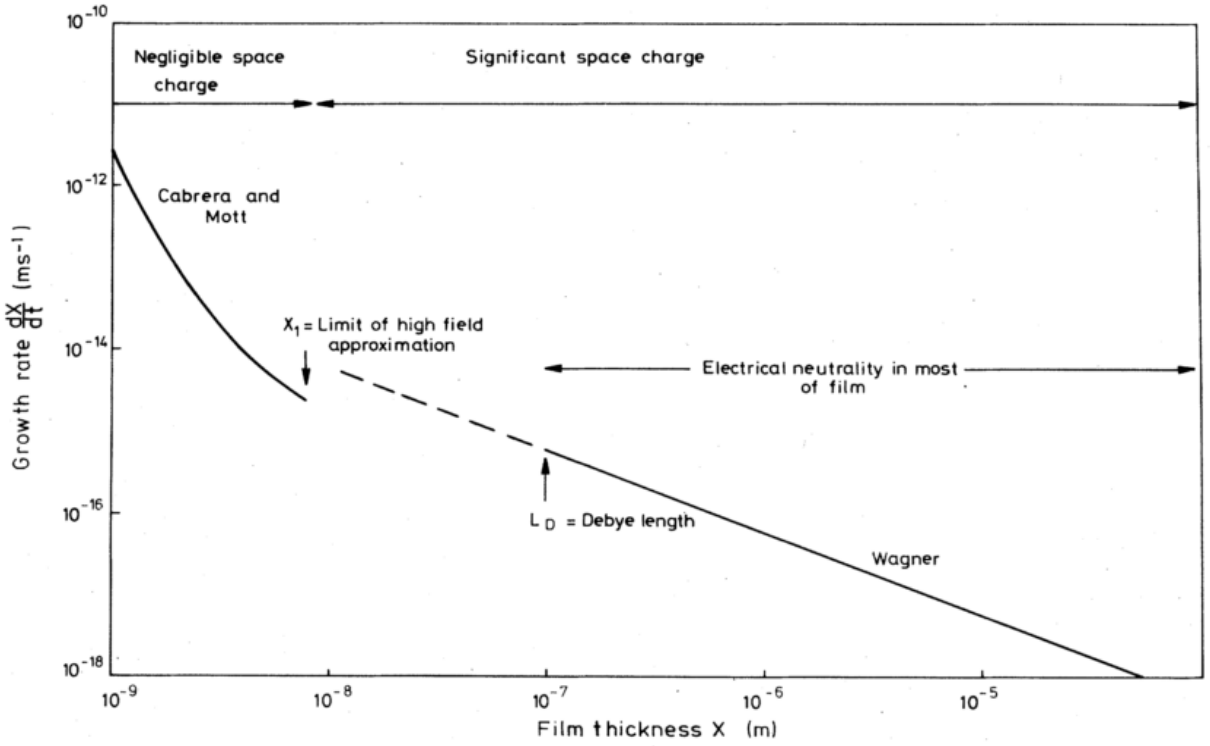

Figure 2.12 Growth rate of hypothetical p-type oxide as a function of oxide thickness [69]

As a result, for much thinner oxides, a logarithmic rate expression is required, such as that proposed by Mott and Cabrera [70, 71].

Logarithmic

The thin film oxidation model covered by Cabrera and Mott was developed based the assumption that the limiting step is the ionic jump process in the presence of the electric field and voltage across the oxide film for the reaction given by equation (2.42)[69]

$$\frac{1}{2}O_2(gas) + 2e^-(metal) \rightarrow O^{2-}(surface) \quad (2.42)$$

The driving force is the electrical potential across the oxide, ΔV, approximated by equation (2.43)

$$\Delta V = -\frac{\Delta G^0}{2e} + \frac{kT}{2e}\ln\left[\frac{4e^2 N_s a(O_2)^{\frac{1}{2}} X}{kT\ \varepsilon\ \varepsilon_0}\right] \quad (2.43)$$

Where $\boldsymbol{\varepsilon_0}$ and $\boldsymbol{\varepsilon}$ are the dielectric coefficients of vacuum and the oxide film respectively, $a(O_2)$ the oxygen activity at the oxide surface. The resulting rate expression follows an inverse logarithmic form, as shown in equation (2.44).

$$\log\left(\frac{dl}{dt}\right) = B_1 + \frac{B_2}{l} \quad (2.44)$$

Where B_1 and B_2 are fitting constants and l is the film thickness.

Alternative logarithmic rate expressions are given by equations (2.45) and (2.46).

$$x = k_{LOG}\log(t + t_0) + A \quad (2.45)$$

$$\frac{1}{x} = B - k_{IL}\log(t) \quad (2.46)$$

Where x is the mass or film thickness of oxide, k_{LOG} and k_{IL} are logarithmic and inverse logarithmic rate constants, respectively, and a and b are constants. Due to the presence of constants in the equation, distinguishing between rate expressions is unrealistic since both rate expressions can be adjusted to fit the data.

Linear

Linear oxidation rates are observed in metal surface where the charge transfer is the limiting step. This occurs in the case of initial oxide formation on a clean metal surface or in the

case of the formation of a porous scale. The expression of the film thickness is expressed as equation (2.47)

$$x = k_L t \tag{2.47}$$

Linear kinetics are often observed when the oxide film cracks or spalls allowing access to the metal beneath resulting in less diffusion limited mechanism [72].

2.2.3 State of the Art

Cyclic voltammetry has been used to study metal/YSZ interfaces between temperatures of 300-600°C for platinum [9, 17, 43, 55–60, 66, 73], nickel [38] and palladium [74] systems. Variability found in cyclic voltammograms in solid state electrochemical cells is attributed to the inconsistency of film preparation and pre-treatment methods, which result in variations of microstructure, purity and geometry of the polarisable surface [60].

Pt/YSZ System

The O_2/Pt/YSZ is the most commonly studied as platinum is considered the model materials for solid state cells. Early work by Vayenas *et al.* on platinum paste electrodes identified an anodic and cathodic peak describing to the formation and reduction of backspillover species [56]. These peaks were insensitive to changes in partial pressure, but found to form according to an irreversible charge transfer limited process according to equation (2.37).

A second cathodic peak was later reported [57, 66, 67], and hypothesized to be caused by the backspillover of oxygen [57], platinum oxide or the rearrangement of platinum oxide [66]. Jaccoud *et al.* also identified these two cathodic peaks as well as a third and fourth peak which appeared with increased hold time [59], as shown in Figure 2.13.

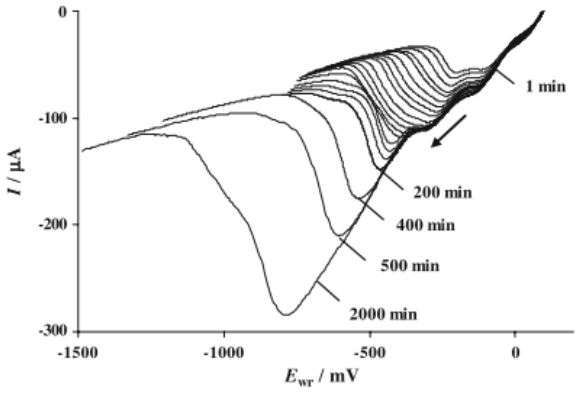

Figure 2.13 Linear sweep voltammetry measurements. Effect of holding time t_H at E_i=100 mV on the first cathodic scan, T = 450 °C, P_{O2} = 20 kPa, v = 10 mV.s^{-1}[75]

The additional peaks were attributed to the formation of oxides on different locations on the electrode [60]. Oxides may form at the Pt/YSZ interface, Pt/O_2 interface, or at the three phase boundary (YSZ/O_2/Pt) [76]. The model put forward by Jaccoud *et al*. comprise first of the monolayer formation of PtOx species along the Pt/YSZ interface, then the backspillover of O^{2-} along the surface of the electrode through the three phase boundary. The third and fourth peaks the describe the extension of the three phase boundary or the growth of the oxide at the Pt/YSZ interface [59].

Further investigation into the formation of PtOx oxide at the interface was confirmed by the use of chronoamperometry. Kenjo *et al.* [51] and Jaccoud *et al.* [76] identified a pseudocapacitive behaviour of the film which could not be attributed of a species stored as a chemical oxide on the film. This effect was caused by the formation of PtO_x at the electrode electrolyte interface [76]. The growth of PtO_x at the Pt/YSZ interface was found to be slow, follow $t^{1/2}$ kinetics and show to saturation [75].

Effect of Microstructure

The effect of microstructure on the current Pt/YSZ model is of interest as the phenomenon of backspillover is limited by the three phase boundary length. The three phase boundary may be determined through measurement using scanning electron micrographs of the film surface. This leads to an underestimation of the three phase boundary length as it excludes nanoscopic three phase boundary contributions identified by Ryll *et al.* [77] in sputter deposited Pt.

Vayenas *et al.* derived a correlation between the change in peak current with respect to scan rate from which the activity of oxygen at the three phase boundary, N_{Otpb}, could be determined. Equation (2.48) is valid for charge transfer limiting reactions, where the relation between peak density, I_p, and scan rate, ν, is linear.

$$I_p = \frac{\alpha_c z F^2 N_{o,tpb}}{2.72\ RT}\nu \tag{2.48}$$

where z is the total number of electrons exchanged during electrochemical reaction per mole of reactant, N_{Otpb} is the moles of active oxygen sites at the three phase boundary, R is the gas constant and T the temperature of the gas. From this, the length of the three phase boundary, l_{tpb}, could then be determined using equation (2.49).

$$l_{tpb} = \frac{N_{O,tpd}\, N_{AV}(2r_{Pt})^2}{\left(\frac{D_o RT}{F\nu_p}\right)^{0.5}} \tag{2.49}$$

where D_0 is the surface diffusivity of oxygen on platinum, r_{Pt} the radius of a platinum atom and ν_p is the pre-factor for the diffusivity coefficient (ca. 10^{-12} s) and N_{AV} is Avogadro's constant, 6.02×10^{-23} atoms.mol^{-1}.

The behaviour on platinum electrodes was quantified by Jaccoud *et al.* [60] with comparison to cermets with high three phase boundary and dense sputtered (200 nm) platinum films. The presence of cathodic peaks was found prevalent in dense films and was characterized

as a Pt/YSZ interface phenomenon because under the same condition were not observed in cermet electrodes. [60] Similar behaviour was observed by Mutoro *et al.*, who compared a variety of paste films with varying degrees of solvent resulting in varying thicknesses.

The effect of changes in three phase boundary was also investigated in dense plasma layer deposited (PLD) films. Successive scratching of the film resulted in marginally longer three phase boundary, resulting in a lower charge of the cathodic peak, as shown in Figure 2.14. The reduction of oxygen is more significant in samples with greater three phase boundary than the storage of PtOx at the PtOx interface.

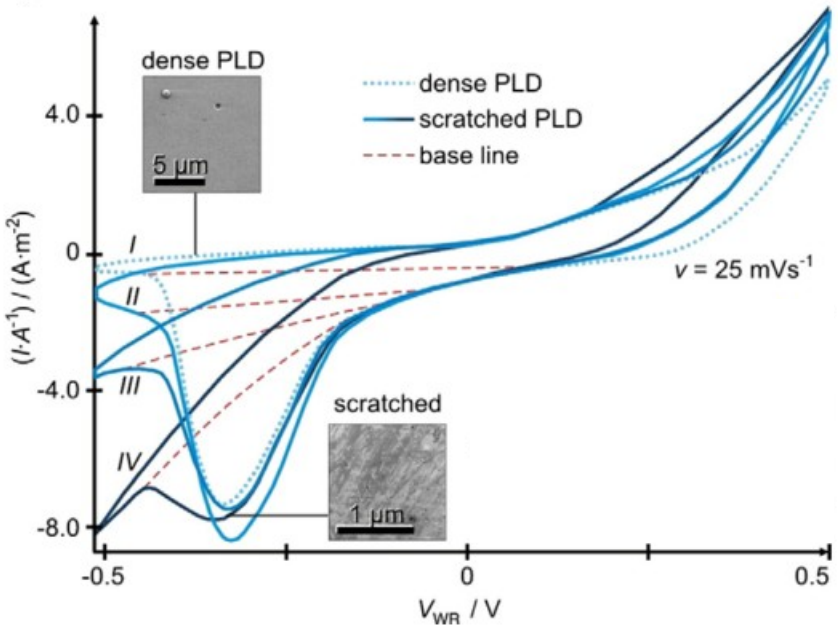

Figure 2.14 Cyclic voltammograms of dense Pt PLD films on YSZ where film sequentially (I, II, III, IV) scratched to increase three phase boundary [54]

Oxygen uptake becomes more significant and the peak charge associated with the reduction of interface PtOx species becomes smaller.

Effect of Impurities

The traditional interpretation of peaks within for platinum paste electrodes has been put under scrutiny with the identification impurities in the metal pastes as well as precipitated on the surface of the electrolyte [68]. Calcium, sodium, potassium and silicon was found on the surface of annealed single crystal YSZ samples, while sintering aids such as silica are commonly added to electrode pastes. In the presence of such contaminants, the electrochemical formation of oxides, specifically silicon oxide was determined to occur preferentially over the formation of platinum oxides [78]. Samples dosed with silica show two anodic and two cathodic peaks not observed in untreated paste electrode.

Effect of Partial Pressure

Cyclic voltammetry on platinum electrodes is has been carried out in air (P_{O2} = 20 kPa) [46, 56, 57, 59, 60, 76, 79–81], pure oxygen [51, 53, 66, 67, 80, 82] or at reduced oxygen ($P_{O2,min}$=10^{-7} Pa) [43, 51, 55–57, 67, 82–84] or no oxygen [66, 67, 82].

Studies of the impact of partial pressure on platinum electrodes has not shown significant changes in the peaks of the cyclic voltammogram. Vayenas *et al*. found the charge ratio of anodic and cathodic peaks (Q_A:Q_C) to be less than 1. The discrepancy was purportedly caused by the formation of chemical oxides at the three phase boundary of the electrochemically reduced film, but verification of the impact of partial pressure on this ratio were not performed [56]. Additional studies of the variation of partial pressure on the shape of the cyclic voltammograms showed no change in peaks [59] or shift of the main cathodic peak to more negative potentials [66, 82]. Work by Jaccoud *et al.* found greater currents resulted in the oxygen reduction region of the scan with higher partial pressures, as shown in Figure 2.15

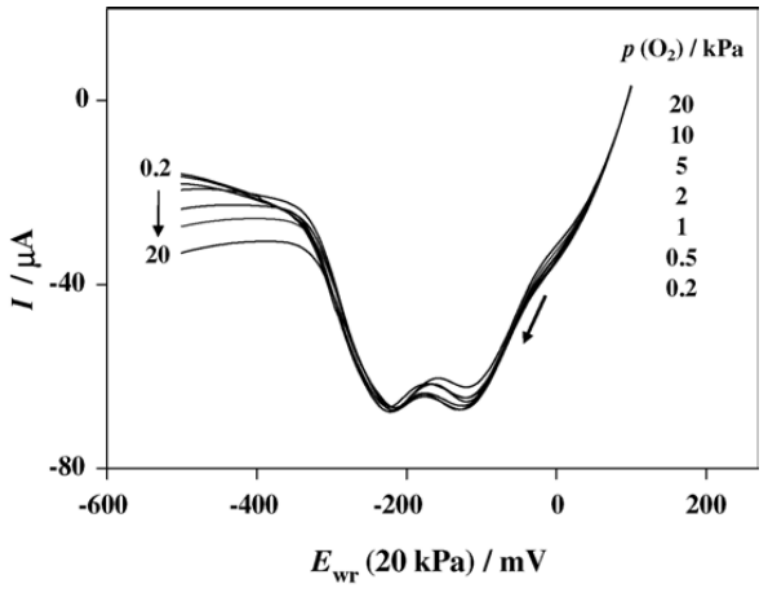

Figure 2.15 Linear sweep voltammetry of platinum paste electrodes at different partial pressures of oxygen [59]

Effect of Temperature

Peak currents were found to increase with temperature until a critical temperature above which oxides are no longer stable. For platinum this temperature was found to be 444 °C [56].

Model

The model presented in Figure 2.16 was developed for sputtered platinum electrodes. With anodic polarization, PtO forms in a monolayer along the interface of YSZ and platinum and, with increased polarization time, extends from the surface forming a surface oxide species. Further polarization leads to the growth of the interface oxide layer according to a parabolic growth rate consistent with Wagner's theory, which proposes the rate determining diffusion of Pt^{2+} oxides through the scale. At higher overpotentials, Jaccoud proposes a Mott and Cabrera mechanism of oxygen diffusion across PtO or Wilkinson mechanmism involving the exchange of strongly adsorbed oxygen [85].

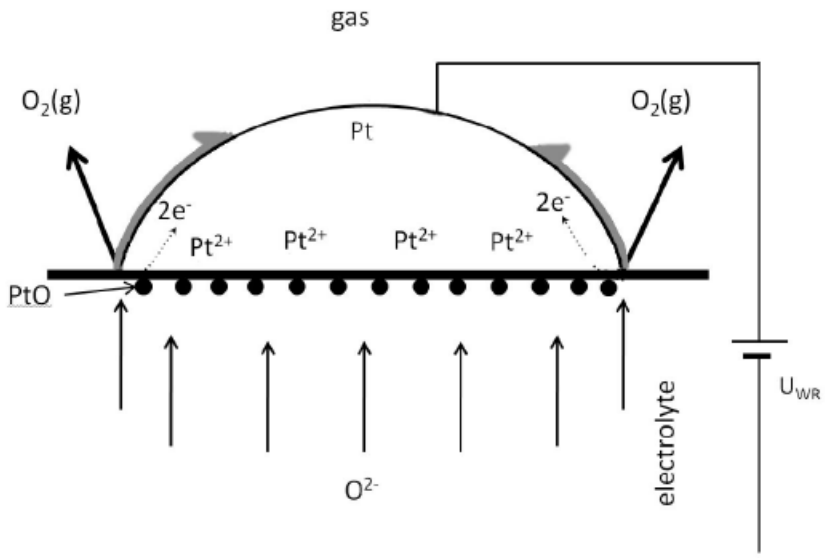

Figure 2.16 Model for anodic polarization of sputtered platinum electrodes on yttria stabilized zirconia [85]

For dense electrodes, with decreased three phase boundary the evolution and backspillover of oxygen are suppressed resulting in a greater polarization, pseudocapacitance and higher current efficiency for the formation of platinum oxides at the interface.

Ni/YSZ system

Nickel is a model oxidation compound as it follows Wagner oxidation theory to form near stoichiometric oxides [38, 86]. Souentie presented a model for oxidation of 880 nm nickel film on YSZ under anodic polarization [38] Similarly to cyclic voltammetry of platinum electrodes, a single cathodic peak was observed which increased with anodic holding time with a rate expression of $t_H^{0.5}$, as shown in Figure 2.17.

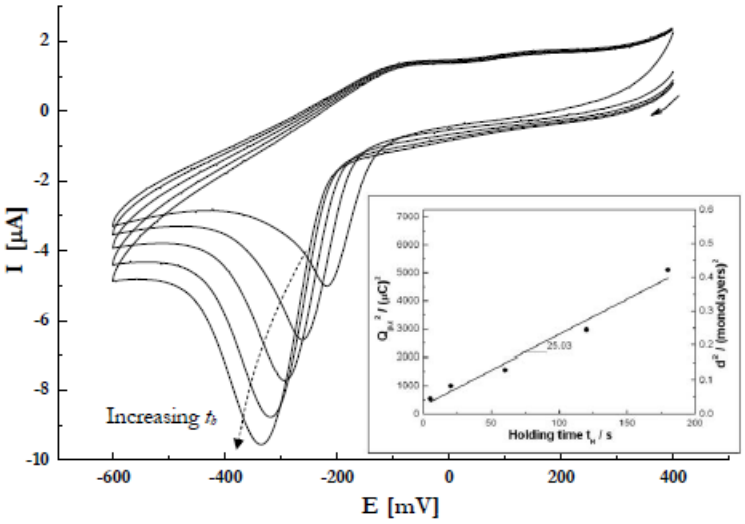

Figure 2.17 Effect of hold time on 880 nm nickel thin film. Inset: charge change with increased hold time [85]

The peak was found to disapeare below polarization potentials of 125 mV indicating the electrochemically rather than chemically formed oxide results from polarization process. A model was proposed wherein the oxides form along the interface through migration of Ni^{2+} through the formed scale and extend through the three phase boundary onto the surface of the film as shown Figure 2.18

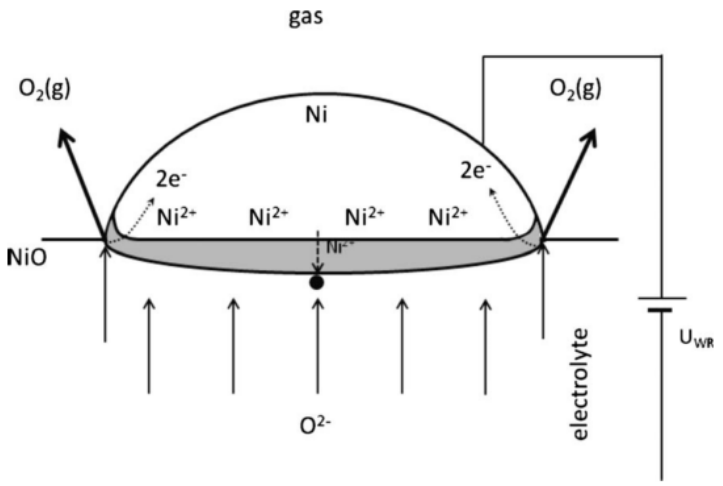

Figure 2.18 Nickel model for anodic polarization of 880 nm nickel film interfaced with YSZ [38]

Concurent to the oxide growth, oxygen evolution occurs under positive polarization and current efficiency for this process increases as more oxides form at the three phase boundary.

2.2.4 Reproducibility

The impact of impurities and microstructure on cyclic voltammetry results muddled experimental results from early studies which favored metal paste electrodes [54, 68]. The use of physical vapor deposited thin films for which high purity electrodes with reproducible and well defined microstructure have lead to less adulterated studies of the electrochemical promotion mechanism. Despite this, few studies show the reproducibility of the results.

This uncertainty stems from the electrode configurations and reference electrode materials. As discussed in section 2.3, the location of the electrodes is inconsistent from study to study allowing for poor qualitative comparisons for measured values. In addition, while the use of PVD films is being adopted for working electrodes, counter and reference electrodes continue to be produced from Pt or Au pastes. While the counter electrode merely provides an electron sink or source for the electrochemical cell, and thus has little bearing on electrochemical measurements, the reference electrode has a greater impact on the reproducibility of results. The potential of the reference electrode is sensitive to partial pressure of oxygen in the gas stream and the microstructure of the electrode. Unlike aqueous electrochemistry, where the same reference electrode can be transferred and used for a series of electrochemical experiments, the reference electrodes used in solid state electrochemistry must be freshly applied to each cell studied. As a consequence, the results presented for each film studied in this work purport to a single sample and must be compared to experiments of similar materials or thicknesses with great care.

2.3 **Electrode Morphology**

Electrode morphology plays an important role in determining the electrochemical processes which occur in a solid state cell. The minimum requirement for thin film metal electrodes is electronic conductivity of the electrode and percolation over the desired contact area. In developing an electrode model, studies rely on highly defined electrode systems. The electrode system is comprised of three two phase boundaries (*Me*/O_2, *Me*/YSZ, YSZ/O_2) and one three phase boundary (*Me*/YSZ/O_2).

The length of the three phase boundary has been shown to be most important as the backspilling of oxygen is considered the rate limiting step [9]. As modeled by Vayenas *et al.* [9, 87] and confirmed experimentally by Baranova *et al.* [88] and Koutsodontis *et al.* [89] the rate enhancement ratio decreases with increased film thickness as a result of a reduced three phase boundary. This results in a lower concentration of backspilled O^{2-} near the catalysts surface as it reacts with reducing agents in the gas stream [89]. Studies of the Pt/YSZ and Ni/YSZ system have shown the storage of oxides at the electrode/electrolyte interface occurs in dense films with high two phase boundary and low three phase boundary. This phenomenon is associated with a pseudocapacitance and permanent or persistent electrochemical promotion (P-EPOC, Pers-EPOC).

As shown in Figure 2.19, additional concerns need be to addressed in order assure reproducibility of results, such as structure and orientation of the materials, grain boundaries, defect chemistry, possible interdiffusion at phase boundaries, morphologies of the surface and the interface, pores, impurities and their segregation. The impacts of impurities can be mitigated by the selection of materials and synthesis method. Impurities and other system components, such as yttria, can segregate and accumulate at phase boundaries result in time dependant

activation or passivation of the electrode [54]. Defect chemistry of materials influence conductivities. The morphology of interfaces between electrode and electrolyte controls the interface capacitance [54]. In addition, surface roughness of substrates bear an impact on the evolution of thin film morphologies as discussed in section Section 2.4.4. The orientation of materials or distribution of grain boundaries as well as the appearance of new interface phases or interdiffusion are also significant. Traditionally, this is accounted for by use of single crystal electrolytes or high purity

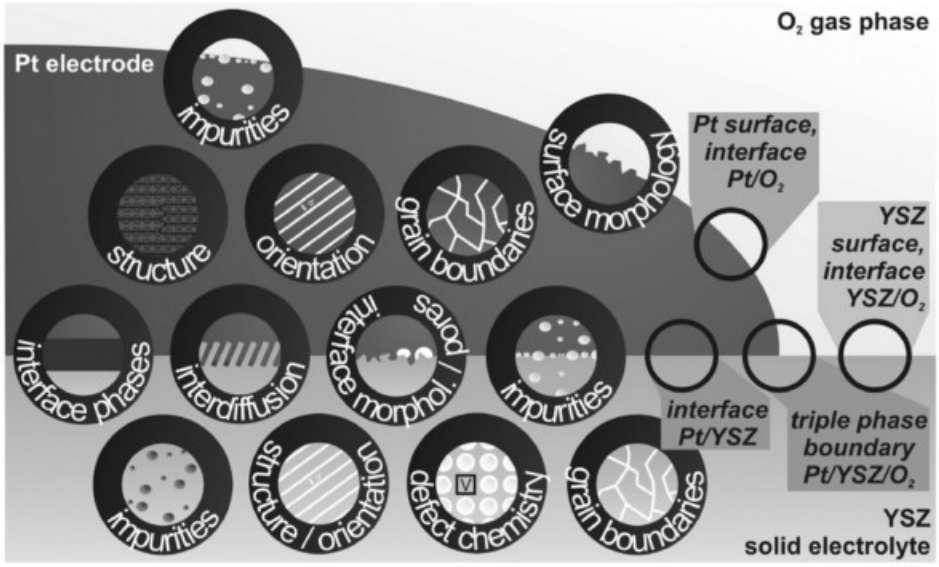

Figure 2.19 Interfaces and factors controlling electrochemical behavior [54]

Thin film catalysts have low dispersions and make for poor catalysts when compared to alternative, such as nanoparticles, but have an simple, open which lends them to the application of electrochemical promotion. In addition to these qualities, the reproducible nature of the morphology of vapor deposited films makes the technology scalable.

2.4 Thin Film Microstructure

The formation of thin films with controlled microstructure can be achieved through a variety of deposition methods. Chemical, physical and electrochemical methods of metal film deposition have been used in the literature to make electrodes.

2.4.1 Deposition Methods

Early studies of metal films interfaced with YSZ employed metal pastes comprised of suspended metallic articles in an organic phase, which with sintering forms a thick (ca. 1-2 μm) porous films [9]. The presence of sintering agents and impurities in the film result in misleading results and the limited control over thickness and porosity that these pastes entail make it an unpopular option for mechanistic studies. Additional studies have shown that films prepared by the decomposition of salt precursors can be used for electrochemical promotion [24, 90]. While these approaches are less expensive and require little specialized equipment, they result in less morphological control and greater contamination of the electrode.

Electrodeposition methods are also used for the synthesis of highly porous films with dendritic microstructure [91]. This method is impractical due to the necessity of an electronically conductive substrate and the incorporations of impurities within the film.

Chemical and physical vapor deposition techniques are preferred as they afford greater control over morphology and thickness of thin films.

Chemical vapor deposition (CVD) is a process involving the chemical reaction of a volatile compound of a given material which reacts on the substrate with a mixture of gases to form a non-volatile film [92]. This method can be used to deposit a wide variety of film materials: metals, semiconductors, inorganic and organic in crystalline of vitreous form with desired

properties. Variants include atmospheric pressure (APCVD), low pressure (LPCVD), plasma-enhanced (PECVD) and laser-enhanced (LECVD) CVD [92]. These can be used in batch and semicontinuous operations, but concerns over the requirement of hazardous gases and mass transfer limitations limit its application.

Physical vapor deposition (PVD) techniques involve the production of metal vapors directly deposited on a substrate in a low vacuum environment resulting in thin films with few impurities and a controllable microstructure [92, 93]. Several techniques have been developed which are characterized as physical vapor deposition, cathodic arc deposition, electron beam physical vapor deposition, thermal evaporative deposition, pulsed laser deposition and sputter deposition.

In the literature, sputtering is the preferred metal for electrochemical promotion due to the ease of deposition of high melting point noble-metal catalysts, such as Pt and Rh [88, 94–97]. Sputtered films are produced by bombarding a high purity metal target with high velocity argon ions, chipping off single atoms from the target which are then directly deposited on the substrate. Due to their high velocity and low pressure in the chamber, few interactions occur between particles resulting in dense films with good step coverage and uniformity [92]. This technique also has the added advantage of allowing in situ substrate cleaning or etching with the argon plasma prior to deposition. The morphology of the film is controlled via modification of the energy of impinging atoms, but may result in surface damage and imbedding of impinging metal atoms within the bulk of the support [98]. This technique has also been used for the synthesis of non-percolated noble metal islands for use in indirect polarization for EPOC studies [23, 99].

Evaporative physical vapor deposition is not used in literature for EPOC studies due to the prohibitive melting points of the noble metal catalysts under investigation. This technique

involves the vaporization of metal samples at ultrahigh vacuum which travel linearly to the substrate and deposit on the substrate. Techniques may be further quantified by the evaporation source used. Resistance-heated, sublimation, induction-heated, electron-beam evaporation (thermionic or plasma electron beam), laser beam, arc evaporation sources are all available methods for evaporating the target material [100]. Physical vapor deposition via thermal evaporation can be used to produce thin films with a variety of microstructures characterized by grain size, crystallographic orientations, lattice defects, phase composition and surface morphology through control of deposition parameters [101].

2.4.2 Basics and Definitions

The morphology of thin films is greatly impacted by the early stages of deposition, for which deposition parameters play an important role. Conditions of the environment, thermodynamics of the film-support interactions as well as the kinetics of the process impact the resulting film structure.

Upon heating, the flux of evaporated metal atoms, shown in equation (2.50) is a function of the hydrostatic pressure in the chamber, $P_{H,}$ but strongly a function of temperature on account of its influence on the equilibrium vapor pressure, P_E [92].

$$\Phi_E = \frac{\alpha_E N_A (P_E - P_H)}{(2\pi MRT)^{\frac{1}{2}}} \tag{2.50}$$

Where α_E is the coefficient of evaporation, which is defined as the ratio of experimental evaporation rate to theoretical maximum evaporation rate and thus given a value between 0 and 1, Φ_E is the number of atoms per unit area, M is the molar mass, R is the gas constant and N_A Avogadro's constant, 6.02×10^{23}. The maximum evaporation is achieved when $\alpha_E = 1$ and P_H is zero.

The mean-free path of atoms is derived from kinetic gas laws and calculated from equation (2.51). This distance must exceed the distance from evaporation source to substrate to ensure no interactions between metal atoms during deposition.

$$\lambda = \frac{k_B T}{\sqrt{2}\,\pi\, d^2 P_H} \tag{2.51}$$

Where k_B is the Boltman constant, d the diameter of the gas particle and p the pressure in the chamber.

Evaporation in low vacuum is modeled by a point source with the metal atoms traveling towards the substrate in straight lines introducing a geometry-dependent non-uniformity across the deposition as illustrated in Figure 2.20.

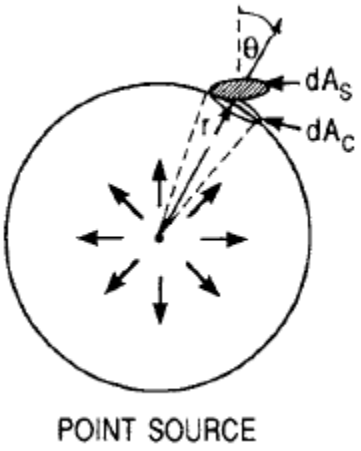

Figure 2.20 Point source evaporation [92]

For this reason, the substrate must be placed along the circumference of the sphere of which the source is the center to achieve uniform deposition.

The total mass deposited, $\overline{M_S}$, on a surface A_S is given by equation (2.52).

$$\frac{d\overline{M_S}}{dA_S} = \frac{\cos\theta}{4\,\pi\, r^2} \int_0^t \int_{A_E} \Gamma_E dA_C dt \tag{2.52}$$

Where A_C is the projected area on the sphere and θ the angle of the surface with respect to the adatom path, as shown in Figure 2.20 and Γ_E is the rate of evaporation.

Having reached the surface of the support, the energetic atom may bounce off, impinge directly into previous deposits or become physisorbed as adatoms on the surface, traveling until it reaches thermal equilibrium with the support or combines with previously deposited adatoms as shown in Figure 2.21.

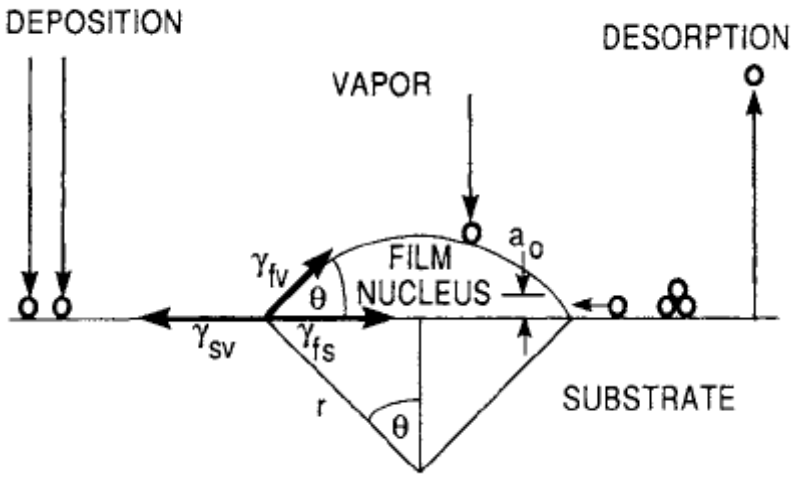

Figure 2.21 Substrate -deposit interactions [92]

The modes of film growth are determined by the metal-support interactions and are classified as:

(i) Volmer-Weber (VW) – adatom-adatom interactions are greater than adatom-substrate interactions resulting in island formation

(ii) Frank-van-der Merwe (FM) – adatom-adatom interactions are weaker than adatom-substrate interfactions resulting in layer by layer growth

(iii) Stranski-Krastanov (SK) – adatom-adatom interactions are similar to adatom-substrate interactions resulting in a layer-plus island growth.

Given the dissimilar nature of dielectric substrate and metal catalysts in electrochemical promotion systems, Volmer-Weber modes of thin film growth are expected, but instances of Stranki-Krastanov have been observed [102].

The process of film growth proceeds through stages of nucleation, island growth, impingement and coalescence of islands, formation of polycrystalline islands and channels, and finally the development and growth of a continuous film which are dependent on the kinetics and thermodynamics of the deposition system [101]. These, in turn, depend on the nature, roughness and temperature of the substrate, the rate of impinging atoms, nature of the deposit and angle of deposition [103].

At equilibrium, which is to say that the rate of deposition and desorption from the surface is equal, the minimization of interfacial energies between support-metal, metal-vapor and vapor-support results in the formation of nucleus of critical radius.

The critical radius r^* is derived from the minimization of Gibbs free energy, ΔG, and is expressed as (2.53).

$$r^* = -\frac{2\left(a_1 \gamma_{fv} + a_2 \gamma_{fs} - a_2 \gamma_{sv}\right)}{3a_3 \Delta G_v} \tag{2.53}$$

where ΔG_v change in Gibbs free energy of formation per unit volume of condensed material, γ_{sv}, γ_{fv} and γ_{fs} are the interface energies for substrate-vapor, film-vapor and film-substrate interfaces and $a_1 r^2$ is the curved area of the film-vapor interface, $a_2 r^2$ the projected area of the film-substrate interface and $a_3 r^3$ is the volume of the nuclei involved.

Where the gibbs free energy evaluated at r^* is given by equation (2.54).

$$\Delta G^* = \frac{4\left(a_1 \gamma_{fv} + a_2 \gamma_{fs} - a_2 \gamma_{sv}\right)^3}{27 a_3^2 (\Delta G_v)^2} \tag{2.54}$$

From this the density of stable nuclei, N^*, can be determined with equation (2.55)

$$N^* = n_s \exp\left(-\frac{\Delta G^*}{k_B T}\right) \tag{2.55}$$

where n_s is the total nucleation site density.

This model, referred to as the capillarity theory, affords a simplistic model which allows for quantitative description of thin film behavior deposited near equilibrium conditions.

There is an industrial precedence for room temperature deposition, thin films are often deposited at temperatures less than 0.2-0.3 times the melting point temperature, T_m, and thus, being deposited far from equilibrium, rely heavily on the kinetics of adatom displacement [101].

The size and shape of islands form from the competition of terrace-, interlayer-exchange and edge diffusion processes. Each of these displacements has a characteristic energy barrier and tuning the relative importance of these diffusion processes can result in the formation of different microstructures [104]. The microstructure of the film is greatly influenced by surface and bulk diffusion phenomena [101].

Below, the methods used in literature for characterizing thin film microstructures are outlined. Following this, the effects of film material, substrate temperature, deposition rate and substrate roughness on the microstructure of the film are discussed.

2.4.3 Characterization of Microstructure

Microscopy

Microstructure is most frequently characterized using a variety of ex-situ microscopy techniques including scanning electron microscopy (SEM) [68, 84, 105–109], tunneling electron microscopy (TEM) [101, 108, 110–112], atomic force microscopy (AFM) [109, 113] and scanning tunneling microscopy (STM) [114].

A qualitative description of the growth of non-continuous thin films is described by the degree of agglomeration, where a highly agglomerated film is described by a low number of large islands and low agglomeration by an abundance of smaller islands [103]. Deposits may also be characterized by the critical thickness, and surface coverage. The critical thickness, t_c, is the thickness at which the film forms a percolated network, which is characterized by a drop in resistance consistent with the transition from insulating to metal state [115, 116].

Conductivity

The formation of metal films on dielectric substrate begins with the formation of isolated islands, followed by the development of percolated networks until a dense compact layer is formed. These three stages are accompanied with three different conduction mechanisms, namely, tunneling conduction, percolation conduction and continuous film conduction, respectively [117]. The transition from tunneling conduction to percolation conduction is associated with a sharp decrease in resistance from which the percolation threshold of a film can be determined. The mechanisms of conduction over these stages of growth have been modeled with aims at understanding the effect of morphology on the resistance in films.

The conductivity mechanisms in films just above the percolation threshold have been described by percolation theory models [118]. These models describe the physical properties by the surface coverage, p. The percolation threshold, p_c, is the coverage of the substrate at which the first spanning cluster appears.

For fractal systems, the resistance of a growing metal film near percolation threshold where $p>p_c$ is expected to follow a power law of the form of equation (2.56).

$$R \sim (p - p_c)^{-\mu} \tag{2.56}$$

Where μ is a coefficient dependent on the dimensionality of the system. Measurement of the resistance has been used in literature to determine critical thickness [110, 114, 118] as well as the effect of film thickness dependence of thermal stability [109].

2.4.4 Effect of Deposition Parameters

Effect of Film Material

The rate of nucleation impacts the distribution and size of islands in non-percolated film as well as the final microstructure and grain distribution in the continuous film. This behavior is decided by adatom binding energy, crystal structure of the substrate material, lattice defects, surface steps and contamination [101]. This implies that, for every set of deposit and substrate, there will be a different percolation threshold, critical radius and island density. Differences in material behaviors can be observed by differences in contact angle, which is directly related to surface tension and thus equilibrium state as illustrated in Figure 2.22. Humenik and Kingery found that the wettability of oxides by liquid metals is an increasing function of the heat of formation of the oxide of the wetting metal [119]. For the case of copper, nickel and silver heats of formation are given in Table 2.1, which are consistent with wetting angles, θ, presented in Figure 2.22.

Table 2.1 Standard heat of vaporization of nickel, silver and copper and the heat of formation of their oxides [120]

	Oxide	ΔH_f^0 (298 K) kJ.mol^{-1}
Ag	Ag_2O	-31.1
	AgO	-24.3
Cu	CuO	-157.3
	Cu_2O	-168.6
Ni	Ni_2O_3	-489.5

Silver has the highest wetting angle as well as the lowest melting temperature and is therefore expected to have the largest critical radius and therefore the highest percolation threshold of the metals.

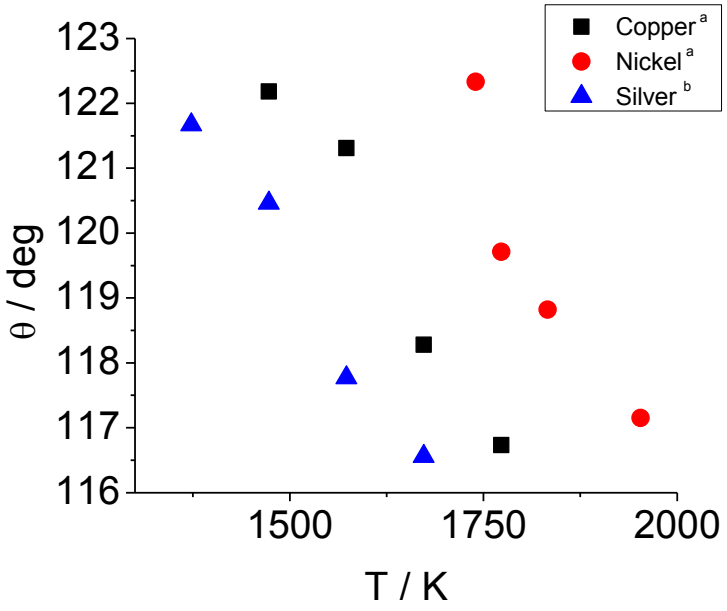

Figure 2.22 Contact angles of silver, copper and nickel on zirconia substrate (superscripts : a - Sotiropoulos *et al.*. [121], **b - Nikopoulos *et al.*** [122])

Effect of Deposition Rate

Assuming an inert substrate ($\gamma_{fv} = \gamma_{fs}$), the effect of deposition rate can be incurred by differentiation of equation (2.53) and (2.54) with respect to $\dot{R}$ to express r^* and ΔG^* as a function of deposition rate. The resulting trends are shown in equation (2.57). This shows that, at constant temperature, both r^* and ΔG^* decrease with deposition rate at constant temperature. Given that $N\,\alpha \exp(-\Delta G^*)$ according to equation (2.55), this result indicates that at higher deposition rates, a greater number of small islands are formed. At high deposition rates, metal films form with lower critical thicknesses.

$$\left(\frac{\delta r^*}{\delta \dot{R}}\right)_T < 0 \qquad \left(\frac{\delta\, \Delta G^*}{\delta \dot{R}}\right)_T < 0 \qquad (2.57)$$

This finding is consistent with derivations from atomistic models from Campbell [123], as well as Frankl and Venables [124] who found the saturation nucleation density to be proportional to $(\dot{R}/\mathrm{D})^{0.5}$, where D is the diffusion coefficient of adatoms on the substrate surface.

The effect of deposition rate on the microstructure of the film has been studied experimentally on a variety of substrates with conflicting results. Early work by Lewis *et al.* [125], on the deposition of LiF and Au on carbon was in line with equation (2.57) and found that higher deposition rates resulted in a greater density of smaller islands. In direct contradiction to this, Levinstein found that slow deposition rates of antimony on collodion produce larger crystallites than faster rates and also that there is a change in crystallinity with deposition rate [126]. Sennett and Scott [127] observed the same trend for silver deposited on formar and found that smaller crystallites form at slower deposition rates. This difference can be attributed to the lack of control over the kinetic energy of the deposited material. Higher evaporation rates, as shown in equation (2.50) can be achieved with higher temperatures, resulting in vaporized atoms with a broad distribution of kinetic energies. In the experimental literature, little care is taken in maintaining constant the kinetic energy of the impinging atoms [103] and heating of the substrate is common, impacting in turn surface diffusion.

Effect of Temperature

Differentiating equation (2.53) and (2.54) with respect to temperature results in the relations given in (2.58).

$$\left(\frac{\delta r^*}{\delta T}\right)_{\dot{R}} > 0 \qquad \left(\frac{\delta \Delta \mathrm{G}^*}{\delta T}\right)_{\dot{R}} > 0 \tag{2.58}$$

From this, an increase in substrate temperature results in an increased density of larger stable nuclei. This is a result of the increased diffusion coefficient for adatoms on the substrate surface, D, as given by equation (2.59)

$$D = (\nu a^2) \exp\left(-\frac{E_{diff}}{RT}\right) \tag{2.59}$$

where a is the square lattice constant, E_{diff} is the free energy of diffusion and ν the prefactor constant.

This is consistent with observations made by Chopra *et al.* [103] who found that increased substrate temperatures yield a larger critical film thickness. The trend is illustrated in Figure 2.23 for the evaporative deposition of silver on a heated glass.

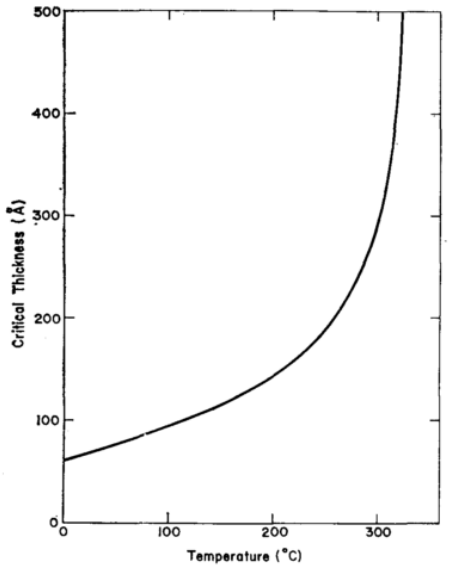

Figure 2.23 Substrate temperature impact on critical thickness of deposit [103]

The critical thickness is expected to increase until it reaches a constant value determined by the thermodynamics of the metal-substrate interactions.

Effect of Substrate Roughness

Inhomogeneity in the substrate causes islands to be pinned in a metastable state during growth resulting in more nucleation sites and a higher island density [128]. The kinetics of nucleation are decided by adatom binding energy, crystal structure of the substrate material, lattice defects, surface steps and contamination [101].

Assessment of the impact of substrate quality on the electrical properties of thin films was done by Toth *et al.* by evaporative deposition of NiCr films on Al_2O_3 ceramic plates (crystalline) and fused silica (amorphous)[129]. It was determined that the critical thickness for the rougher substrate was larger for the alumina plate than for the fused silica. Also, they found that the impact of surface quality on the electrical properties of the film were orders of magnitude greater than that of heating the substrate [129].

Effect of Post-deposition Treatment

Control over the microstructure of thin physical vapor deposited films can be achieved through changes in the deposition conditions, but may also be modified via post-deposition treatment. Thermally-, electrochemically and chemically driven restructuring of thin metal films have been reported for catalyst films used in electrochemical promotion [93, 107], as shown in Figure 2.24. These effects may be desirable, but may also lead to failure of the devices in which they are used.

Electrochemically induced restructuring arises from the formation of bubbles at the interface of compact, dense films, and solid electrolytes, causing the film to rupture and crack [54, 94, 130].

Chemically induced changed to the catalyst morphology have been reported for a variety of reaction systems. Catalytic etching [131] and catalyst oxidation [132] are common forms of

chemically-induced morphological changes in metal film catalysts. The former is associated with the pitting and faceting of the catalyst surface during catalytic reaction, which results in a higher specific surface area [131, 133, 134]. The latter can lead to the formation of highly-porous surface oxides, resulting in an increase in volume which may cause the film to crack or delaminate [86, 92, 131]. If the oxide is catalytically active, the increase in surface area is beneficial, but decrease in the overall conductivity of very thin film makes it less desirable for electrochemical applications [25].

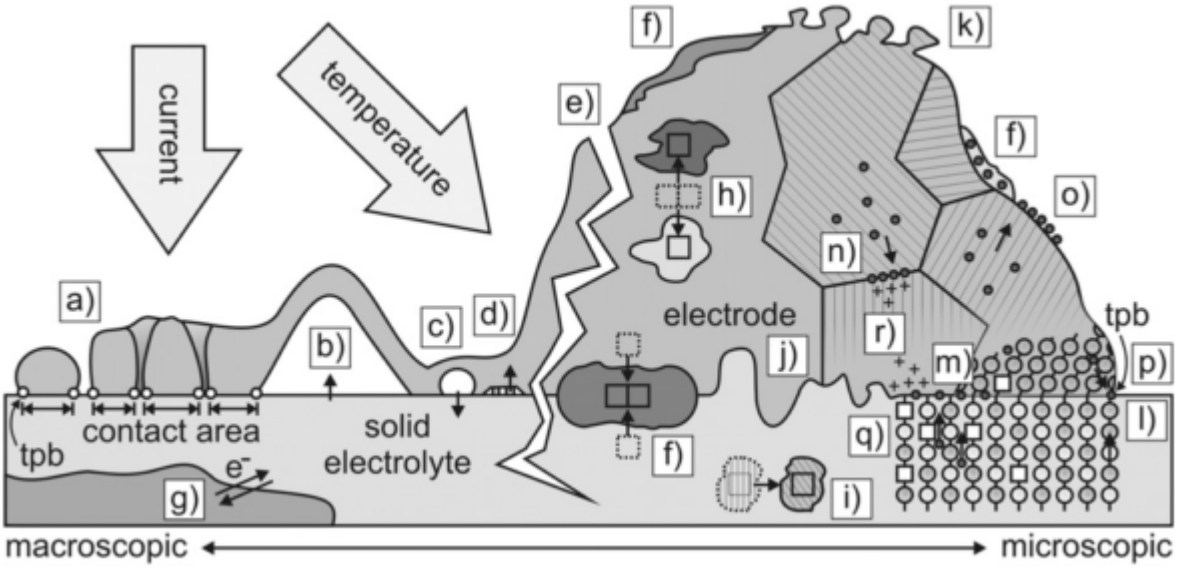

Figure 2.24 Effect of polarization and temperature on film microstructure [130]

Since solid thin films on oxides are generally unstable or metastable, thermally induced restructuring is common [135]. Under operating conditions, mobile metal films dewet causing loss in percolation for very thin films [77]. Dewetting is the breaking of a continuous film aimed at reducing stresses resulting from film and substrate lattice mismatch, which leads to the formation of highly agglomerated films. At temperatures as low as 0.2 T_m for pure metal films, coarsening also occurs and is described by the growth of grains of a preferred orientation through

surface (adatom) or bulk (grain boundary) diffusion to form larger grains with the aims of reducing surface and interface energies [101, 135–137]. At lower temperatures, coarsening of the film is more common through grain boundary (GB) diffusion [101].

Dewetting progresses through at least three distinct stages: hole formation, hole growth and impingement, and ligament breakup [105, 135]. Since dewetting involves atomic transport, the rate of dewetting is strongly temperature and film thickness dependant [105, 107, 135]. The size and spacing of the islands that form through dewetting also decreases with film thickness [135].

2.5 **Research Objectives**

Electrochemical promotion has been shown to modify catalytic behavior for a variety of thin film materials interfaced with solid electrolyte. The behavior of Pt interfaced with YSZ has been widely investigated under polarization using a variety of techniques [31, 33, 34, 73, 138, 139]. Models of Pt/YSZ behavior has been presented in the literature using cyclic voltammetry for a variety of preparation methods [54, 56, 139, 140]. Similarly, a model has been developed for thick sputtered nickel film using cyclic voltammetry studies [38].

The preparation method of the films has been shown to have a significant impact on their behavior under polarization. Concerns over three phase boundary length, YSZ-electrode interface area may lead to an understanding of the processes which occur at these locations. Well defined electrodes are therefore required for careful investigation of mechanisms occurring on a polarized film. Physical vapor deposition methods afford a great degree of control over microstructure while limiting impurities.

The objective of this work is to develop a model of well defined silver, nickel and copper electrodes interfaced with YSZ using cyclic voltammetric techniques. These will be deposited on YSZ pellets via evaporative physical vapor deposition.

2.6 Contribution to Knowledge

Electrochemical promotion of catalysis has been found to apply for a variety of metal and solid electrolyte pairs for a variety of industrially viable reactions [9]. An understanding of the fundamental behaviour of specific thin film materials under polarization is beneficial for assessing the promotability of the catalyst. This quick and inexpensive method of investigating thin films has been applied to a variety of film materials [9, 17, 38, 43, 55–60, 66, 73, 74].

A thick sputtered nickel film (880 nm) interfaced with a polycrystalline yttria-stabilized has been produced and studied in this manner [38]. The following work adds to the knowledge of this material by investigating thinner films (50 and 100 nm) and determining the impact of film thickness on their electrochemical behaviour.

Copper was selected as a material of interest for this work on the basis of its catalytic behaviour [141-143]. Only one study has used this material in the context of EPOC, for which a 400 nm sputtered film was shown to be unpromotable [25]. This work proposes the study of the fundamental response to polarization to determine the cause of this behaviour.

Silver was the material over which the EPOC phenomenon was first discovered, but few studies of the electrochemical response have been attempted on physical vapor deposited films.

In addition to the applicability of these results for EPOC studies, this knowledge can be applied to a variety of electrochemical applications. For instance, films with a marked response to oxygen partial pressure can be used as gas sensors [82, 144]. Additionally, while these

temperatures are not suitable for traditional SOFC, studies of the behaviour of silver and nickel thin films interfaced with YSZ can be applied to μ-SOFC which operate at lower temperatures and employ thin electrolyte films to reduce resistance [105].

2.7 **Reference**

[1] P. Vernoux, M. Guth, X. Li, *Electrochem. Solid-State Lett.*, 12, E9, (2009).

[2] J. H. Shim, Y. B. Kim, J. S. Park, J. An, T. M. Gür, F. B. Prinz, *J. Electrochem. Soc.*, 159, B541, (2012).

[3] W. Zhu, S. . Deevi, *Mater. Sci. Eng., A*, 362, 228–239, (2003).

[4] J. Riegel, H. Neumann, H. Wiedenmann, *Solid State Ionics*, 153, 783–800, (2002).

[5] H. Iwahara, *Solid State Ionics*, 168, 299–310, (2004).

[6] H. Iwahara, *Solid State Ionics*, 77, 289–298, (1995).

[7] T. J. Mazanec, T. L. Cable, J. G. Frye, *Solid State Ionics*, 56, 111–118, (1992).

[8] K. Sundmacher, L. Rihkostruckmann, V. Galvita, *Catal. Today*, 104, 185–199, (2005).

[9] C. G. Vayenas, S. Bebelis, S. Brosda, C. Pliangos, D. Tsiplakides, *Electrochemical Promotion of Catalysis - Promotion, Electrochemical Promotion and Metal Support Interactions* (Kluwer Academic Publishers, New York, 2002), p.574

[10] J. B. Goodenough, *Solid State Ionics*, 94, 17–25, (1997).

[11] S. J. Skinner, J. A. Kilner, *Mater. Today*, 6(3), 30–37, (2003).

[12] S. J. Tauster, *Acc. Chem. Res.*, 20, 389–394, (1987).

[13] C. G. Vayenas, S. Bebelis, I. V. Yentekakis, *Catal. Today*, 11, 303–442, (1992).

[14] S. Balomenou, *Appl. Catal. B.*, 52, 181–196, (2004).

[15] G. Schwab, *Advances in Catalysis, Vol 27* (1978).

[16] F. Solymosi, I. Tombacz, M. Kocsis, *J. Catal.*, 75, 78–93, (1982).

[17] C. G. Vayenas, C. Pliangos, S. Brosda, D. Tsiplakides, *Promotion, Electrochemical Promotion and Metal-Support Interactions : The Unifying Role of Spillover,* In *Catalysis and Electrocatalysis at Nanoparticle Surfaces* (CRC Press, 2003), p.970

[18] J. Nicole, D. Tsiplakides, C. Pliangos, X. E. Verykios, C. Comninellis, C. G. Vayenas, *J. Catal.*, 204, 23–34, (2001).

[19] M. Stoukides, C. G. Vayenas, *J. Catal.*, 70, 137–146, (1981).

[20] C. Wagner, *Adv. Catal.*,21, 323-381, (1970)

[21] M. Stoukides, *J. Catal.*, 69, 18–31, (1981).

[22] A. Katsaounis, *J. Appl. Electrochem.*, 40, 885–902, (2009).

[23] C. Xia, M. Hugentobler, Y. Li, G. Foti, C. Comninellis, W. Harbich, *Electrochem. Comm.*, 13, 99–101, (2011).

[24] F. Gaillard, N. Li, *Catal. Today*, 146, 345–350, (2009).

[25] E. I. Papaioannou, S. Souentie, A. Hammad, C. G. Vayenas, *Catal. Today*, 146, 336–344, (2009).

[26] D. Tsiplakides, S. Balomenou, A. Katsaounis, D. Archonta, C. Koutsodontis, C. G. Vayenas, *Catal. Today*, 100, 133–144, (2005).

[27] I. Constantinou, D. Archonta, S. Brosda, M. Lepage, Y. Sakamoto, C. G. Vayenas, *J. Catal.*, 251, 400–409, (2007).

[28] F. Williams, *Electrochim. Acta*, 47, 1259–1265, (2002).

[29] E. A. Baranova, A. Thursfield, S. Brosda, G. Foti, C. Comninellis, C. G. Vayenas, *J. Electrochem. Soc.*, 152, E40, (2005).

[30] A. de Lucas-Consuegra, F. Dorado, C. Jiménez-Borja, A. Caravaca, P. Vernoux, J. L. Valverde, *Catal. Today*, 146, 293–298, (2009).

[31] C. G. Vayenas, S. Bebelis, S. Ladas, *Nature*, 343, 625–627, (1990).

[32] C. G. Vayenas, S. Bebelis, *Solid State Ionics*, 94, 267–277, (1997).

[33] I. Metcalfe, *J. Catal.*, 199, 247–258, (2001).

[34] C. G. Vayenas, C. G. Koutsodontis, *J. Phys. Chem.*, 128, 182506, (2008).

[35] G. Somorjai, Y. Li, *Introduction to surface chemistry and catalysis* (Wiley, 2010), p. 771.

[36] S. Ladas, S. Kennou, S. Bebelis, C. G. Vayenas, *J. Phys. Chem.*, 97, 8845–8848, (1993).

[37] S. G. Neophytides, D. Tsiplakides, C. G. Vayenas, *J. Catal.*, 428, 414–428, (1998).

[38] S. Souentie, C. Falgairette, C. Comninellis, *J. Electrochem. Soc.*, 157, P49, (2010).

[39] I. Harkness, R. M. Lambert, *J. Catal.*, 152, 211–214, (1995).

[40] I. Constantinou, I. Bolzonella, C. Pliangos, C. Comninellis, C. G. Vayenas, *Catal. Let.*, 100, 125–133, (2005).

[41] L. Basini, C. Cavalca, G. L. Haller, *J. Phys. Chem.*, 98, 10853–10856, (1994).

[42] C. Cavalca, G. Larsen, C. G. Vayenas, H. G.L, *Nature*, 6115–6119, (1993).

[43] S. G. Neophytides, C. G. Vayenas, *J. Phys. Chem.*, 99, 17063–17067, (1995).

[44] J. Janek, M. Rohnke, B. Luerssen, R. Imbihl, *Phys. Chem. Chem. Phys.*, 2, 1935–1941, (2000).

[45] C. G. Vayenas, M. M. Jaksic, S. Bebelis, and S. G. Neophytides, *The Electrochemical Activation of Catalysis*, In *Modern Aspects of Electrochemistry*, vol. 29 (Kluwer Academic, New York, 1996), p. 57.

[46] A. Jaccoud, thesis, Ecole Polytechnique Federale de Lausanne (2007).

[47] J. Janek, C. Korte, *Solid State Ionics*, 116, 181–195, (1999).

[48] R. E. W. Casselton, *J. Appl. Electrochem.*, 4, 25–48, (1974).

[49] M. Nagata, Y. Itoh, H. Iwahara, *Solid State Ionics*, 67, 215–224, (1994).

[50] J. Winkler, *J. Electrochem. Soc.*, 145, 1184, (1998).

[51] T. Kenjo, Y. Yamakoshi, K. Wada, *J. Electrochem. Soc.*, 140, 2151–2157, (1993).

[52] J. Poppe, S. Vo, A. Schaak, E. Schutz, J. Janek, R. Imbihl, *Phys. Chem. Chem. Phys.*, 1, 5241, (1999).

[53] O. Szengasum, E. Djurado, T. Pagnier, N. Rosman, C. Roux, E. Siebert, *Solid State Ionics*, 176, 2599–2607, (2005).

[54] E. Mutoro, B. Luerssen, S. Günther, J. Janek, *Solid State Ionics*, 179, 1214–1218, (2008).

[55] E. J. L. Schouler, *J. Electrochem. Soc.*, 134, 1045, (1987).

[56] C. G. Vayenas, A. Ioannides, S. Bebelis, *J. Catal.*, 67–87, (1991).

[57] J. Yi, A. Kaloyannis, C. G. Vayenas, *Electrochim. Acta*, 38, 2533–2539, (1993).

[58] X. Chen, S. Chan, K. Khor, *Solid State Ionics*, 164, 17–25, (2003).

[59] A. Jaccoud, G. Foti, C. Comninellis, *Electrochim. Acta*, 51, 1264–1273, (2006).

[60] A. Jaccoud, G. Fóti, R. Wüthrich, H. Jotterand, C. Comninellis, *Top. Catal.*, 44, 409–417, (2007).

[61] A. Sevcik, *Collec. Czech. Chem. Commun.*, 13, 349, (1948).

[62] J. E. B. Randles, *Transactions of The Electrochemical Society*, 1, 11-19, (1947).

[63] P. Delahay, *New Instrumental Methods in Electrochemistry, (*Interscience Publishers, 1954), p. 437

[64] S. Srinivasan, E. Gileadi, *Electrochim. Acta*, 11, 321–335, (1966).

[65] A. J. Bard, L. R. Faulkner, *Electrochemical Methods - Fundamentals and Applications* (John Wiley & Sons Inc., 2nd Edition, 2001).

[66] T. Chao, K. J. Walsh, P. S. Fedkiw, *Solid State Ionics*, 47, 277–285, (1991).

[67] M. W. Breiter, K. Leeb, G. Fafilek, *J. of Electroanal. Chem.*, 434, 129–137, (1997).

[68] E. Mutoro, B. Luerssen, S. Günther, J. Janek, *Solid State Ionics*, 180, 1019–1033, (2009).

[69] A. Atkinson, *Rev. Mod. Phys.*, 57, 437-470, (1985).

[70] N. F. Mott, *Transactions of the Faraday Society*, 35, 1175–1177, (1939).

[71] N. Cabrera, N. F. Mott, *Rep. Prog. Phys.*, 163, 163, (1949).

[72] A. S. Khanna, *High temperature oxidation and corrosion* (ASM International, 2002), p. 324.

[73] L. Bultel, *Solid State Ionics*, 166, 183–189, (2004).

[74] F. M. Sapountzi, F. Dorado, S. Souentie, J. L. Valverde, In *7th international conference on environmental catalysis*, Lyon, France, 2012, pp. 7–8.

[75] G. Fóti, A. Jaccoud, C. Falgairette, C. Comninellis, *J. Electroceram.*, 23, 175–179, (2007).

[76] A. Jaccoud, C. Falgairette, G. Foti, C. Comninellis, *Electrochim. Acta*, 52, 7927–7935, (2007).

[77] T. Ryll, H. Galinski, F. Schiettekatte, P. Elser, J. Rupp, A. Bieberle-Hutter, L. J. Gauckler, *Adv. Funct. Mater.*, 21, 565–572, (2011).

[78] M. Salmeron, L. Brewer, G. Somorjai, *Surf. Sci.*, 112, 207–228, (1981).

[79] H. S. Isaacs, L.J Olmer, *J. Electrochem. Soc.*, 129, 436-443, (1982).

[80] T. Jacobsen, B. Zachau-Christiansen, L. Bay, M. Juhl Jørgensen, *Electrochim. Acta*, 46, 1019–1024, (2001).

[81] J. Nielsen, T. Jacobsen, *Solid State Ionics*, 178, 1001–1009, (2007).

[82] E. Shoemaker, M. Vogt, F. Dudek, *Solid State Ionics*, 92, 285–292, (1996).

[83] G. Fafilek, K. Leeb, M. . Breiter, *Solid State Ionics*, 86-88, 1415–1419, (1996).

[84] R. Imbihl, J. Janek, *Solid State Ionics*, 137, 699–705, (2000).

[85] C. Falgairette, thesis, Ecole Polytechnique de Lausanne (2010).

[86] N. Birks, G. Meier, *Introduction to High Temperature Oxidation of Metals* (Edward Arnold, London, ed. 1, 1983), p. 198.

[87] C. G. Vayenas, G. E. Pitselis, *Ind. Eng. Chem. Res.*, 40, 4209–4215, (2001).

[88] E. A. Baranova, G. Fóti, H. Jotterand, C. Comninellis, *Top. Catal.*, 44, 355–360, (2007).

[89] C. Koutsodontis, A. Katsaounis, J. C. Figueroa, C. Cavalca, C. Pereira, C. G. Vayenas, *Top. Catal.*, 39, 97–100, (2006).

[90] F. Dorado, A. De Lucas-Consuegra, P. Vernoux, J. L. Valverde, *Appl. Catal. B.*, 73, 42–50, (2007).

[91] A. Radisic, P. Vereecken, P. Searson, F. Ross, *Surf. Sci.*, 600, 1817–1826, (2006).

[92] M. Ohring, *The material science of thin films* (Academic Press Limited, San Diego, ed. 2, 2002).

[93] R. Imbihl, *Prog. Surf. Sci.*, 85, 241–278, (2010).

[94] A. Toghan, M. Khodari, F. Steinbach, R. Imbihl, *Thin Solid Films*, 519, 8139–8143, (2011).

[95] L. Lizarraga, M. Guth, a. Billard, P. Vernoux, *Catal. Today*, 157, 61–65, (2010).

[96] C. Koutsodontis, a. Hammad, M. Lepage, Y. Sakamoto, G. Fóti, C. G. Vayenas, *Top. Catal.*, 50, 192–199, (2008).

[97] E. A. Baranova, A. Thursfield, S. Brosda, G. Fóti, C. Comninellis, C. G. Vayenas, *Catal. Let.*, 105, 15–21, (2005).

[98] J. D. Plummer, M. Deal, P. B. Griffin, *Silicon VLSI technology: Fundamentals, practice and modeling* (Prentice Hall, 2000), p. 817.

[99] C. Xia, M. Hugentobler, C. Comninellis, W. Harbich, *Electrochem. Comm.*, 12, 1551–1554, (2010).

[100] J. L. Vossen, W. Kern, *Thin Film Processes II,* (Academic Press Inc., 1991), p. 866.

[101] I. Petrov, P. Barna, L. Hultman, J. E. Greene, *J. Vac. Sci. Technol., A*, 21, S117, (2003).

[102] D. Sotiropoulou, *Surf. Sci.*, 408, 182–189, (1998).

[103] K. L. Chopra, *J. Appl. Phys.*, 39, 1874–1881, (1968).

[104] J. V Barth, G. Costantini, K. Kern, *Nature*, 437, 671–9, (2005).

[105] N. J. Simrick, J. A. Kilner, A. Atkinson, *Thin Solid Films*, 520, 2855–2867, (2012).

[106] W. . Maskell, N. M. Sammes, B. C. Steele, *J. Appl. Phys.*, 20, 99–104, (1987).

[107] H. C. Kim, T. L. Alford, D. R. Allee, *Appl. Phys. Let.*, 81, 4287, (2002).

[108] K. Seal, M. Nelson, Z. Ying, D. Genov, A. Sarychev, V. Shalaev, *Phys. Rev. B*, 67, 1–13, (2003).

[109] R. Saxena, M. Frederick, G. Ramanath, W. Gill, J. Plawsky, *Phys. Rev. B*, 72, 1–7, (2005).

[110] I. M. Rycroft, B. L. Evans, *Thin Films*, 6090, 283–288, (1996).

[111] D. P. Tracy, D. Knorr, *J. Electron. Mater.,* 22, 611–616, (1993).

[112] N. Kaiser, *Appl. Opt*., 41, 3053–60, (2002).

[113] S. E. Roark, K. L. Rowlen, *Anal. Chem.*, 66, 261–270, (1994).

[114] J. S. Agustsson, U. B. Arnalds, A. S. Ingason, K. B. Gylfason, K. Johnsen, S. Olafsson, J. T. Gudmundsson, *Appl. Surf. Sci.*, 254, 7356–7360, (2008).

[115] S. Kirkpatrick, *Rev. Mod. Phys.*, 45, 574–588, (1973).

[116] K. Sieradzki, K. Bailey, T. L. Alford, *Appl. Phys. Let.*, 79, 3401, (2001).

[117] S. Wagner, A. Pundt, *Phys. Rev. B: Condens. Matter*, 78, 1–14, (2008).

[118] A. Kapitulnik, G. Deutscher, *J. Stat. Phys.,* 36, 815–826, (1984).

[119] M. Finnis, *J. Phys. Condens. Matter*, 8, 5811–5836, (1996).

[120] W. M. Haynes, ed., *CRC Handbook of Chemistry and Physics*, 93rd Edition (CRC Press/Taylor and Francis , Internet Version 2013)

[121] D. Sotiropoulou, P. Nikolopoulos, *Journal of Material Science*, 28, 356–360, (1993).

[122] P. Nikolopoulos, D. Sotiropoulou, *J. Mat Sci. Let.*, 6, 1429–1430, (1987).

[123] C. T. Campbell, *Surf. Sci. Rep.*, 27, 1–111, (1997).

[124] D. R. Frankl, J. A Venables, *Adv. Phys.*, 19, 409–456, (1970).

[125] B. Lewis, D. . Campbell, *J. Vac. Sci. Technol., B*, 4, 209–218, (1967).

[126] H. Levinstein, *J. Appl. Phys.*, 20, 306, (1949).

[127] R. S. Sennett, G. D. Scott, *J. Opt. Soc. Am.*, 40, 203, (1950).

[128] P. M. Duxbury, M. Dubson, X. Yu, G. Jeffers, *Europhys. Lett.*, 26, 601–606, (1994).

[129] L. Toth, *Vacuum*, 37, 103–106, (1987).

[130] E. Mutoro, S. Gunther, B. Luerssen, I. Valov, J. Janek, *Solid State Ionics*, 179, 1835–1848, (2008).

[131] T. We, J. Phillips, 41,359-421, (1996).

[132] C. Bartholomew, *Appl. Catal.*, A, 212, 17–60, (2001).

[133] M. Flytzani-Stephanopoulos, L. . Schmidt, R. Caretta, *J. Catal.*, 64, 346–355, (1980).

[134] M. Flytzani-Stephanopoulos, L. . Schmidt, *Prog. Surf. Sci.*, 9, 83-111, (1979).

[135] C. V. Thompson, *Annu. Rev. Mater. Sci.,* 42, 399–434, (2012).

[136] H. Frost, C. . Thompson, D. Walton, *Acta Metallurgica*, 38, 1455–1462, (1990).

[137] C. V Thompson, *Annual Review of Material Science*, 20, 245–268, (1990).

[138] L. Bay, T. Jacobsen, *Solid State Ionics*, 93, 201–206, (1997).

[139] H. Pöpke, E. Mutoro, B. Luerßen, J. Janek, *Catal. Today*, 202, 12–19, (2013).

[140] J. Mizusaki, K. Amano, S. Yamauchi, K. Fueki, *Solid State Ionics*, 22, 313–322, (1987).

[141] M. V. Twigg, M. S. Spencer, Appl. Cat. A, 212, 161–174, (2001)

[142] K. V. R. Chary, G. V. Sagar, C. S. Srikanth, V. V. Rao, J. Phys. Chem B, 111, 543–50, (2007).

[143] A. Baikerb, A. Wokaun, Phys. Chem. Chem. Phys., 1, 5071–5080, (1999).

[144] J. Riegel, H. Neumann, H. Wiedenmann, Solid State Ionics, 153, 783–800, (2002).

Chapter 3 Yttria Stabilized Zirconia Pellet Synthesis

This chapter covers the synthesis of 8 mol% yttria stabilized zirconia pellets from pressed and sintered powders. The result was opaque, non-porous, white polycrystalline pellets with a density greater than 98% of the maximum theoretical density. The ionic conductivity was also characterized using electrochemical impedance spectroscopy (EIS) over temperature of 300 °C to 400 °C between frequencies of 1 Hz and 100 kHz and compared with commercially prepared pellets of similar composition. The laboratory prepared samples were found to have lower bulk conductivities than commercially obtained pellets as well as a wider distribution of densities, but results are consistent with literature values for similarly prepared pellets.

3.1 **Introduction**

Solid electrolytes are materials which contain mobile charged ions. [1]. The ionic conductivity is directly related to the presence of Frenkel and Schottky defects which manifest as lattice vacancies or interstitial sites, respectively [2]. With the application of an electric field, charged species migrate through the solid via these sites. Ionic conductors are available in a variety of forms (amorphous, crystalline), carrier species (anionic/cationic, monovalent/polyvalent) and operating temperatures. Historically, crystalline materials have been used for solid oxide fuel cells (SOFC) [3–6], solid state electrolyzers [7], gas sensors [8, 9] and electrochemcial promotion [10–16], while amorphous materials are favored for lower temperature applications, such as solid state lithium batteries [17–19]. Electrochemical promotion has been shown to occur with a variety of ion-conducting supports: Beta-Al_2O_3 (K^+) [20–23] NASICON (Na^+) [24], lathanum stabilized manganate (LSM) [25], gadolinium doped

ceria (O^{2-}) [26] and stabilized zirconias [11, 27–33]. In addition to electrochemical promotion, solid electrolytes are used in solid oxide fuel cells [3, 34], gas sensors [4], electrolyzers [5, 6] and yttria stabilized zirconia (YSZ) is the popular owing to its mechanical strength, thermal stability and high ionic conductivity at temperatures greater than 300 °C [35].

Zirconia is crystalline material with a monoclinic structure at ambient temperatures and transitions to tetragonal (1480 K) and cubic (2650 K) structures at increasing temperatures [36]. These phase transitions cause zirconia to crack under rapid cooling and is therefore stabilized with yttria, which simultaneously results in higher ion conductivities. Yttria doping from 0 to 12 is possible, but fully stabilized zirconias contain 8-12 mol% yttria, where ionic conductivity is maximized [37]

Yttria stabilized zirconia pellets used for electrochemical promotion, SOFCs, gas sensors and electrolyzers are pressed and sintered from corresponding powders, which may be prepared via coating, co-milling or coprecipitation methods [38]. The conductivity of the resulting pellet is affected by the degree of densification and the grain size. Densities on the order of 98% or greater of the theoretical maximum of 5.958 $g.cm^{-3}$ [39] are typical to reduce pore resistances [1, 40]. The degree of densification of the pellet is primarily dependant on the sintering temperature [1]**,** while inter-grain resistances can be reduced with longer sinter times owing to the growth of grains [41]. The most common methods for evaluating the resistance of solid electrolyte materials are the current interruption method [42, 43] and electrochemical impedance spectroscopy [40, 44, 45]. The current interruption method consists of applying a current step across the electrolyte and measuring the response after interruption of current. Electrolyte resistance is comprised of compensated and uncompensated resistances, and this method allows the measurement of the uncompensated resistance, while the compensated resistance is

accounted for in the correct placement of the reference electrode [42]. Electrochemical impedance spectroscopy measures the responses to AC currents applied across the electrolyte at a variety of frequencies, resulting in a Bode plot of impedance measurements from which both bulk, inter-grain and total resistances can be measured. Impedance spectroscopy is more complex than the current interruption method, but it is the preferred method for resistance measurements because of the information it can provide. The pellet may be further characterized by observation of its microstructure and calculation of densification [41].

Due to the scarcity of manufacturers of YSZ pellets for electrochemical research and therefore, their high cost, the objective of this chapter is to present a method by which YSZ pellets of the desired size may be synthesized in laboratory setting. Characterization of these pellets in terms of ionic conductivity and density will be compared to those of commercially procured specimens and literature values.

Electrochemical Impedance Spectroscopy (EIS)

Electrochemical impedance spectroscopy (EIS) is a versatile tool used to characterize electrode processes and complex interfaces through measured responses to low amplitude alternating current (AC). The impedance of a material is its opposition to AC flow and links the current to the electrical potential according to this generalized form of Ohm's law, given by equation (3.1)

$$\dot{V} = \dot{I}Z \tag{3.1}$$

Where $\dot{V}$ and $\dot{I}$ are the phasors of electrical potential and current, respectively. Alternating current is described mathematically by equations (3.2) and (3.3).

$$v(t) = A_v sin(\omega_v t) \tag{3.2}$$

$$i(t) = A_i sin(\omega_i t) \tag{3.3}$$

Where A_v and A_i are the amplitude of current and electrical potential oscillation and ω_v adn ω_i are their respective frequencies.

Since both amplitude and period are impacted by impendence, it is practical to express impedance using a complex number of the form equation (3.4)

$$Z = X - jR \tag{3.4}$$

where R is the resistance and X, the reactance, which is the opposition to current due to capacitance or inductance within the substance. Experimental impendance data of the electrochemical system O_2, *Me*/YSZ/*Me*, O_2 can be modeled as the equivalent circuit given in Figure 3.1.

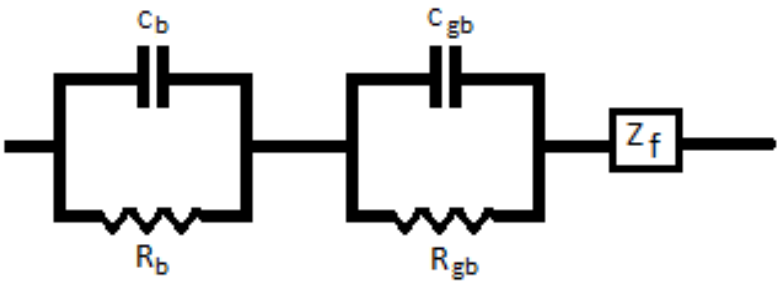

Figure 3.1 Equivalent circuit of the O_2, *Me*/YSZ/*Me*, O_2 system [46]

where C_b, R_b are bulk capacitance and resistances, C_{gb}, R_{gb} are grain boundary capacitance and resistances and Z_f represents impedance responses due to Faradaic processes occurring at the electrode surface.

When impedance is measured over a range of current frequencies, the imaginary (Z'') and real (Z') parts of the impedance are displayed in a Nyquist diagram, shown in Figure 3.2.

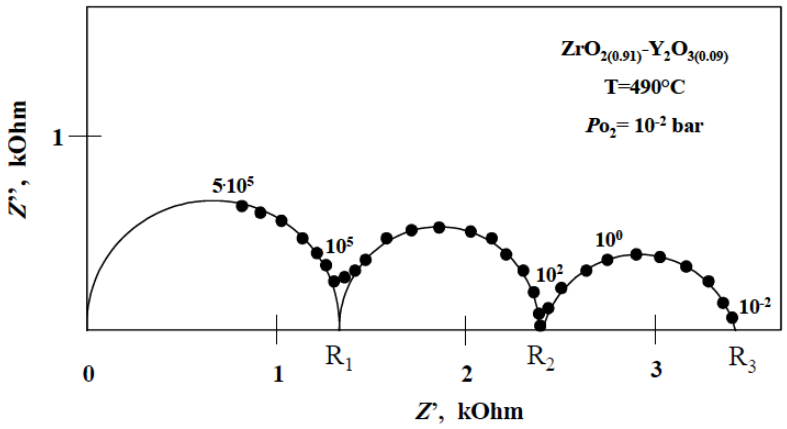

Figure 3.2 Representative Nyquist plot for 8 mol% YSZ [46]

The bulk and inter-grain contributions are shown by R_1 and R_2, respectively, while R_3 accounts for Faradaic processes occurring at the electrode surface. From these resistances, the conductivities can be determined from equation (3.5).

$$\rho = \frac{1}{R\left(\frac{A}{x}\right)} \tag{3.5}$$

Where R is the resistance, A the cross-sectional area of the electrodes and x the thickness of the pellet.

Densification

The densification of a material is the percentage of the theoretical maximum density achieved during sintering. The densification is an indication of the conductivity of the material; however, grain sizes and distribution also have a noted effect [2]. For electrochemical promotion,

a densification of 98% or higher is used in literature. The theoretical maximum density of YSZ (8 mol %) is 5.985 $g.cm^{-3}$ [2].

To obtain an accurate measurement of the pellets density, the precise measurement of the volume is needed. Calculating volume from physical dimensions is not sufficiently accurate and so techniques based on the Archimedes principle are preferred. In a typical densification measurement experiment, a pellet suspended in water by a wire is artificially given the density of water. Recording the difference in mass and subtracting from it the contribution of the wire an accurate measure of the volume of the pellet, making the density calculation simply given by equation (3.6). The densification, by extension is expressed by equation (2.7).

$$\rho_{pellet} = \frac{m_{pellet}}{V_{pellet}} = \frac{m_{pellet}}{V_{Pellet+wire} - V_{wire}} \tag{3.6}$$

$$\text{Densification} = \frac{\rho_{Pellet}}{\rho_{\text{theoretical max}}} \times 100 \tag{3.7}$$

The densification of the synthesized pellet can then be compared to that found in commercial pellets.

3.2 **Experimental**

3.2.1 Synthesis of YSZ Pellets

Green YSZ pellets are formed from 1.5 g of 8 mol% YSZ powder (TOSOH) pressed at 5000 psi in a stainless steel cylindrical die (ID = 25 mm). Once cast, the green pellets were transferred to an alumina plate and placed in a Carbolite furnace (SPECS) where they are pre-treated at 1000°C in air and subsequently sintered at 1500 °C for 6 hours. The resulting pellets are 1 mm x 18.5 mm.

These pellets are then sandblasted on each side for 10 s and subsequently sonicated in acetone for 10 minutes, rinsed in DI water and de-greased in iso-propanol for 10 minutes. The pellet is allowed to dry in air.

The density of the pellets is determined from these dried pellets. Impedance measurements were performed on a two electrode cell configuration with silver electrodes. Two Ag electrodes with thickness 200 nm were deposited symmetrically via physical vapor deposition to a thickness of 200 nm with a geometric surface area of 2.5 cm^2. Gold wires were anchored to the pellet using ceramic Zirconia paste (AREMCO) and electrical contact established with gold paste (Gwent), which was subsequently calcined at 550 °C for 1 hour. Impedance measurements were compared with results obtained from commercially available YSZ pellets and literature data.

3.3 **Characterization of YSZ Pellets**

Electrochemical Impedance Spectroscopy (EIS)

Impedance measurements were taken for prepared YSZ pellets and compared to commercially available YSZ pellets. Pellets were placed in a reactor 200 mL Pyrex reactor as shown in Figure 4.5a (Chapter 4). Impedance measurements were taken for frequencies of 100 kHz to 1 Hz with AC amplitude of 40 mV at temperatures of 300, 320, 340, 360, 380 and 400 °C in air. These measurements were carried out on the Bio-Logic potentiostat with EC lab software package.

Figure 3.3 shows the Nyquist plot of commercial (YSZ-C) and synthesized (YSZ-L) YSZ pellets. With increasing temperature, the both grain boundary and bulk semicircles shrink, indicating a decrease in resistance with temperature.

The first semicircle is attributed to the resistance in the material bulk. The lab produced pellet has higher bulk resistance over all temperatures. The grain boundary contribution is expected to appear between frequencies of 10^5 and 10^2 Hz and in most scan is small hard to deconvolute from grain boundary resistance and the Faradaic process contributions at higher scan rates.

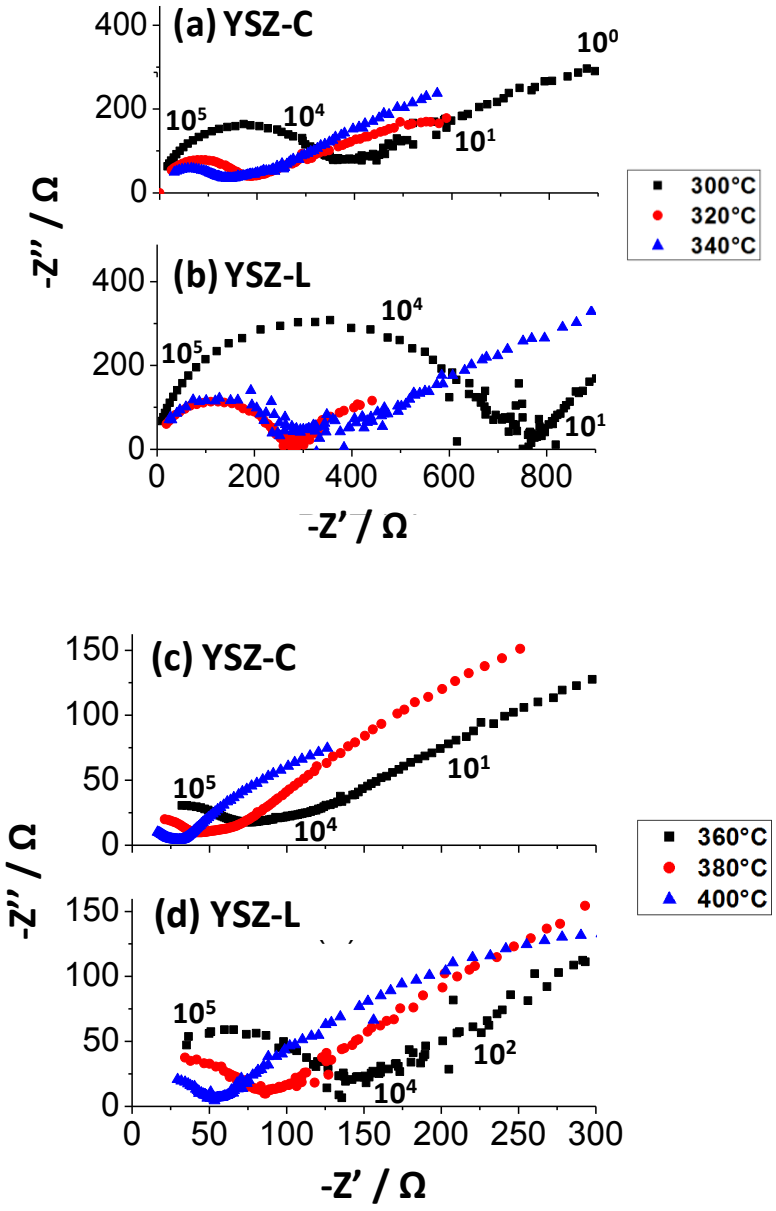

Figure 3.3 Nyquist plot of YSZ-L and YSZ-C at (a-b) 300-360 °C and (c-d) 380-400°C, labeled with frequency (Hz)

From these, total, grain boundary and bulk conductivities were calculated and shown in Figure 3.4

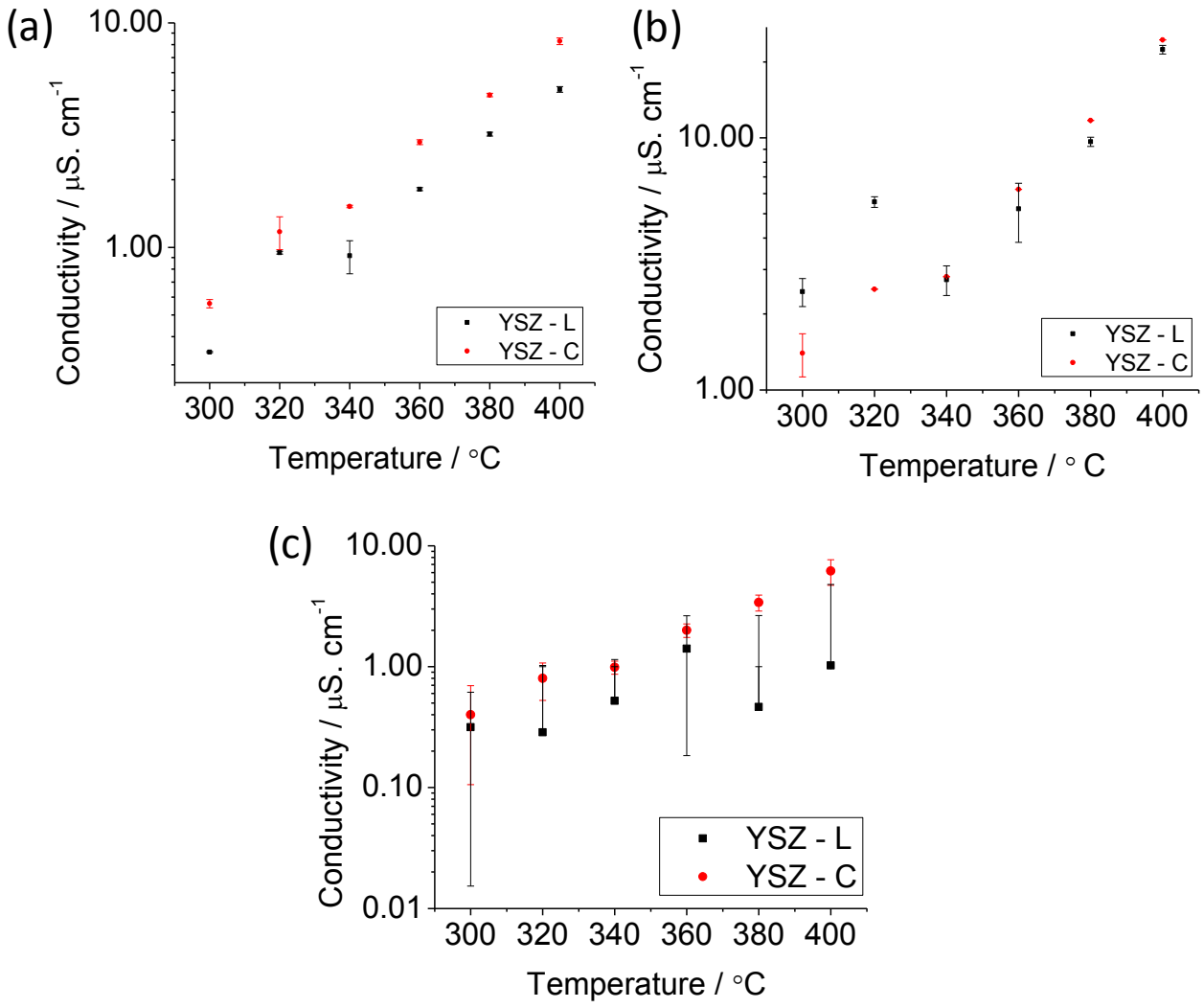

Figure 3.4 Bulk (a), grain boundary(b) and total conductivity(c) for Commercial pellets (YSZ-C) and pellets produced in a laboratory setting (YSZ-L)

The conductivities follow a logarithmic increase with respect to temperature. This increase in conductivity with temperatures is due to the increase in mobility of the O^{2-} ions through both bulk and grain boundaries. These results presented in Figure 3.4 are summarized in

Table 3.1 and shown extrapolated to 1000°C in order to compare with literature values available for SOFC applications.

Table 3.1 Conductivity of YSZ Pellets

Temperature	YSZ-L			YSZ-C		
°C	Bulk $\mu S.cm^{-1}$	Grain Boundary $\mu S.cm^{-1}$	Total $\mu S.cm^{-1}$	Bulk $\mu S.cm^{-1}$	Grain Boundary $\mu S.cm^{-1}$	Total $\mu S.cm^{-1}$
300	0.34	2.45	0.30	0.58	1.51	0.42
320	0.94	5.56	0.73	1.13	2.22	0.75
340	0.91	2.74	0.69	1.63	3.47	1.11
360	1.82	5.23	1.30	2.98	6.11	2.01
380	3.19	9.64	2.12	4.91	10.27	3.32
400	5.05	22.4	3.72	8.37	24.49	6.24
1000*	-	-	10.0	-	-	32.0

**extrapolated using logarithmic curve fitting*

In both commercial and synthesized YSZ pellets the bulk conductivity is the limiting factor, resulting in a reduced overall conductivity. Bulk conductivity is a function of the starting material and so cannot be altered by variation in synthesis methods. Since both pellets were made from commercially available TOSOH 8YT powder, this discrepancy can be attributed to batch-wise variations in the manufacturing process or the use of additives. Binders are additives mixed in with the ceramic powder before pressing to increase the stability of the resulting pellets prior to sintering. No additives were used in the synthesis method proposed above since impurities affect the microstructure and conductivity of the electrolyte [47].

In literature, the conductivity of YSZ pellets is reported at much higher temperatures for their use in solid oxide fuel cells. Gibson *et al.* reports conductivities of 16 S cm^{-1} at 1000°C [41] for samples pressed and sintered from commercial TOSOH powders, which is orders of magnitude smaller than those found in the samples prepared in this study. Extrapolating from

experimental data, the total conductivity of the YSZ pellets are 32 and 10 $\mu S.cm^{-1}$, for commercial and lab-produced samples respectively.

Densification

The volume of synthesized YSZ pellets was measured using a Denver Instruments TP-64 balance ($\pm$0.1 mg) and 50 mL of DI water in a small beaker. A pellet holder was fashioned out of stainless steel wire and its submerged volume subtracted from that of the pellet. Pellets were thoroughly dried before submerging and no bubbles were observed during testing. Figure 3.5 shows the calculated densification of the pellets.

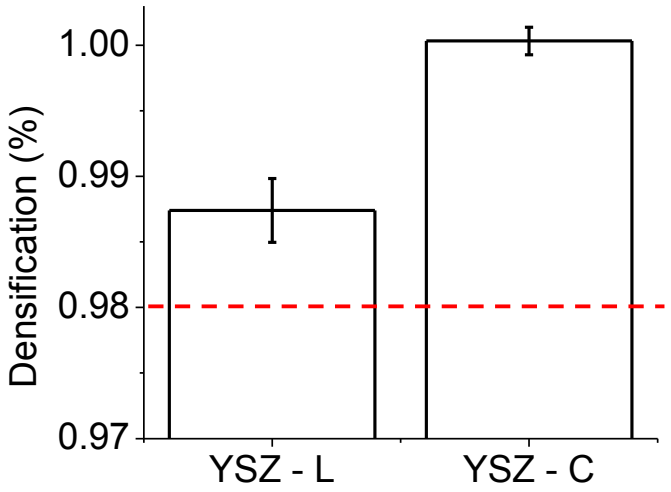

Figure 3.5 Densification of synthesized and commercially available YSZ pellets

The synthesized pellets have an average densification above the required 98% quoted in the literature, but show much lower density than commercially available pellets, which are effectively fully densified. In addition to a higher degree of densification, the commercial pellets show less variability in density across those tested.

3.4 **Conclusion**

Yttria stabilized zirconia pellets were successfully synthesized from commercially available 8 mol% YSZ powder. Pressed pellets were formed from TOSOH 8 mol% YSZ powder at 5000 psi. A pre-treatment of 1 hour at 1000°C was used to remove impurities and then sintered at 1500°C for 6 hours to achieve densification of 98.74 ± 0.002 % as measured using the Archimedes method. These pellets were less dense than commercially available pellets, with measured densification of 100.000 ± 0.001%. The greater than 100% densification of commercial pellets can be attributed to the presence of additive and sintering agents in the starting material.

Bulk and grain boundaries conductivities were measured with electrochemical impedance spectroscopy for a temperature range of 300-400°C and the frequency range of 1Hz to 100 kHz. Grain boundary conductivities were found to be consistent between samples while bulk conductivities in commercial samples were double that of lab-produced samples over the studied temperature range. Extrapolated data from lab-produced pellets show a conductivity of 10 $\mu.cm^{-1}$ which is comparable to literature value of 16 $\mu.cm^{-1}$ but smaller than 32 $\mu.cm^{-1}$ which was calculated for commercial pellets

3.5 **References**

[1] S. P. S. Badwal, J. Drennan, *J. Mat. Sci.*, 22, 3231–3239, (1987).

[2] S. Geller, *Solid Electrolytes,* vol. 21, (Springer-Verlag,1977)., p.229

[3] W. Zhu, S.Deevi, *Mater. Sci. Eng., A*, 362, 228–239, (2003).

[4] S. McIntosh, R. J. Gorte, *Chem. Rev.,* 104, 4845–65, (2004).

[5] F. T. Ciacchi, K. M. Crane, S. P. S. Badwal, *Solid State Ionics*, 73, 49–61, (1994).

[6] A. Cantos-Gómez, R. Ruiz-Bustos, J. van Duijn, *Fuel Cells*, 11, 140–143, (2011).

[7] H. Iwahara, *Solid State Ionics*, 168, 299–310, (2004).

[8] J. Riegel, H. Neumann, H. Wiedenmann, *Solid State Ionics*, 153, 783–800, (2002).

[9] E. Shoemaker, M. Vogt, F. Dudek, *Solid State Ionics*, 92, 285–292, (1996).

[10] J. Pritchard, *Nature*, 343, 592–593, (1990).

[11] F. Williams, *Electrochim. Acta*, 47, 1259–1265, (2002).

[12] I. V. Yentekakis, A. Palermo, N. C. Filkin, M. S. Tikhov, R. M. Lambert, *J. Phys. Chem. B*, 101, 3759–3768, (1997).

[13] A. Katsaounis, *J. Catal.*, 226, 197–209, (2004).

[14] E. I. Papaioannou, S. Souentie, F. M. Sapountzi, A. Hammad, D. Labou, S. Brosda, C. G. Vayenas, *J. Appl. Electrochem.*, 40, 1859–1865, (2010).

[15] A. Toghan, L. M. Rösken, R. Imbihl, *ChemPhysChem*, 11, 1452–9, (2010).

[16] R. Imbihl, *Prog. Surf. Sci.*, 85, 241–278, (2010).

[17] N. Machida, H. Yamamoto, S. Asano, T. Shigematsu, *Solid State Ionics*, 176, 473–479, (2005).

[18] J. B. Bates, G. R. Gruzalski, *Solid State Ionics,* 70/71, 619-628 (1994).

[19] Y. Ooura, N. Machida, M. Naito, T. Shigematsu, *Solid State Ionics*, 225, 350–353, (2012).

[20] A. de Lucas-Consuegra, A. Caravaca, M. J. Martín de Vidales, F. Dorado, S. Balomenou, D. Tsiplakides, P. Vernoux, J. L. Valverde, *Catal. Comm*., 11, 247–251, (2009).

[21] F. Dorado, A. De Lucas-Consuegra, P. Vernoux, J. L. Valverde, *Appl. Catal. B*., 73, 42–50, (2007).

[22] A. Lucas-Consuegra, F. Dorado, C. Jiménez-Borja, J. L. Valverde, *J. Appl. Electrochem.*, 38, 1151–1157, (2008).

[23] A. de Lucas-Consuegra, F. Dorado, C. Jimenezborja, J. L. Valverde, *Appl. Catal. B.*, 78, 222–231, (2008).

[24] P. Vernoux, F. Gaillard, C. Lopez, E. Siebert, *J. Catal.*, 217, 203–208, (2003).

[25] V. Roche, E. Siebert, M. C. Steil, J. P. Deloume, C. Roux, T. Pagnier, R. Revel, P. Vernoux, *Ionics*, 14, 235–241, (2008).

[26] R. Karoum, V. Roche, C. Pirovano, R.-N. Vannier, A. Billard, P. Vernoux, *J. Appl. Electrochem.*, 40, 1867–1873, (2010).

[27] S. Souentie, A. Hammad, S. Brosda, G. Foti, C. G. Vayenas, *J. Appl. Electrochem.*, 38, 1159–1170, (2008).

[28] C. Koutsodontis, A. Hammad, M. Lepage, Y. Sakamoto, G. Fóti, C. G. Vayenas, *Top. Catal.*, 50, 192–199, (2008).

[29] I. Constantinou, D. Archonta, S. Brosda, M. Lepage, Y. Sakamoto, C. G. Vayenas, *J. Catal.*, 251, 400–409, (2007).

[30] C. Pliangos, C. Raptis, T. Badas, C. G. Vayenas, *Solid State Ionics*, 136-137, 767–773, (2000).

[31] G. Foti, O. Lavanchy, C. Comninellis, *J. Appl. Electrochem.*, 30, 1223–1228, (2000).

[32] Y. Sakamoto, K. Okumura, H. Shinjoh, M. Lepage, S. Brosda, *Catal. Today*, 146, 299–307, (2009).

[33] X. Li, P. Vernoux, *Appl. Catal. B.*, 61, 267–273, (2005).

[34] J. H. Shim, Y. B. Kim, J. S. Park, J. An, T. M. Gür, F. B. Prinz, *J. Electrochem. Soc.*, 159, B541, (2012).

[35] C. G. Vayenas, S. Bebelis, S. Brosda, C. Pliangos, D. Tsiplakides, *Electrochemical Promotion of Catalysis - Promotion, Electrochemcial Promotion and Metal Support Interactions* (Kluwer Academic Publishers, New York, 2002)

[36] M. Munoz, S. Gallego, J. Beltran, J. Cerda, *Surf. Sci. Rep.*, 61, 303–344, (2006).

[37] N. Q. Minh, *J. Am. Ceram. Soc.*, 765, 563–588, (1993).

[38] A. Jaccoud, G. Fóti, R. Wüthrich, H. Jotterand, C. Comninellis, *Top. Catal.*, 44, 409–417, (2007).

[39] ICDD, *PDF Card no. 30-1468* (Newton Square, USA, 1980).

[40] E. J. L. Schouler, N. Mesbahi, G. Vitter, *Solid State Ionics*, 9-10, 989–996, (1983).

[41] I. R. Gibson, G. P. Dransfield, *J. Mat. Sci.*, 33, 4297–4305, (1998).

[42] D. Fletcher, *Instrumental Methods in Electrochemistry* (Hordwood Publishing, 2001), p. 443.

[43] J. C. Myland, K. B. Oldham, *Anal. Chem.*, 72, 3972–80, (2000).

[44] J. Goff, W. Hayes, S. Hull, M. Hutchings, K. Clausen, *Phys. Rev. B: Condens. Matter*, 59, 14202–14219, (1999).

[45] HJ. Winand, J. Depireux., *Europhys. Lett*. 8(5), 447-452 (1989)

[46] C. Desportes, M. Duclot, P. Fabry, J. Fouletier, A. Hammou, M. Kleitz, E. Siebert, J.-L. Souquet, *Electrochimie des Solides* (Pres Universitaire de Grenoble, 1994).

[47] Z. G. Lv, P. Yao, R. S. Guo, F. Y. Dai, *Mater. Sci. Eng., A*, 458, 355–360, (2007).

Chapter 4 Nickel Thin Films Interfaced with Yttria-Stabilized Zirconia

Using *in-situ* resistance measurements, the critical thickness of nickel thin films on YSZ was determined to be 3.0 nm $\pm$ 0.4 nm for a deposition rate of 0.5 nm. To ensure fully percolated films over the course of testing, 50 and 100 nm nickel thin films were used to investigate the response of nickel thin films interfaced with YSZ to polarization. For this, cyclic voltammetry techniques similar to those used by Souentie *et al.* [1] were used. The model proposed for thicker (880 nm) sputtered nickel thin films presented by Souentie *et al.* [1] is compared with that developped in for 50 nm and 100 nm evaporated thin films in this chapter. The 50 nm film was found to form NiO along the three phase boundary of the YSZ/Ni/O_2, while in 100 nm nickel films, the oxides grow outward towards the Ni-YSZ interface. This behavior is reflected in oxide growth kinetics that follows neither a logarithmic nor, as the work by Souentie *et al.* [1] illustrates, a parabolic reaction rate expression.

4.1 Introduction

Nickel is a low cost catalyst material commonly used in hydrogenation reaction [1], steam reforming [2] and methanation reactions [3]. It also features prominently in electrochemical literature because of its low charge transfer resistance and good electrocatalytic ability for hydrogen oxidation [4]. Nickel is the most common anode material in high temperature solid oxide fuel cells (SOFC) due to its low cost, chemical stability in reducing atmospheres and high temperatures and thermal expansion coefficient (13.4 x10^{-6} K^{-1}) [4] compatible with that of YSZ

(6-8 x10^{-6} K^{-1}) [5–7]. Drawbacks of nickel include the formation of carbon deposits for fuels with hydrocarbon contaminants and coarsening and agglomeration at elevated temperatures [6].

Based on its catalytic and electrocatalytic pedigree, the electrochemical promotion of nickel films presents an interesting avenue of investigation. Thus far, the electrochemical promotion to nickel thin films has not been attempted in literature; although, investigation of nickel impregnated carbon nanofibers have shown to mildly promote the hydrogenation of CO_2 with a rate enhancement ratio of 1.2 achieved at -0.75V [8]. A model for the polarization of nickel has been proposed by Souentie *et al.* [9] for sputtered 880 nm nickel film interfaced with polycrystalline YSZ that has been subjected to polarization in 20 kPa oxygen, as discussed in Section 2.2.3. The following work proposes an extension of this work to include 50 nm and 100 nm nickel films.

Understanding of the oxidation mechanisms of pure nickel under operating conditions as well as the polarization of nickel in aqueous electrochemistry allows for a comprehensive starting point for the study of solid state models.

4.1.1 Oxidation Model

The oxidation of nickel at high temperatures is well studied in literature as it proceeds via simple mechanisms, forming a compact, adherent NiO scale. The overall reaction may be expressed by equation (4.1).

$$\mathrm{Ni} + \frac{1}{2}\mathrm{O}_{2(g)} \rightleftarrows \mathrm{NiO} \tag{4.1}$$

Above 700°C, nickel forms a compact, thermodynamically stable, adherent p-type semiconducting scale which forms from the migration of Ni^{+} or Ni^{2+} to the gas exposed surface of the oxide according to Wagner's theory [10]. The oxide formation is limited by the diffusion

of these cationic species through the oxide and follows a parabolic rate expression, given by equation (2.47) with rate constant proportional to $p_{O_2}^{\frac{1}{6}}$ in the gas phase [10].

At low partial pressures ($5x10^{-3}$ Torr) of oxygen and temperatures between 200-340°C, initial oxidation proceeds rapidly and uptake of oxygen stabilizes to a logarithmic rate of oxidation. For temperatures in excess of 340°C, after an initial logarithmic oxide formation (30 - 40 Å), subsequent oxides form according to a parabolic reaction rate. In this temperature range a variety of oxidation kinetics models have been proposed including, parabolic [11], two stage logarithmic [12, 13] as well as logarithmic followed by quartic [14] oxidation rates. These inconsistencies were attributed to the dependence of the pre-treatment of nickel and nature of the exposed surface on the mechanism and rate of oxide growth [15].

4.1.2 Aqueous Nickel Cyclic Voltammetry

While the formation of chemical oxides of nickel is well studied in gas phased systems, the electrochemical response to polarization has not been extensively studied. However, the electrochemistry of nickel electrodes in aqueous medium is well established because nickel is an important electrode material in water electrolysis [16–19] and NiH batteries [20, 21]. It is possible, as shown in work by Jaccoud *et al.*, to draw a link between the aqueous and gas phased cyclic voltammograms [22].

Anodic polarization of nickel in neutral and alkaline aqueous solutions has been reported to produce α-, β- and γ-NiO with an oxidation state of Ni^{2+} as well as a nickel oxide hydroxide species (NiOOH) with oxidation state Ni^{3+} at high electrical potentials. For nickel nanoparticles in 1M KOH, Figure 4.1 shows a typical cyclic voltammogram which can be divided into 6 regions.

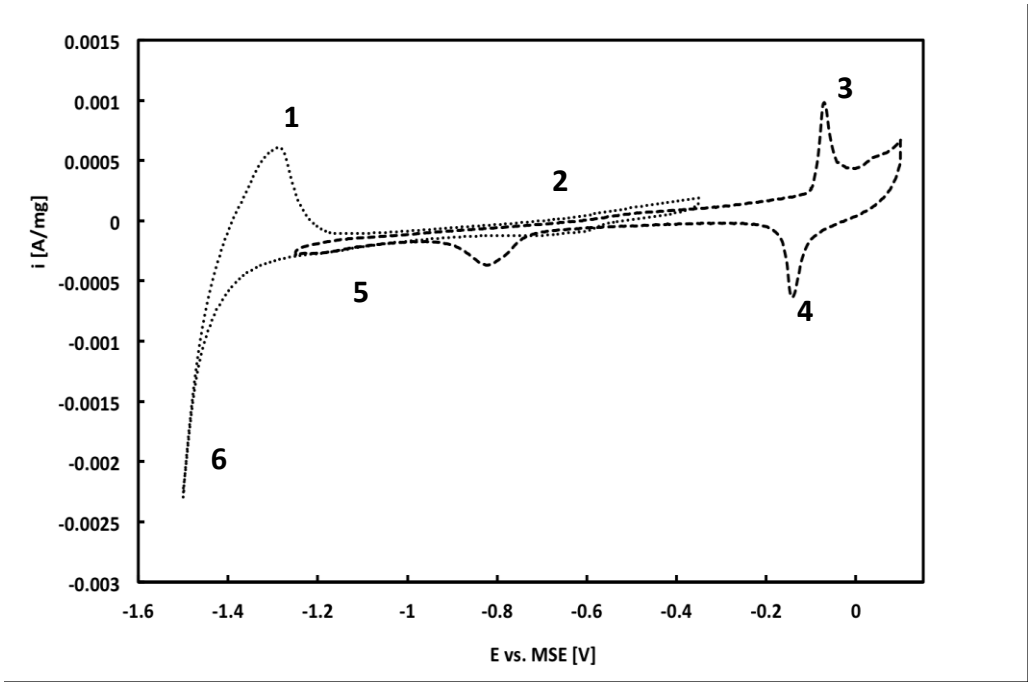

Figure 4.1 Cyclic voltammogram of nickel nanoparticles in 1M KOH [18]

At negative potentials, described by region 6, hydrogen evolution occurs at the electrode which is in the nickel metal state. Subsequent increase in the electrical potential results in the formation of α-$Ni(OH)_2$ which corresponds to peak 1 and is expressed by equation (4.2)

$$Ni + 2OH^- \rightarrow \alpha Ni(OH)_2 + 2e^- \quad (4.2)$$

The $\alpha Ni(OH)_2$ undergoes a change to $\beta Ni(OH)_2$, which does not appear as a peak since it represents a morphological rather than electrochemical change in the electrode [23]. The $Ni(OH)_2$ is further oxidized to nickel oxide hydroxide, NiOOH, according to equation (4.3).

$$\beta Ni(OH)_2 + OH^- \rightarrow (\beta, \gamma)NiOOH + H_2O + e^- \quad (4.3)$$

This transformation from Ni^{2+} to Ni^{3+} appears as peak 3 on the cyclic voltammogram. In decreasing the electrical potential, $(\beta, \gamma)NiOOH$ is reduced to β-$Ni(OH)_2$ in the reverse

reaction of (4.3). Partial reduction of the β Ni(OH) and α Ni(OH) electrode to nickel metal according to equation (4.4).

$$(\alpha, \beta)\mathrm{NiOOH} + \mathrm{H_2O} + \mathrm{e^-} \rightarrow \mathrm{Ni} + 2\mathrm{OH^-} \qquad (4.4)$$

4.2 *In-situ* Resistance Measurements During Deposition

YSZ pellets were prepared according to Chapter 3. Parallel gold electrodes, shown in Figure 4.2, were painted onto the top of the pellet with gold paste (Gwent) using an electrical tape mask. Short (1 cm) gold wires (Alfa Aesar, 99.9% metal basis, ø= 0.3 mm) were subsequently connected to the electrodes and anchored to the pellet with ceramic paste (Aremco, Ultra-Temp 516). The assembly was placed in the oven at 550°C for 1 hour to cure the paste and ceramic. Clear cyanoacrylate glue (Superglue) was used to further cement the gold wires to the pellet, ensuring electrical connections were not dislodged during handling or deposition.

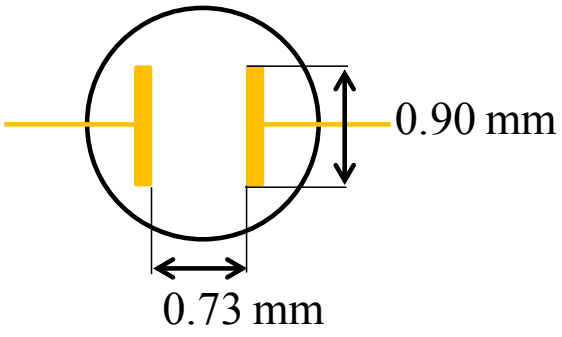

Figure 4.2 Electrode configuration for *in situ* resistance measurements

Pellet placed on an electronically insulated rubber disc (1 mm x 20 mm) and installed into the evaporator with teflon tape. A square rubber mask was placed over the pellet and alligator clips secured to the gold wires. Electronic connections were verified and passed out of the vaccum chamber through conductive pins which had been electronically isolated from the evaporator's metal frame. Resistance measurements were recorded with a multimeter

(NetxxTech Digital Multimeter 2218202) and film thickness monitored with a quartz microbalance thin film monitor (Edwards FTM-5). Measurements were recorded for a deposition rate of 0.5 nm s^{-1} at a pressure of $4.2x10^{-5}$ mBar and are shown in Figure 4.3

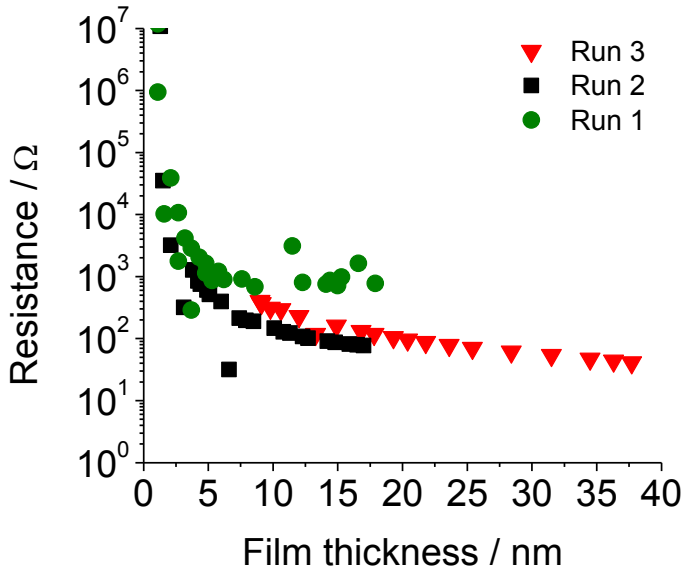

Figure 4.3 *In-situ* resistance measurements for nickel during deposition, rate = 0.5 nm.s^{-1}

This data was fit to the model given in equation (2.56) and the critical thickness was found to be 3.0 ± 0.4 nm. Below this value thickness, the film exists as an array of disconnected islands, while films above this threshold are electronically percolated. As a result, film thickness of 50 nm and 100 nm were selected for further study.

4.3 Experimental

Yttria stabilized zirconia pellets were synthesized as outlined in Chapter 3. Copper films were synthesized using evaporative physical vapor deposition with resistive heating of tungsten dimble boats (Kurt J. Lesker) at 2.5 x 10^{-5} mBar in a BOC Auto306. Metal slugs (99.99% metal basis, Alpha Aesar) were heated until a deposition rate of 0.5nm s^{-1} was achieved as measured

in-situ with a quartz microbalance thin film monitor (Edwards, FTM-5). Films of 20, 50 and 100 nm were deposited with a geometric surface area of 2.5 cm^2 using a circular mask. Concurrently deposits of copper on silicon wafer were used to confirm film thickness. Counter (geometric area ≈ 2.46 cm^2) and pseudo-reference (geometric area ≈ 0.2 cm^2) electrodes were painted onto the reverse according to the bipolar configuration shown in Figure 4.4 [24–26]

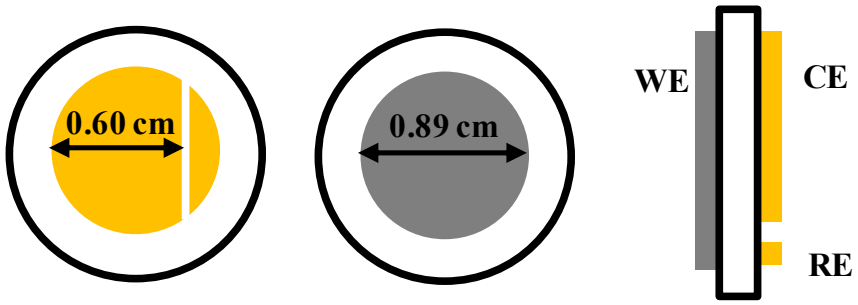

Figure 4.4 Electrode configuration of thin film electrochemical cell (WE: Nickel)

Gold wires were connected to the electrodes with gold paste (Gwent). These wires were anchored with high temperature ceramic paste (Aremco, Ultra-Temp 516) onto uncoated segments of the pellet. The cement and gold paste were cured at 550°C for 1 hour in air. Before the experiment Au/YSZ was treated at 550°C in air. Studies of the effect of this pre-treatment can be found in Chapter 4. The resulting cell was placed in a 200 mL CSTR reactor made of Pyrex and connected as shown in Figure 4.5.

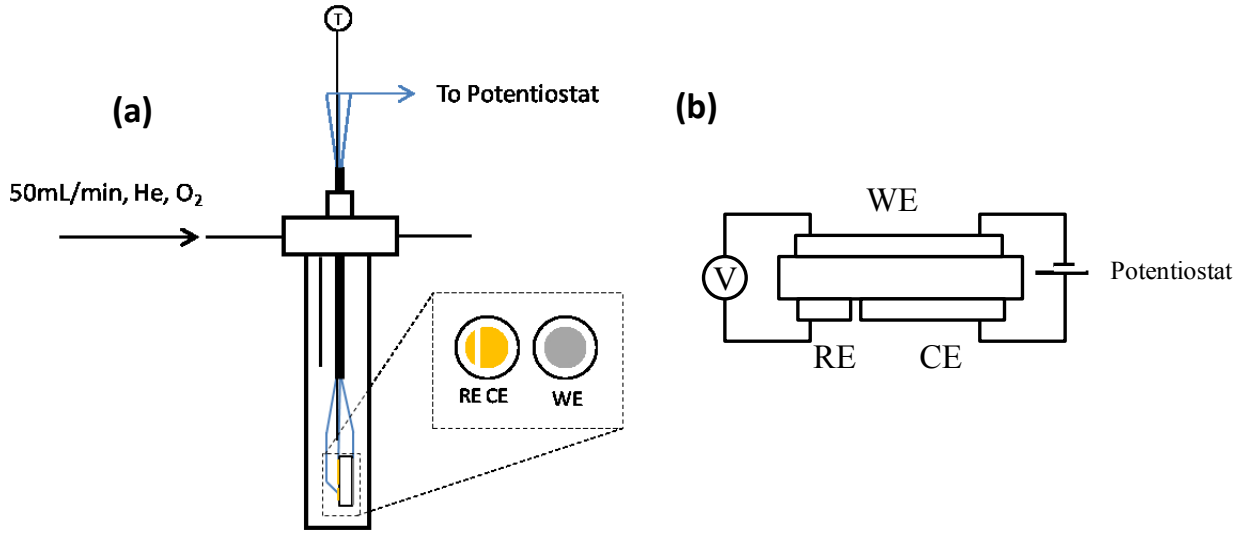

Figure 4.5 Reactor setup (a) CSRT with pellet configuration and (b) electronic connections to electrochemical cell.

Helium (99.997%, Linde) and Oxygen (99.997%, Linde) were mixed with MKS 1359C mass flow controllers until a total flow of 50 mL.min^{-1} was achieved. Oxygen partial pressures of 0-20 kPa were used. The cells were placed under a 50 mL.min^{-1} flow of helium to limit the formation of chemical oxides. Cyclic voltammetry measurements were carried out with PARSTAT 2263 potentiostat with PowerSuite software package (Princeton Applied Research).

4.4 Results and Discussion

4.4.1 Nickel Film Electrode of 50 nm Thickness

Figure 4.6 shows a typical cyclic voltammogram of a 50 nm nickel film on YSZ. The results shown in this section are for the stable third cycles unless otherwise indicated. In cathodic sweep, a single peak is observed at -0.15 V. At the start of the scan, the film is positively polarized and, oxygen evolution and oxide formation both occur at the three phase boundary (tpb) between nickel electrode, YSZ and gas phase, given by equation (2.28) and (2.29),

respectively. The maximum number of moles produced by this electrochemical process is given by Faraday's law, given by equation (4.5).

$$n = \frac{QM}{Fz} \tag{4.5}$$

Where Q is the charge associated with the process (current x time), M the molar mass of the species being formed, F faraday's constant (96485 C/mol e^-) and z the number of electrons exchanged in the electrochemical reaction. For the oxidation of O^{2-} in YSZ, z equals 2. As the film is polarized with more negative potentials, it undergoes electrochemical reduction to metallic nickel with charge Q_{RED}. The charge is calculated from integral of the peak with respect to time, given the baseline shown in Figure 4.6. From this the total number of moles of nickel reduced can be calculated using Faraday's law.

The actual number of moles is determined by the current efficiency, which is given by the ratio of total charge, Q_{TOT}, divided by the charge of the given process, as given by equation (4.6).

$$\eta_i = \frac{Q_i}{Q_{TOT}} \times 100 \tag{4.6}$$

Where *i* represents the oxygen evolution (O_2) or oxide reduction (RED) reactions.

Sweeping towards positive potentials, the film re-oxidizes from the backspillover of O^{2-}. As shown by Vayenas *et al.* [27] and Souentie *et al.* [9] this peak is not visible for films which form stable chemical oxides under operating conditions as the film is chemically oxidized before electrochemical oxidation of possible. As shown in Figure 4.6, even at low partial pressures, only one cathodic peak is visible. In addition, the film is shown to be sensitive to partial pressure as, at P_{O2}= 20 kPa, the cathodic peak is suppressed. The presence of chemical oxides are further reflected in the shape of the scan: the observed slant of the scan is associated with high ohmic resistances in the film either due to the oxides or the thickness of the film.

In increasing the initial positive potential of the scan, as shown in Figure 4.7 resulting either from very thin films or oxidation, there is an increase in the reduction current. This is caused by the formation of more oxides at higher initial currents and a shift in the peak to more negative values is consistent with a more difficult reduction associated with thicker oxide films. This sensitivity to positive polarization potential confirms that the process anodic process can be electrochemically controlled.

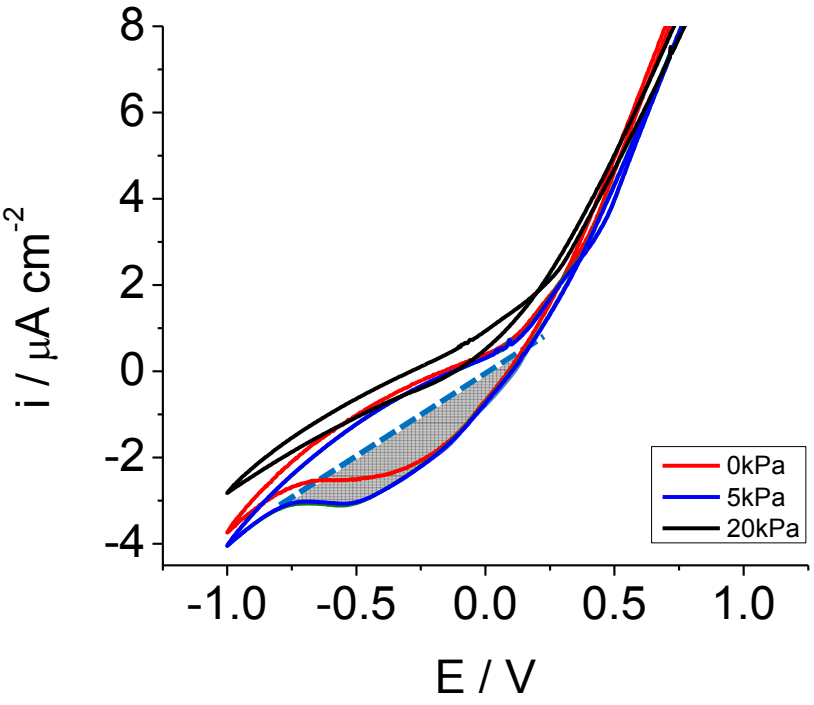

Figure 4.6 Effect of partial pressure of oxygen on the cyclic voltammogram of 50 nm Ni film on YSZ at T=350 °C, ν =20 mV.s^{-1}, E_i = 0.4 V, E_s=-1 V. Peak area of 5 kPa highlighted.

A similar trend is observed with increasing the hold time at a constant positive potential, shown in Figure 4.8 for E_i = 400 mV. With increasing hold time, there is an increase in peak current, broadening of the reduction peak and shift to more negative potentials as shown in Figure 4.8.

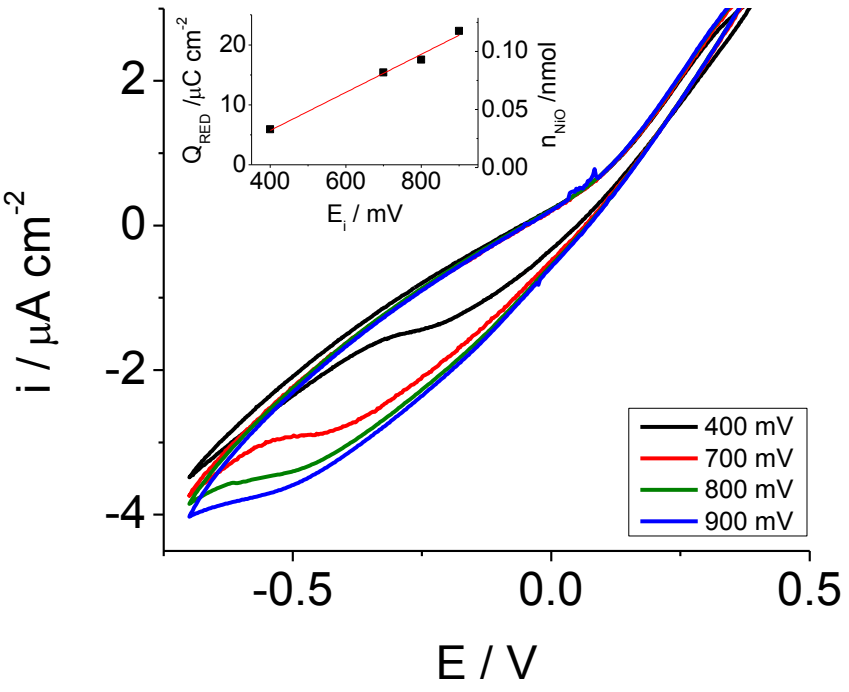

Figure 4.7 Effect of positive potential on the cyclic voltammogram of 50 nm Ni film on YSZ at T = 350 °C, v = 20 mV.s^{-1}, P_{O2} = 20 kPa, E_s = -1 V

The current efficiency of the NiO formation can be calculated from the charge of the reduction peak and oxygen evolution reactions can be calculated from equations (4.7) and (4.8) is shown in the insert of Figure 4.8a.

$$\eta_{NiO} = \frac{Q_{RED}}{Q_{TOT}} \times 100 \tag{4.7}$$

$$\eta_{O_2} = 100 - \eta_{NiO} \tag{4.8}$$

Where Q_{RED} is the charge of the reduction peak and Q_{TOT} the anodic charge associated with a hold time of t_H at 400mV as calculated with equations (4.9) and (4.10), respectively.

$$Q_{TOT} = i_{t=0} t_H \tag{4.9}$$

$$Q_{RED} = \frac{\sum(i \ \Delta E)}{\upsilon} \qquad (4.10)$$

The increase in hold time results in a logarithmic increase in oxide formation as shown in Figure 4.8b. This is consistent with the Mott and Cabrera oxidation model for thin oxide films.

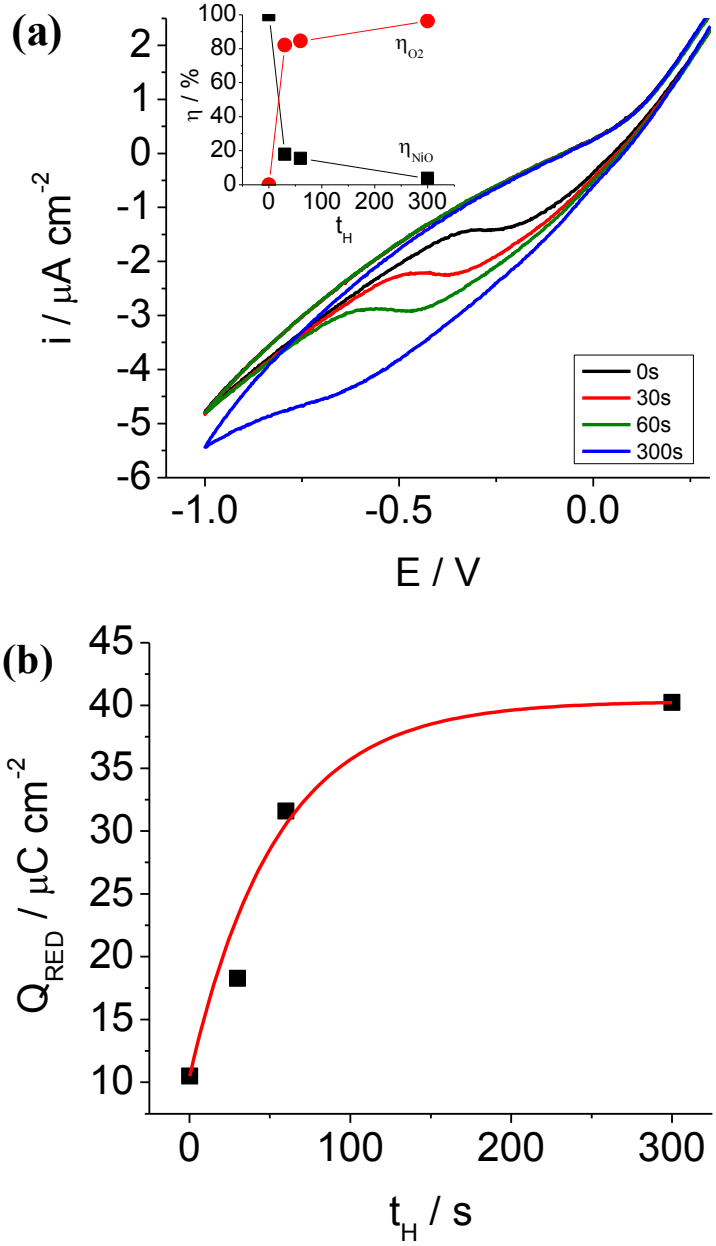

Figure 4.8 Effect of hold time on first cycle of 50 nm Ni films on YSZ at T = 350 °C, ν= 20 mV.s^{-1}, P_{O2} = 20 kPa, E_i = 0.4 V, E_s = 1.0 V (a) cyclic voltammogram, first cycle and (b) total charge of cathodic peak

The current efficiencies of oxide formation decreases with increased hold times as the oxides formed passivates the surface, inhibiting the formation of subsequent oxides and showing a favorability to the evolution of oxides.

4.4.2 Effect of Film Thickness: 50 nm vs 100 nm Nickel Film Electrodes

The effect of film thickness is shown in Figure 4.9. At a film thickness of 100 nm, the current is lower than in the 50 nm film. This is due to the decrease in three phase boundary resulting from a more compact and continuous film of the 100 nm film as compared with the 50 nm.

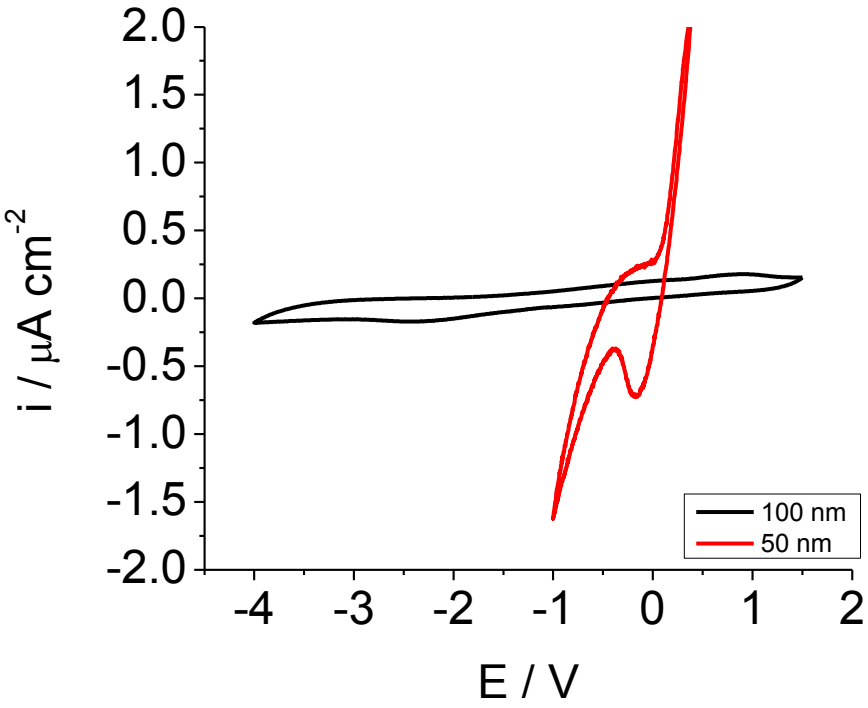

Figure 4.9 Effect of film thickness, T = 350°C, P_{O2} = 0 kPa, ν = 20 mV.s^{-1},

The scan window of the 50 nm film (400 mV to -1000 mV) is smaller than that of the 100 nm film (1.5 to -4) since in the thinner film the onset of oxygen evolution and oxygen uptake occurs at lower potentials and obscures other electrochemical processes on the electrode. In

addition to this, it is important to note that the electrical potentials are applied to the film with respect to the pseudo-reference reaction (equation (2.31)) which occurs at the gold electrode. The result is a reference state which is sensitive to partial pressure, but also to the porosity and geometry of the gold electrode.

4.4.3 Nickel Film Electrode of 100 nm Thickness

Figure 4.10 shows typical cyclic voltammogram of a 100 nm nickel film on YSZ. Two cathodic ($E_{p,1c}$ =-2.3 V and $E_{p,2c}$ =- 4 V) and two anodic peaks ($E_{p,1A}$= -0.05 V and $E_{p,2A}$ =0.5 V) are observed. These are associated with the oxidation and reduction at different locations along the film. At 1.5 V, the formation of oxides proceeds along the three phase boundary as discussed by Souentie *et al.* [9] and spreads along the two phase boundary between film and YSZ. At 100 nm, the film is much thinner and than that studied by Souentie *et al.* [9] resulting in a greater percolated structure and thus more three phase boundary sites, which might explain the absence of this peak in the literature.

The effect of partial pressure in Figure 4.10, shows that the cathodic peak is sensitive to only the absence of oxygen and at any concentration remains constant. The same is not true of the anodic peaks; there is a two-fold increase in the charge of peak 2A with decreased partial pressure from 20 kPa and 0 kPa. The sensitivity of this peak to partial pressure of oxygen indicates that the location of the oxide formed is exposed to the reaction gases, and thus exists at the three phase boundary. Additionally, because this peak appears at higher potential, this indicates that the formation of oxides along the two phase boundary between electrode and electrolyte forms first and then extends along the exposed surface of the metal. This trend is not observed at T = 400 °C.

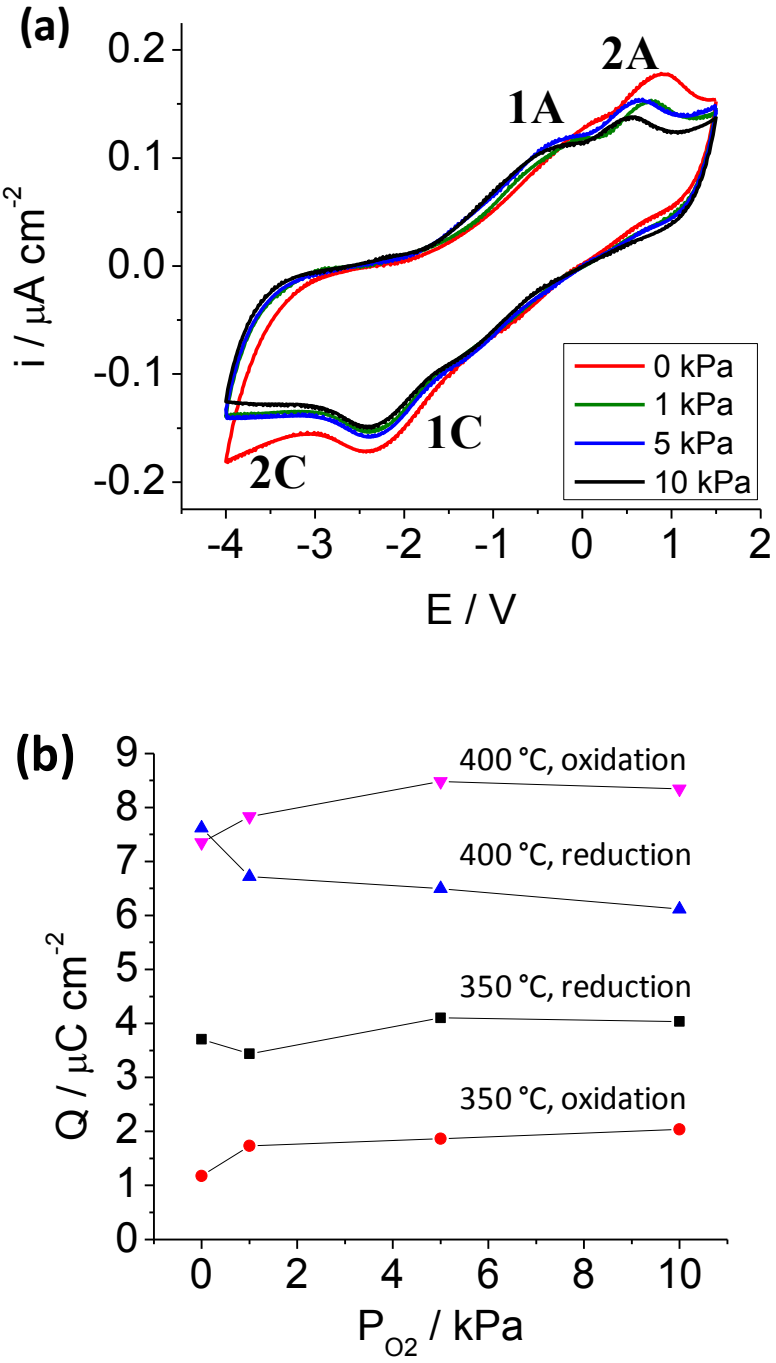

Figure 4.10 Effect of partial pressure on the cyclic volatmmogram of 100 nm nickel film on YSZ, T = 350°C, v = 20 mV.s^{-1}, E_i = 1.5 V, E_s = -4 V (a) cyclic voltammogram, third cycle and (b) change in charge with partial pressure for reduction processes (peaks 1C and 2C) and oxidation processes (peaks 1A and 2A)

Further information regarding the kinetics of the oxidation processes can be obtained through variation in the scan rate Figure 4.11 shows that with increased scan rate, larger peak currents are observed. The peak current is proportional to $\nu^{0.5}$, which is representative of a diffusion limited process as given by the Randles-Sevcic equation.

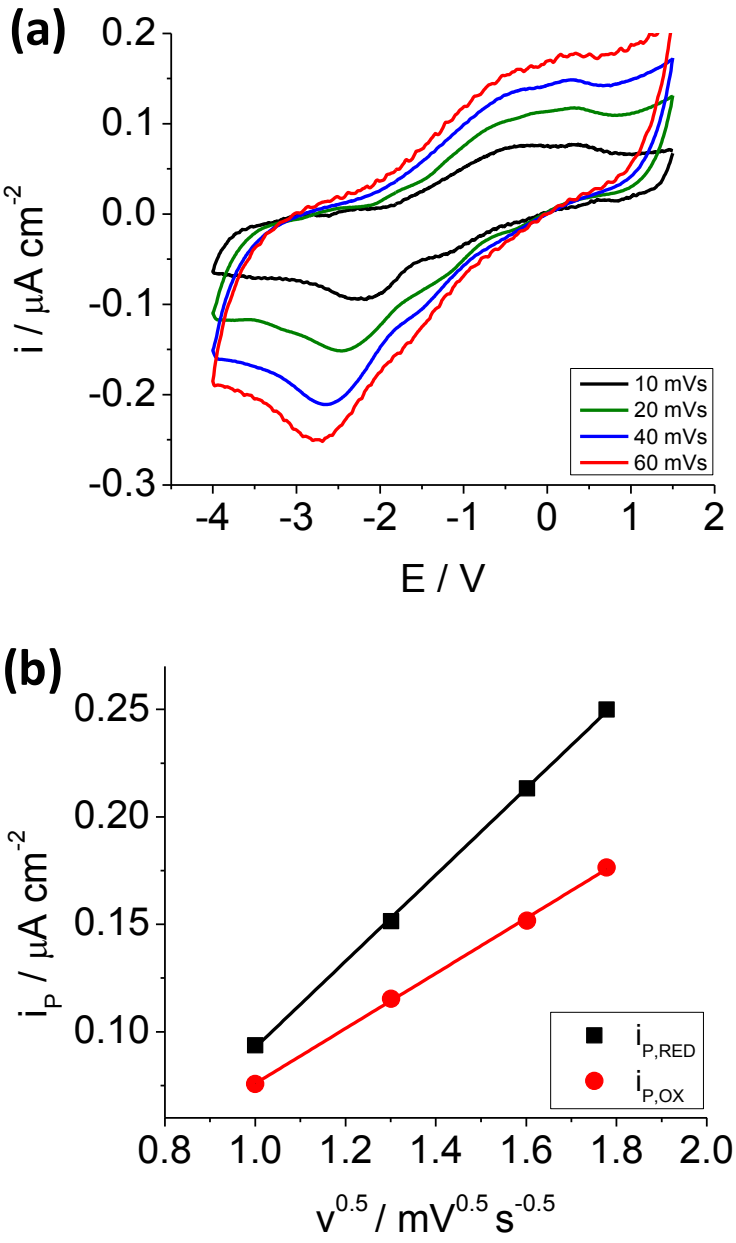

Figure 4.11 Effect of scan rate on the cyclic voltammagram of 100 nm Ni film on YSZ at T = 350 °C, P_{O2} = 20 kPa (a) cyclic voltammagram, third cycle and (b) peak current of primary cathodic (peak 1C) and anodic (peak 2A) processes.

With increased hold time in 100 nm nickel films, the current of the reduction peak undergoes growth that follows neither parabolic nor logarithmic trend, as shown in Figure 4.12.

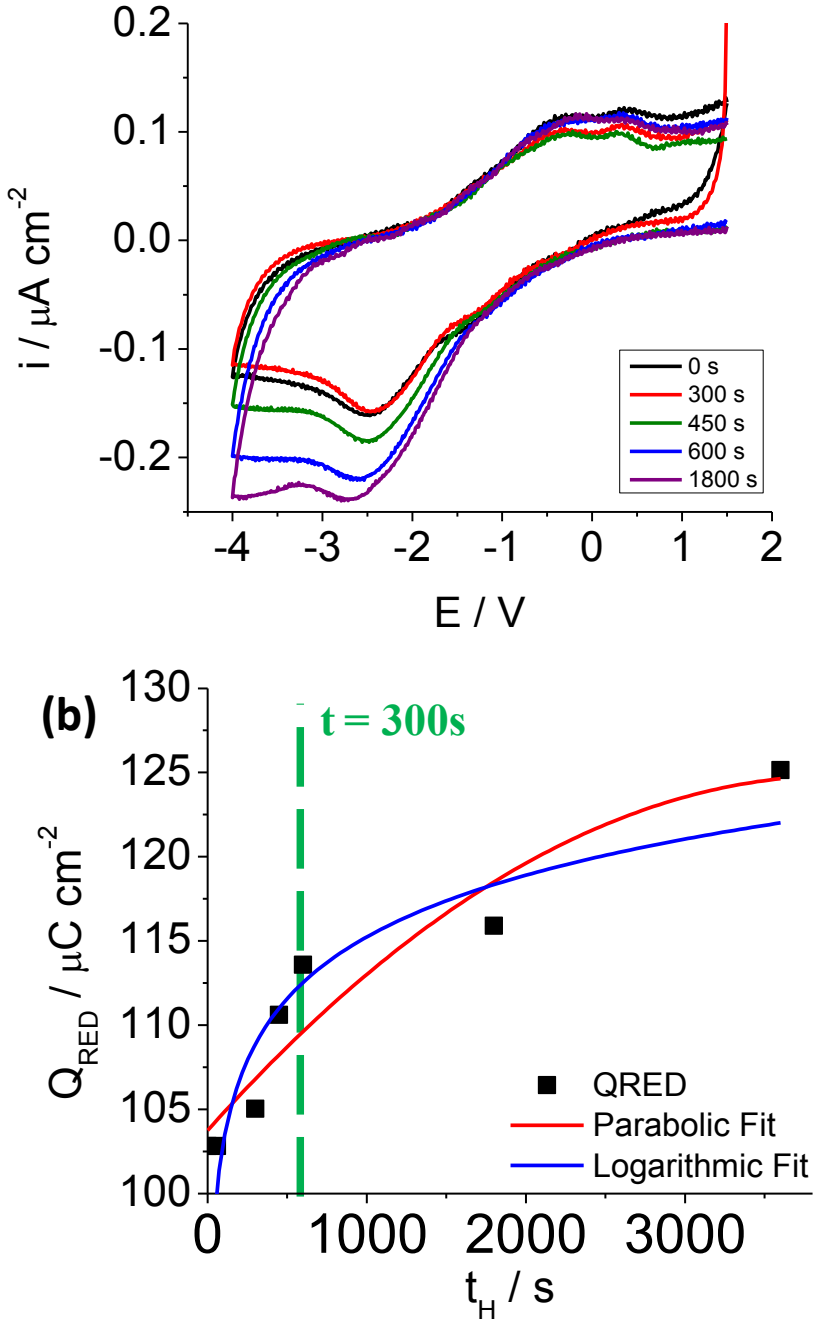

Figure 4.12 Effect of hold time on the cyclic voltammogram of 100 nm nickel film on YSZ (a) cyclic voltammogram, first cycle and (b) Charge of charge for reduction process (peaks 1C and 2C)

The trend appears to proceed through two stages. At hold times below 300 s, there is an parbolic increase in oxide formation. Once saturated, above 600 s, there is the appearance of a second cathodic peak and a decrease in the rate of formation of oxides as the second peak is not fully measured in the scan due to restrictions in the application of large negative potentials which partial reduction of the YSZ [28, 29].

4.5 **Proposed Model**

This proposed mechanism expands upon that suggested by Sounetie *et al.*. to include behavior of thin films of 100 and 50 nm. Due to the Volmer-Weber mechanism of film formation for nickel on YSZ, thinner films form percolated networks with high three phase boundary, but lower two phase boundary as more of the YSZ is exposed. As a result the oxide formation at the three phase boundary is more significant in thin films than in compact, continuous films. This is supported by the presence of a single cathodic peak which is sensitive to the partial pressure of oxygen observed in the 50 nm film. Furthermore, the thin film oxide forms according to a logarithmic rate expression which is consistent with Mott and Cabrera oxidation models for thin films. With the increased formation of anodic oxides, the current efficiency for the formation of subsequent oxides decreases and the oxygen evolution reaction is preferred.

At a film thickness of 100 nm higher film thicknesses, the three phase boundary contribution decreases and the appearance of two cathodic and anodic peaks represent the formation of nickel oxides in two phase boundary. This oxide forms first along the two phase boundary and then extends to the outer surface of the electrode via the three phase boundary. With increased anodic hold times, the rate of oxide formation is neither parabolic nor logarithmic, but seems to follow a two-step rate expression which changes after 300 s of polarization.

4.6 **Conclusion**

Cyclic voltammetry has been used to elucidate the mechanism of oxide formation in thin films for use in electrochemical formation. Electrochemical oxides form in two locations, along the three phase boundary and exposed outer electrode surface, and at the two phase boundary. In thinner films, three phase boundary contributions are more significant than two phase boundary contributions, and so only one cathodic peak is observed. These oxides form according to a logarithmic rate expressions, which is consistent with Mott and Cabrera's model for thin oxide films.

At higher film thicknesses both three phase boundary and two phase boundary oxide formation is measured and formation proceeds first along the three phase boundary and then extending along the gas exposed surface via the three phase boundary. These oxides form according to a parabolic rate expression which is consistent with Wagner's theory of oxidation, which is consistent with Conminellis findings for nickel films of 880 nm.

4.7 **References**

[1] P. Fouilloux, *Appl. Catal*, 8, 1–42, (1983).

[2] J. R. Rostrup-Nielsen, *J. Catal.*, 199, 173–199, (1973).

[3] W. Wei, G. Jinlong, *Frontiers of Chemical Science and Engineering*, 5, 2–10, (2010).

[4] W. M. Haynes, ed., *CRC Handbook of Chemistry and Physics*,
93rd Edition (CRC Press/Taylor and Francis , Internet Version 2013)

[5] A. Cantos-Gómez, R. Ruiz-Bustos, J. van Duijn, *Fuel Cells*, 11, 140–143, (2011).

[6] F. Tietz, P. Nikolopoulos, *Fuel Cells*, 9, 867–872, (2009).

[7] W. Zhu, S. Deevi, *Mater. Sci. Eng., A*, 362, 228–239, (2003).

[8] V. Jiménez, C. Jiménez-Borja, P. Sánchez, A. Romero, E. I. Papaioannou, D. Theleritis, S. Souentie, S. Brosda, J. L. Valverde, *Appl. Catal. B.*, 107, 210–220, (2011).

[9] S. Souentie, C. Falgairette, C. Comninellis, *J. Electrochem. Soc.*, 157, P49, (2010).

[10] N. Birks, G. Meier, *Introduction to High Temperature Oxidation of Metals* (Edward Arnold, 1983), p. 198.

[11] G. Wood, I. Wright, J. Ferguson, *Corros. Sci.*, 5, 645–661, (1965).

[12] J.-C. Rocaries, M. Rigaud, 5, 59–62, (1971).

[13] W. J. Moore, J. K. Lee, *Trans. Faraday Soc.*, 48, 916, (1952).

[14] K. Hauffe, L. Pethe, R. Schmidt, S. R. Morrison, *J. Electrochem. Soc.*, 115, 456, (1968).

[15] M. J. Graham, M. Cohen, *J. Electrochem. Soc.*, 119, 879, (1972).

[16] H. B. Su, J. L. Cerne, F. C. Crnkovic, S. A. S. Machado, L. A. Avaca, Ä. Carlos, U. De Sa, Ä. Paulo, *Int. J. Hydrogen Energy*, 25, 415–423, (2000).

[17] S. A. S. Machado, L. A. Avaca, *Electrochim. Acta*, 39, 1385–1391, (1994).

[18] E. A. Baranova, A. Cally, A. Allagui, S. Ntais, R. Wuthrich, *Comptes Rendue Chimie*, (2012).

[19] I. J. Brown, S. Sotiropoulos, *J. Appl. Electrochem*., 10, 107–111, (2000).

[20] H. Vaidyanathan, K. Robbins, G. M. Rao, *J. of power sources*, 63, 7–13, (1996).

[21] W. G. Tam, J. S. Wainright, *J. Power Sources*, 165, 481–488, (2007).

[22] A. Jaccoud, G. Foti, C. Comninellis, *Electrochim. Acta*, 51, 1264–1273, (2006).

[23] N. Ii, H. Bode, K. D. J. Witte, *Electrochim. Acta*, 11, 1079–1087, (1966).

[24] F. Dorado, A. De Lucas-Consuegra, C. Jiménez, J. L. Valverde, *Appl. Catal. A*, 321, 86–92, (2007).

[25] F. Dorado, A. De Lucas-Consuegra, P. Vernoux, J. L. Valverde, *Appl. Catal. B.*, 73, 42–50, (2007).

[26] A. De Lucas-Consuegra, F. Dorado, C. Jiménez-Borja, A. Caravaca, P. Vernoux, J. L. Valverde, *Catal. Today*, 146, 293–298, (2009).

[27] C. G. Vayenas, A. Ioannides, S. Bebelis, *J. Catal.*, 129, 67–87, (1991).

[28] J. Janek, C. Korte, *Solid State Ionics*, 116, 181–195, (1999).

[29] R. E. W. Casselton, *J. Appl. Electrochem.*, 4, 25–48, (1974).

Chapter 5 Copper Thin Films Interfaced with Yttria-Stabilized Zirconia

The percolation threshold of copper on YSZ was determined to be 5.0±1.0 nm, and so thin films of 50 and 100 nm were synthesized to determine the effect of polarization using cyclic voltammetry. Electrochemical investigation of copper thin films interfaced with YSZ reveals the electrodes to be significantly affected by ohmic losses resulting from oxidation to Cu_2O, resulting in distortion of the cyclic voltammograms for 50 nm copper films. At 100 nm, two oxide states, Cu_2O and CuO are formed with positive polarization, being subsequently reduced to Cu with negative potentials. Oxides form at the three phase boundary and kinetics follow a logarithmic rate expression.

5.1 Introduction

Supported copper catalysts have various industrial application including hydrogenation reactions [1], such as methanol synthesis, low temperature water-gas shift (WGS) and selective hydrogenation of various organic compounds [2]. Copper oxide is also found to be very effective for the reverse water gas shift (RWGS) reaction for the selective formation of CO [3]. Due to its poor activity towards hydrogenolysis reactions, copper is resistant to coking, but is prone to sintering at elevated temperatures, being the least stable of transition metal catalysts after silver [1].

Copper oxide deposited on yttria stabilized zirconia via wet impregnation with copper nictrate has been used as a catalyst in CO oxidation and selective catalytic reduction of NOx [4]. The use of zirconia as a support for copper has been shown to increases long-term stability as

well as enhance selectivity and activity. This is attributed to the metal support interactions, which result in the formation of highly mobile oxygen vacancies on the surface of the support [4]. Ekerdt and coworkers confirmed these vacancies to be the active site for the CO hydrogenation reaction and found that greater reaction rates can be attributed to greater mobility of vacancies [5, 6].

Due its resistance to catalytic coking, copper cermets are studied as an anode material for direct hydrocarbon solid oxide fuel cells to replace nickel-based catalysts. Copper has poor activity for the oxidation of hydrocarbons and is thought to act solely as an electronic conductor. Copper-YSZ cermets perform poorly, but the addition of molybdena in the anode result in increased activity and an increase in selectivity towards the partial oxidation of the fuel [7, 8]. Copper - Ceria (CeO_2) -YSZ cermets are also highly active, but less selective. [9]

Electrochemical promotion of copper thin films was attempted for the hydrogenation of CO_2 and was found unsuccessful due to the high electronic resistance of copper oxide [10]. The addition of an intermediate TiO_2 film improved the polarization of the copper resulting in a rate enhancement ratio of 2.4[10].

Due to the catalytic activity for a variety of gas phased reactions, interaction effects observed on ionically conducting materials (TiO_2, YSZ, CeO_2) and high electronic conductivity, copper presents a promising material for electrochemical promotion.

5.1.1 Oxidation of Copper

The thermal and anodic oxidation behaviors of copper thin films are of interest for copper interconnect in microelectronics as well as solid oxide fuel cells [6]. At temperatures above 270°C, thermal oxidation of copper results in CuO formed through diffusion limited process

according to Wagner's law [11]. The rate of formation follows a parabolic expression given by equation (2.47). Figure 5.1 shows the effect of temperature on the parabolic rate constant.

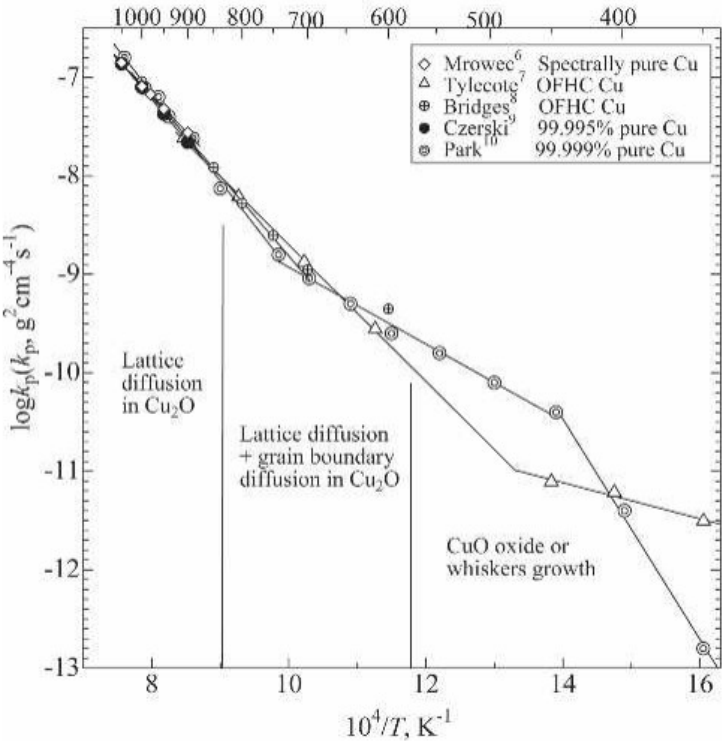

Figure 5.1 Effect of temperature on the parabolic oxidation constant of copper [12]

The formation of copper oxide is driven by the concentration gradient of copper ions in the metal and oxide-oxygen surface and the rate of oxidation increases until a thick enough scale is formed that the diffusion of copper cations is prohibitive to further growth.

5.1.2 Cyclic Voltammetry of Copper Electrodes

Aqueous Cyclic Voltammetry

Few solid state studies of copper electrodes have been attempted. The reduction and oxidation behavior of copper electrodes in aqueous alkaline solution are complexe and involve the formation of several oxidation stated. Cyclic voltammetry studies performed by Haleem *et al.*

[13] on polished polycrystalline copper rod show four distinct peak pairs associated with the formation and reduction of Cu_2O, CuO, Cu_2O_3 and CuO_2^{2-} , a soluble copper species. A characteristic CV for copper in 0.1 M NaOH with platinum counter electrode and saturated calomel reference electrode (SCE) is shown in Figure 5.2.

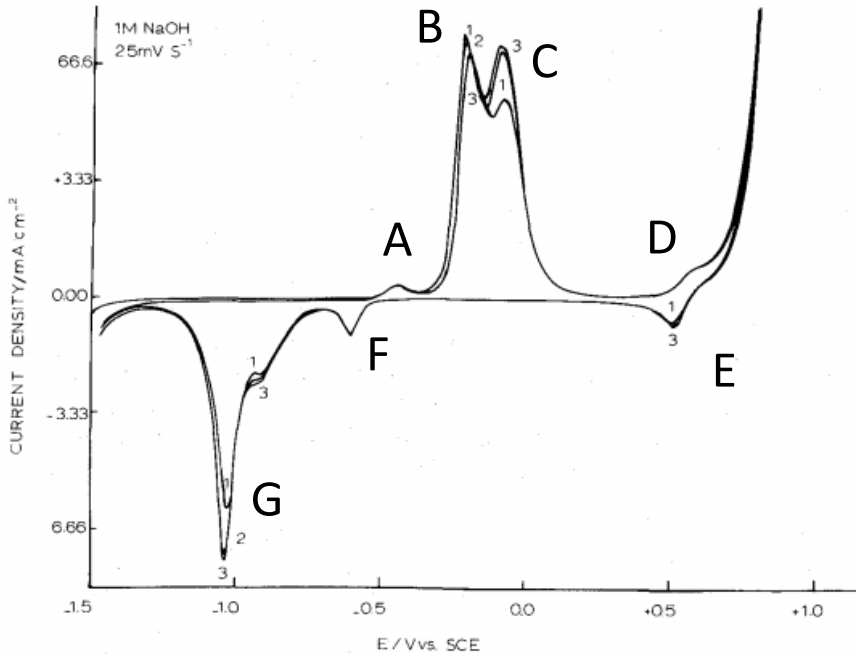

Figure 5.2 Cyclic voltammogram of copper in 1M NaOH solutions at 25 $mV.s^{-1}$ [13]

At low electrical potential, the copper exists as Cu^0. Peak A is attributed to a one-electron transfer process which was assumed to be the formation of Cu(OH) on the surface of the electrode, given by equation (5.1). An equilibrium exists between Cu(OH) and Cu_2O and water according to equation (5.2)

$$Cu + OH - \ CuOH + e^- \tag{5.1}$$

$$2\ Cu(OH) \rightleftharpoons Cu_2O + H_2O \tag{5.2}$$

The charge of the peak was representative of a monolayer of Cu_2O at 0.1 M NaOH and was shown to be electrochemically paired with peak F.

Peak B was found to represent a two electron transfer reaction, which was assumed to be the formation of $Cu(OH)_2$ which exists in equilibrium with CuO as shown in equations (5.3)-(5.5).

$$Cu + 2OH^- \rightleftharpoons Cu(OH)_2 + 2e^- \quad (5.3)$$

$$Cu(OH) + OH^- \rightleftharpoons Cu(OH)_2 + e^- \quad (5.4)$$

$$Cu(OH)_2 \rightleftharpoons CuO + H_2O \quad (5.5)$$

Peak C is the formation of a soluble cuprite, species, CuO_2^{2-}, from base copper or $Cu(OH)_2$ present on the electrode surface.

The majority of the CuO is formed directly from Cu rather than Cu_2O as the peak B has greater area than that of A. This process is electrochemically paired with peak G. Peak D is the oxidation of CuO to Cu_2O_3 which occurs only with high polarization potential.

Solid Electrolyte Cyclic Voltammetry

Van Manen *et al.* [14] carried out cyclic voltametry of copper/copper oxide working electrodes on 14 mol% Y_2O_3–ZrO_2 pellets at 700-900°C. Electrodes were formed from slices of copper/copper oxide rods made from powders pressed at 450 MPa and sintered at 1000°C for 10 h [14]. Figure 5.3 is a representative cyclic voltammogram of the copper/copper oxide oxidation and reduction behaviors at 700°C in Argon. Nickel/nickel oxide electrode prepared in a similar method was used as a pseudo-reference electrode since the charge transfer reaction on nickel was believed to be reversible.

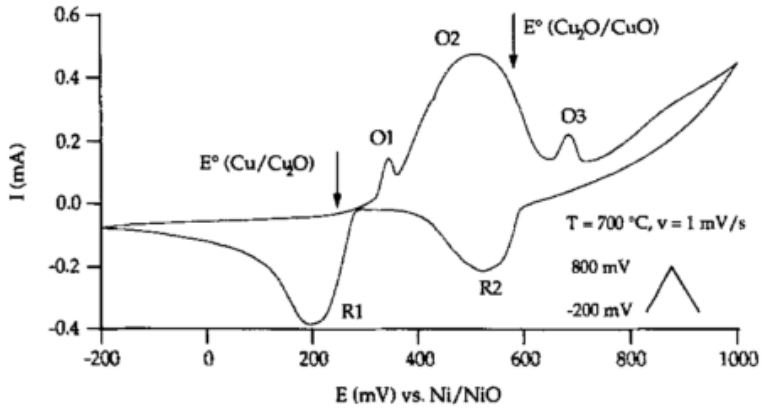

Figure 5.3 Cyclic voltammetry of rod on 14 mol % YSZ with Ni/NiO reference electrode under argon environment, T= 700°C, ν = 1 mV.s^{-1}[14]

Two cathodic peaks and three anodic peaks were observed at low scan rates. Peaks O2 and R1 are paired electrochemical processes given by the overall reaction shown in equation (5.6)

$$2\,Cu + \frac{1}{2}O_2 \rightleftharpoons Cu_2O \tag{5.6}$$

Peak O1 was not attributed to a paired reduction process peak, but was found to be equivalent to the formation of a 1nm scale on the electrode. Processes O3 and R2 were associated to the formation and reduction of CuO, respectively, as given by equation (5.7)

$$2Cu_2O + \frac{1}{2}O_2 \rightleftharpoons 2CuO \tag{5.7}$$

In varying the scan rate, the peak current both oxidation peaks were not found to be linearly proportional to the square of the scan rate. Standard potentials for both reactions were calculated from thermodynamic data and are labeled on Figure 5.3.

5.2 **Experimental**

Yttria stabilized zirconia discs were synthesized and prepared as described Chapter 1. Copper films were synthesized using evaporative physical vapor deposition with resistive

heating of tungsten dimble boats (Kurt J. Lesker) at 2.5E-5 mBar in a BOC Auto306. Metal slugs (99.99% metal basis, Alpha Aesar) were heated until a deposition rate of 0.5 nm.s^{-1} was achieved as measured *in-situ* with a quartz microbalance thin film monitor (Edwards, FTM-5). Films of 50, 100 nm were deposited with a geometric surface area of 2.5 cm^2 using a circular mask as outlined in Section 4.3.

5.3 Characterization of Copper Interfaced with YSZ

5.3.1 Critical Thickness

A measure of the critical thickness of copper thin films was determined using the in-situ resistance measurement method described in Chapter 4.2. Measurements were taken during copper deposition at a rate of 0.5 nm.s^{-1} and a pressure of 3.0x10^{-5} mBar.

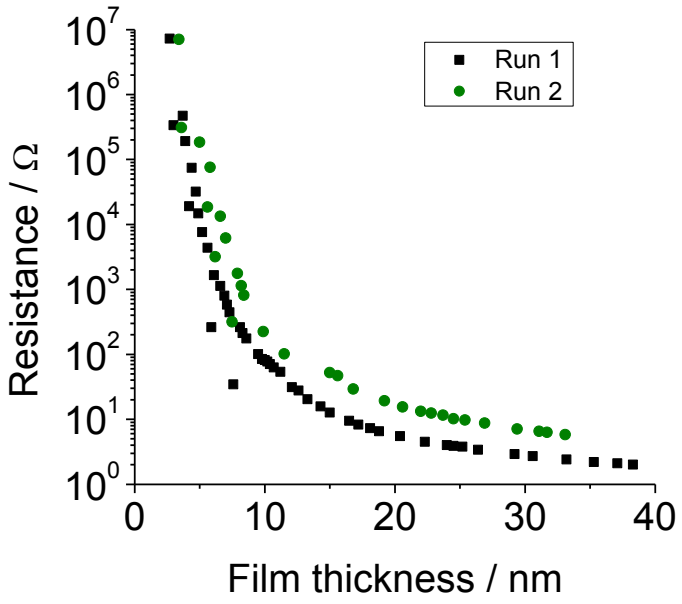

Figure 5.4 In situ resistance for copper deposition at a rate of 0.5 nm.s^{-1}

Fitting this curve to the relation given by equation (2.56) yields a critical thickness of 5.0 $\pm$1.0 nm.

5.3.2 Scanning Electron Miscroscopy of Cu Thin Films

Scanning electron microscopy (SEM) was used to observe changes in morphology with heating. Imaging was performed with a JSM-7500F FESEM (JEOL) in LEI mode with an acceleration voltage of 1 kV, an emission current of 20 μA and working distance of 9 mm. As deposited and annealed 20 nm copper thin films were imaged and shown in Figure 5.5.

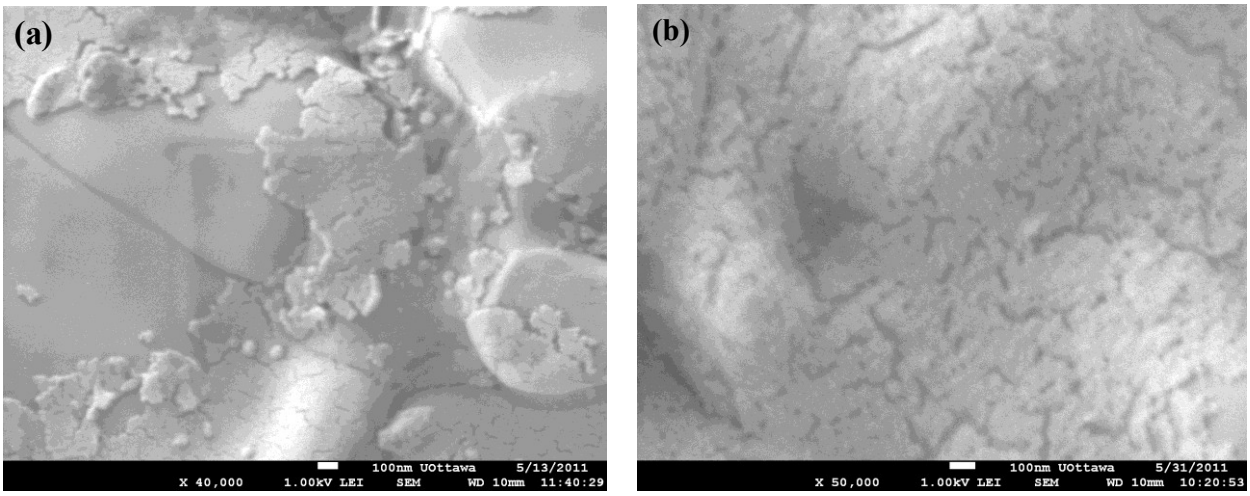

Figure 5.5 Microstructure of 20 nm copper film deposited on YSZ (a) as-deposited and (b) after annealing at 400°C for 2h in air

The microstructure of the as-deposited film shows a percolated microstructure with poor adhesion. After 2 hours of annealing at 400°C, the YSZ is visible through the percolated microstructure though thermal dewetting is not obvious.

5.4 Results and Discussion

Copper electrodes of 50 nm and 100 nm were synthesized for study and comparison, but cyclic voltammograms of 50 nm thin film showed distortion resulting from high ohmic resistances in the film, as seen in Figure 5.6.

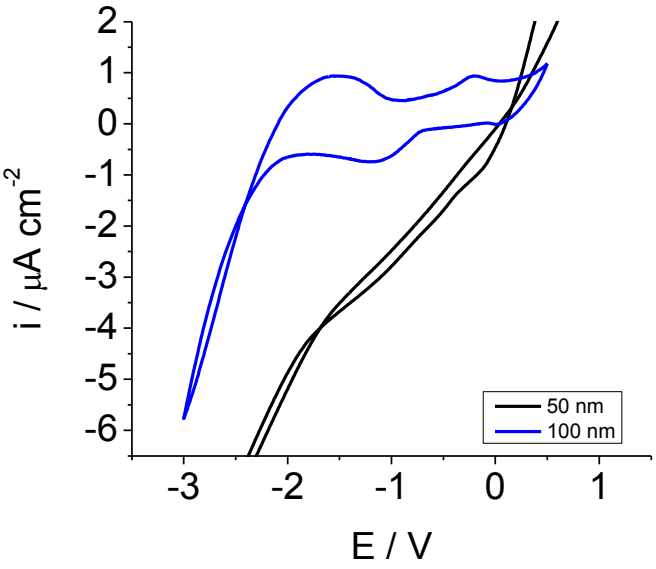

Figure 5.6 Film thickness effect on cyclic voltammogram distortion caused by ohmic resistances at 0 kPa, 350°C and ν = 20 mVs^{-1}

Copper is an excellent electronic conductor, while copper oxide is a semiconductor. Oxidation of 50nm films results in high IR. Thicker copper films have greater resistance to oxidation resulting from the self-limiting nature of the copper scale [15]. The film thickness dependence of thermally induced resistance changes in copper films on YSZ has been investigated in chapter 4.

A typical cyclic voltammogram for 100 nm copper film deposited on YSZ is shown in Figure 5.7 350°C in He with 0 kPa of O_2. Two cathodic (C1 and C2) and two anodic (A1 and A2) peaks are observed. At a starting potential of 500 mV, oxides scales form from the electrochemically induced backspillover of O^{2-} from the solid electrolyte in the vicinity of the three phase boundary. The presence of multiple peaks could be explained by the formation of oxides at different locations on the copper film or by the formation of different oxidation states in the copper electrode. Oxides may occur along the three phase boundary, two phase boundary as well as within the bulk of the electrode. Oxides formed at the interface of the electrode and

YSZ are insensitive to changed in partial pressure since they are not exposed to the gas phase. Peaks from the reduction of bulk oxides are shifted to lower potentials than those at the three phase boundary due to slow diffusion through a surface oxide.

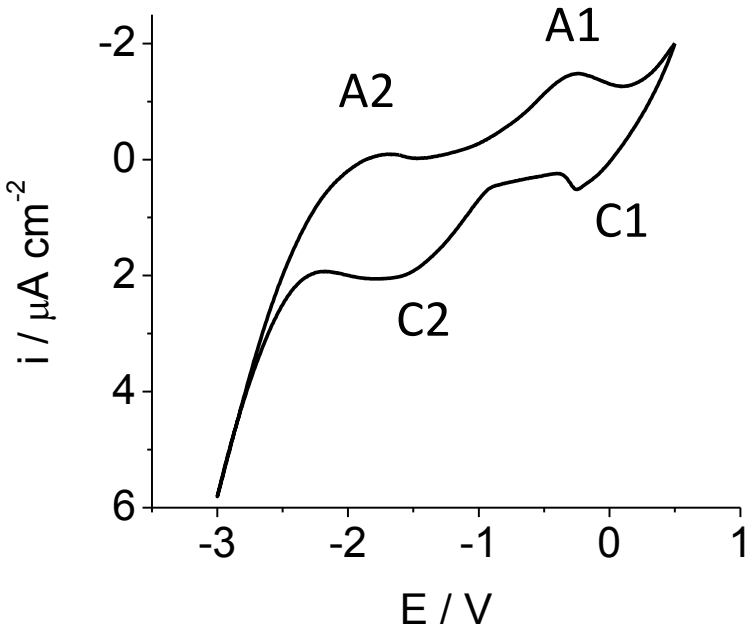

Figure 5.7 Typical cyclic voltammogram of 100 nm copper thin film, P_{O2}=10 kPa, T=350 °C, v=20 mVs^{-1}, E_i=0.5 V, E_s=-3 V

Another explanation for the presence of two sets of peaks is the formation of multiple oxidation states of copper, namely Cu_2O (Cu^+) and CuO (Cu^{2+}), during anodic polarization.

When scanning towards negative potentials, the CuO and Cu_2O are subsequently reduced according to equations (5.8) and (5.9) in peaks C1 and C2, respectively.

$$2CuO + 2e^- \rightleftharpoons Cu_2O + O^{2-} \tag{5.8}$$

$$Cu_2O + 2e^- \rightleftharpoons 2Cu + O^{2-} \tag{5.9}$$

Once the reduced film is anodically polarized, it is immediately oxidized to Cu_2O at peak A2. With increasingly positive potentials, the film is oxidized to CuO at peak A1.

In addition to electrochemical formation of oxides at the starting potential, E_i, the evolution of oxygen occurs concurrently at the three phase boundary via equation (5.10).

$$O^{2-}(\text{YSZ}) \rightleftharpoons \frac{1}{2}O_2 + 2e^- \tag{5.10}$$

The mechanism of electrochemical action can be elucidated by investigation of the effect of scan rate, oxygen partial pressure, starting potential and hold time at the starting potential.

The formation of oxides was found to be sensitive to the partial pressure of oxygen in the feed, as shown in Figure **5.8**a. With increased oxygen partial pressure, there is an increase in the slant of the scan as a result of increased ohmic resistances in the film caused by the presence of a native oxide layer. At 0kPa, all peaks are shifted to more positive potentials, indicating easier reductions, but more difficult oxidations than at higher partial pressures. At 1 kPa, there is an increase in the charge of peaks A1 and C1 and a decrease in peaks A2 and C2. Above 1 kPa, all peaks remain constant, save the A2 peak, which continues to decrease, as shown in Figure **5.8**.

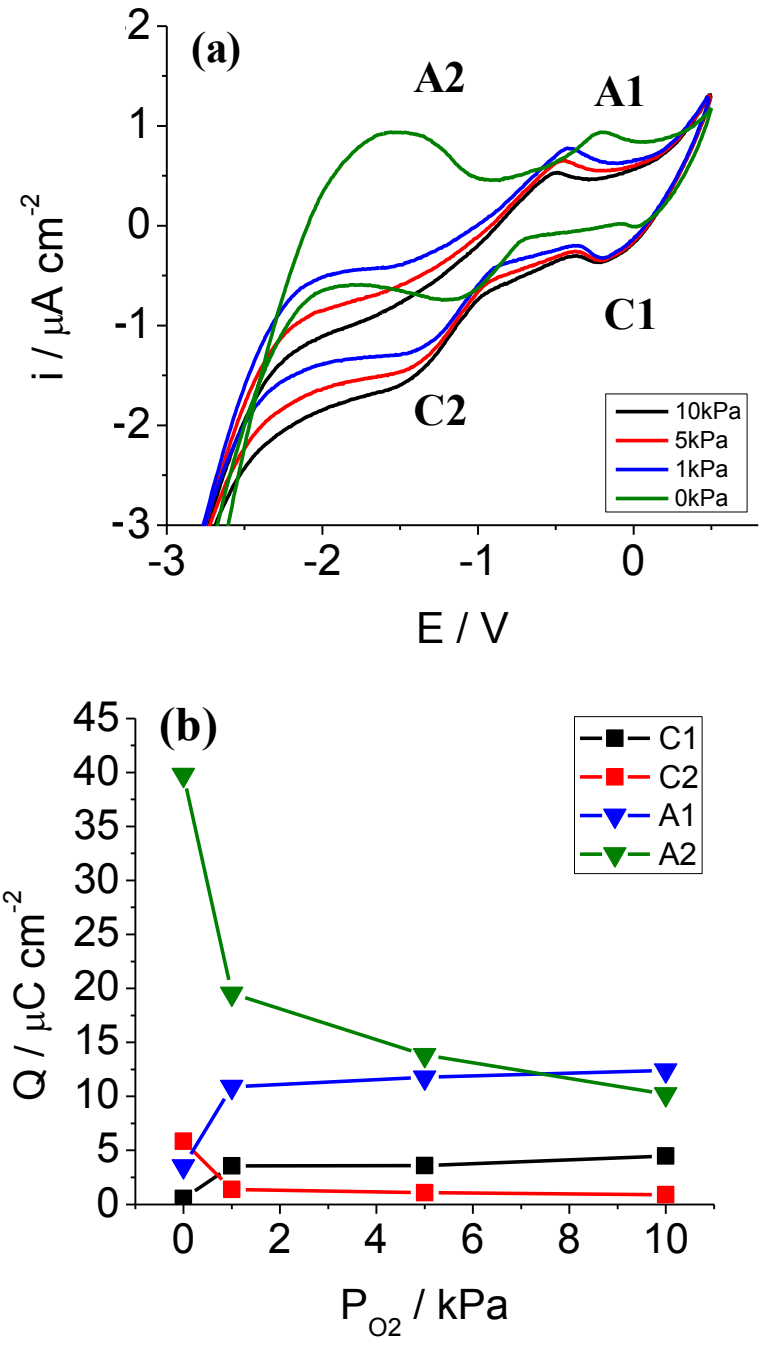

Figure 5.8 Effect of partial pressure of 100 nm copper film deposited on YSZ, (a) cyclic voltamogram, third cycle; T = 350 °C, v = 20 mV.s^{-1}, E_i = 500 mV, E_s = -3V, (b) Charge of anodic and cathodic processes

In the absence of oxygen in the feed, the native oxide layer is assumed to be minimal, while the competition between reactions chemical and electrochemical formation should strongly

favor the latter. In spite of this, the reductions of peak C1 and C2 are smaller in the absence of oxygen than in the presence of it, signifying that the oxides electrochemically formed at the start of the scan are readily desorbed before they can be electrochemically reduced. This suggests that the electrochemical backspillover associated with these peaks are surface phenomenon.

The chemical formation of copper oxides is proportional to $P_{O_2}^{\frac{1}{6}}$ [16] and, as a result, electrochemical oxidation peaks are expected to decrease with increasing partial pressure as the rate of chemical oxidation is increased with higher partial pressures. This decrease is most pronounced in peak A2, but is less apparent in A1 as a saturation point is rapidly achieved above 1kPa.

Changes in the positive potential, shown in Figure 5.9, have an impact on the peak current and potential of C1, C2 and A2 peaks. With decreasing starting potential, there is a decrease in the charge of peak C1 which is linear with respect to the starting potential. Peak C2 is shifted downward due to capacitor-like charging of the effective double layer, while the overall charge incurs little change. In addition, the charge of peaks C2 at higher positive potentials is smaller than peak C1, which would be expected for the formation of Cu_2O to CuO, but with decreasing positive potentials, this is not the case. The amount of oxides that have been reduced to Cu_2O is less than those used in the formation of Cu, indicating a concurrent reaction according to equation (5.11) must also occur.

$$\mathrm{CuO} + 2\mathrm{e}^- \rightleftharpoons \mathrm{Cu} + \mathrm{O}^{2-} \tag{5.11}$$

There is a slight decrease in the charge of A1 and A2 peaks indicating that the film is reduced to the same extent at -3 V. This dependence on positive potential indicates that the formation of oxides associated with peak C1 can be electrochemically controlled.

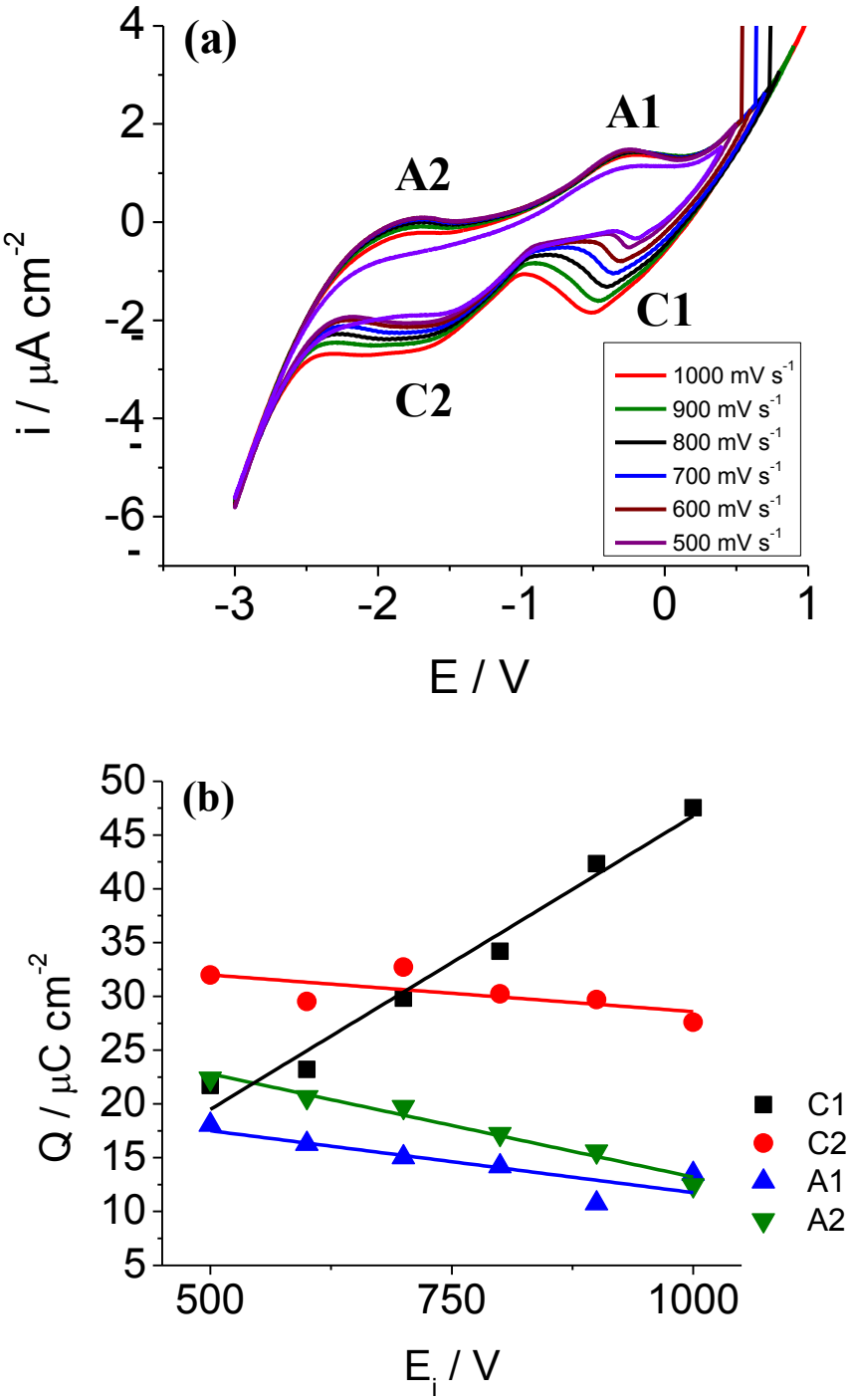

Figure 5.9 Effect of positive potential on the scan rate of 100 nm copper film deposited on YSZ, (a) cyclic voltammogram, third cycle; P_{O2} = 10 kPa, ν = 20 mV.s^{-1}, E_i = 0.5 V, Es = -3 V (b) Charge of anodic and cathodic processes

Figure 5.10 shows the affect of hold time on the first cycle for 100 nm copper thin film at 10 kPa. With increased hold times, the peak current of peak C1 and C2 increase and peak potentials shift to more negative potentials. The charge associated with C1 increases logarithmically with hold time which is consistent with a Mott-Cabrera mode of oxide growth, while that of C2 is distorted.

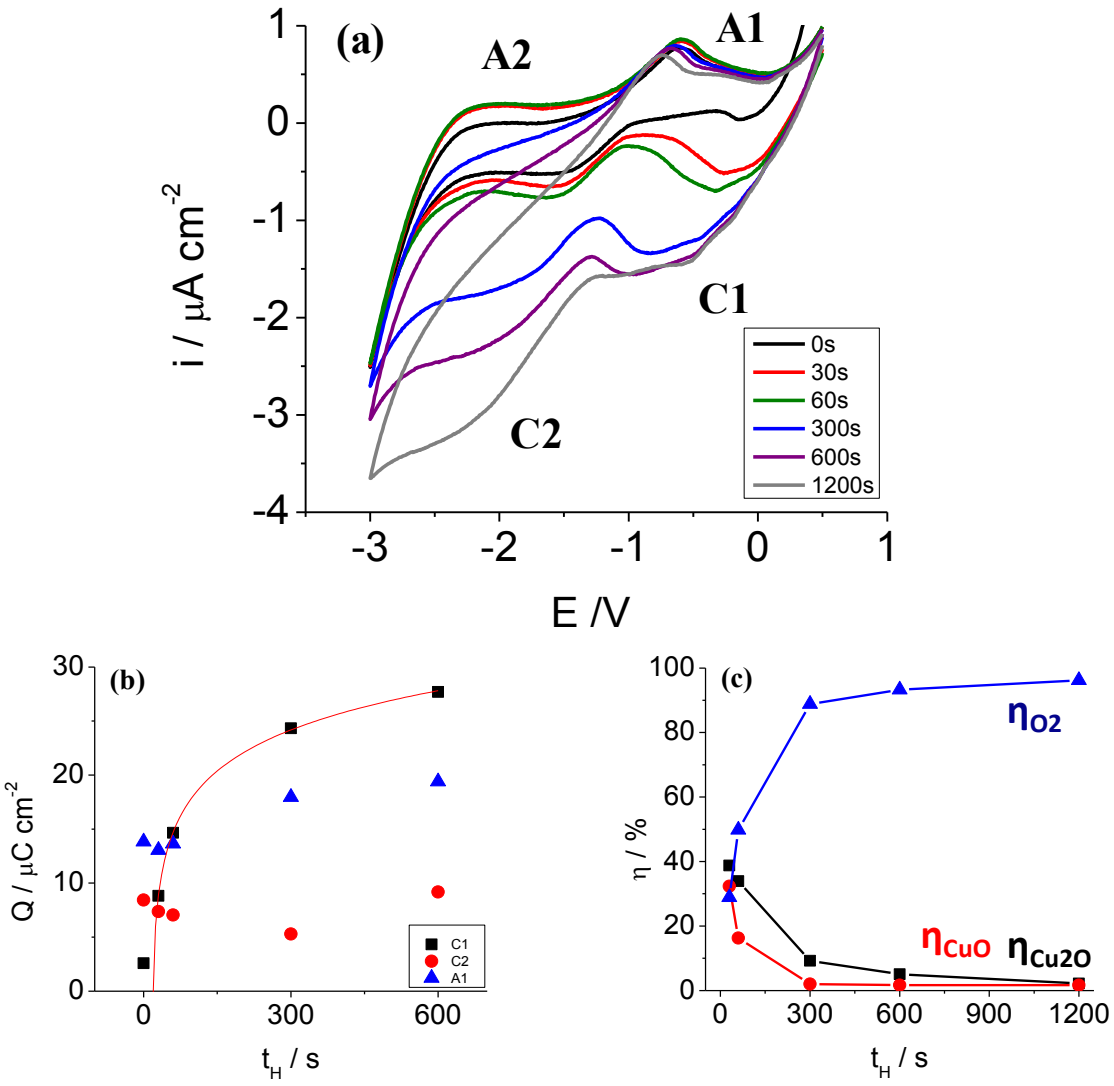

Figure 5.10 Effect of hold time on the cyclic voltammogram of 100 nm copper film deposited on YSZ (a) cyclic voltammogram, first cycle; T = 350 °C, P_{O2} = 10 kPa, v = 20 $mV.s^{-1}$, E_i = 0.5 V E_s= -3 V (a) total charge of anodic and cathodic processes, (b) Current efficiency for the formation of CuO, Cu_2O and oxygen evolution reactions

After prolonged use, the cyclic voltammogram undergoes changes caused by modification of the microstructure or chemistry of the film. Figure 5.11 shows the result for identical operating conditions separated by 4 days of operation.

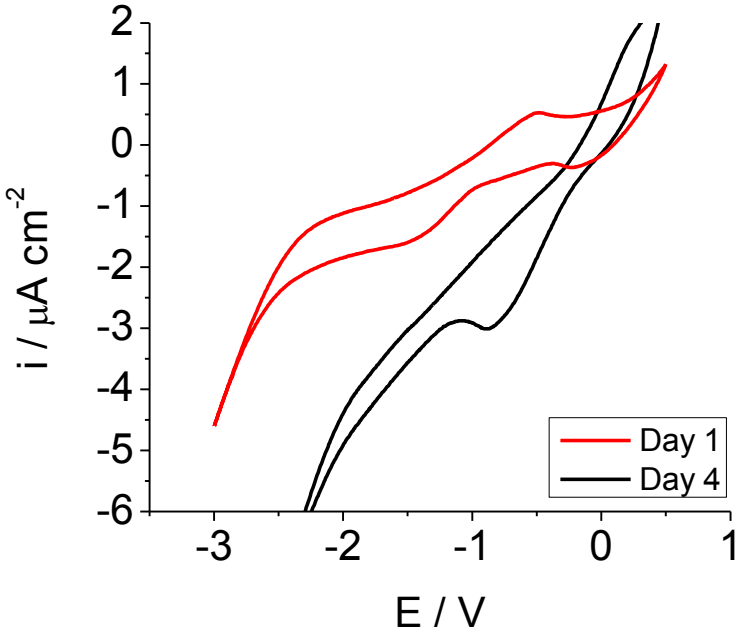

Figure 5.11 Effect of aging on 100nm copper deposited on YSZ, P_{O2} = 10 kPa, ν = 20 mV.s^{-1}, E_i = 0.5 V, E_s = -3 V

The cathode peaks both shift to more positive potentials and the A1 peak is flattened. Decrease in the capacitance of the film from less polarizable electrode.

The effect of scan rate on the aged film is shown in Figure 5.12. The trend of i_p to $\nu^{0.5}$ is linear for the anodic peak (A1) indicating that the anodic process is diffusion limited. The relation between i_p is not linear with $\nu^{0.5}$ or ν. The peak potential for the cathodic peak is linear with respect to ln ν, which is consistent with irreversible electrochemical reactions.

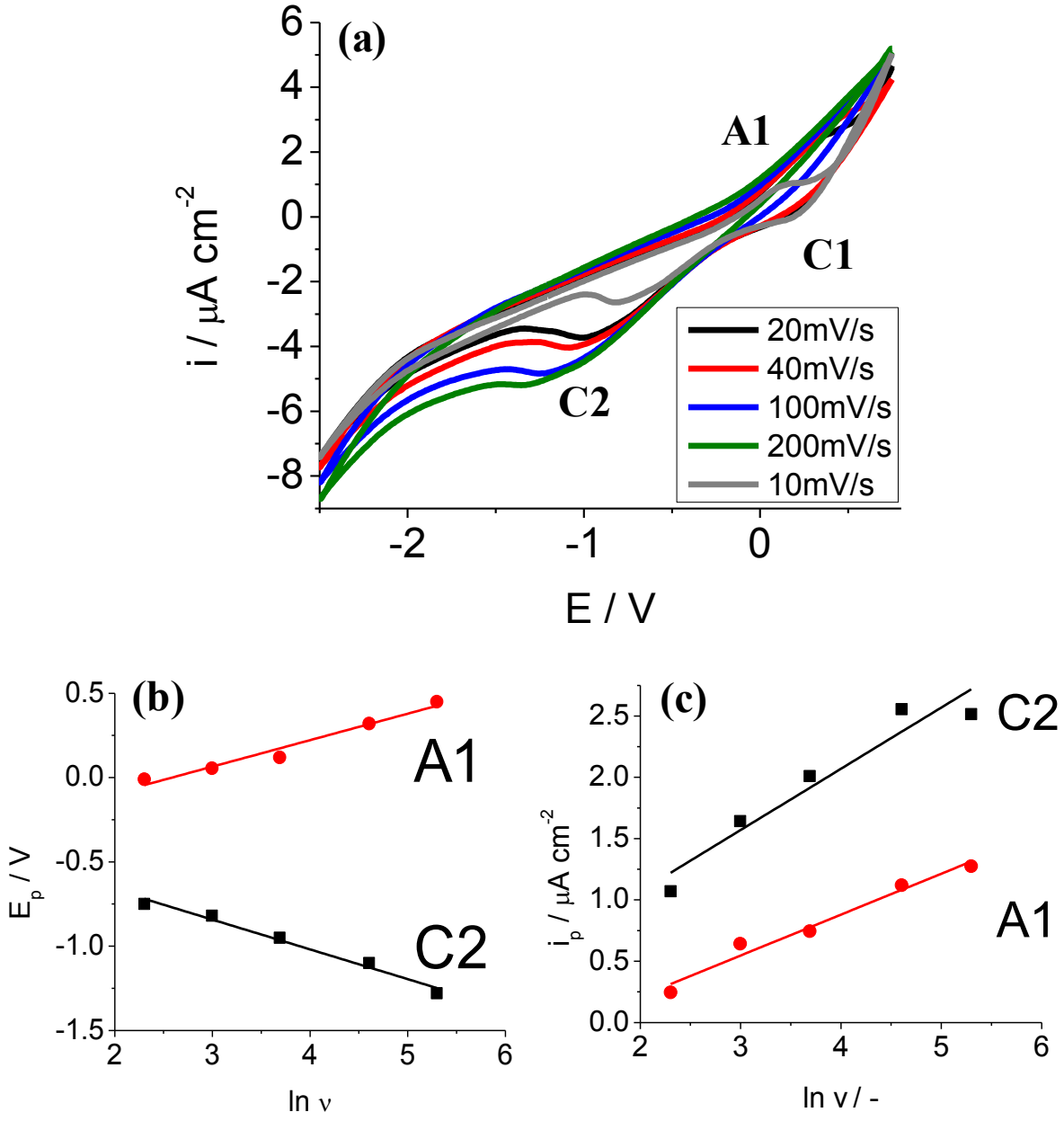

Figure 5.12 Effect of scan rate on 100 nm Copper film, (a) cyclic voltammogram, third cycle; T = 350 °C, P_{O2} = 10 kPa, E_i = 0.5 V, E_s = -2.5 V (b) potential peak current of anodic and cathodic processes, (c) peak current of anodic and cathodic processes

The relation between Ep and ln v is linear for both peaks which is in agreement with trends observed for irreversible electrochemical processes. The relation of i_P is linear with respect to ln v, which does not agree with diffusion or charge limited processes, which are linear

with respect to $v^{0.5}$ and v, respectively. This deviation may be due to the distortion of the data due to ohmic resistance in the film.

5.5 **Proposed Model**

The electrochemical behavior of Cu/O2, YSZ system is greatly impacted by the concurrent chemical interactions of copper in the presence of oxygen at 350 °C. At low film thicknesses, the presence of native oxide layers of comparable thickness to the thickness of the film result in high resistances in the film which appear as a slanted or distorted cyclic voltammogram. At higher film thicknesses, the presence of native and electrochemically grown oxides impact the behavior of the film.

Two cathodic peaks are observed in the cyclic voltammogram for copper which are representative of the reduction of CuO to Cu_2O and ensuing reduction to Cu at more negative potentials. The presence of adjacent peaks representing the formation location specific species were not observed. Additionally, the response of these peaks to partial pressure is evidence that the phenomenon occurs on the gas-exposed surface of the film.

With increased polarization time, both oxides forms according to a logarithmic relation which agrees with the Mott Cabrera model for thin oxide films. By varying the scan rate, changes in peak current values of the aged film were found to disagree with both diffusion and charge transfer limiting processes reported in the literature

5.6 **Conclusion**

Synthesis of 50 nm and 100 nm copper films on YSZ pellets were accomplished. Copper films of 50 nm were distorted from ohmic resistances arising from oxidation of the thin film. One hundred nanometer copper films show two sets of peaks corresponding to the

electrochemical reduction and formations of CuO and Cu_2O. These processes occur at the three phase boundary and exposed surfaces of the film and form according to Mott-Cabrera model for thin oxides. After prolonged use there is significant aging of the film resulting in distortion of the cyclic voltammogram caused by ohmic resistances in the oxidized film.

5.7 **References**

[1] M. V. Twigg, M. S. Spencer, *Applied Catalysis A: General*, 212, 161–174, (2001).

[2] K. V. R. Chary, G. V. Sagar, C. S. Srikanth, V. V. Rao, *The journal of physical chemistry. B*, 111, 543–50, (2007).

[3] A. Baikerb, A. Wokaun, *Phys. Chem. Chem. Phys.*, 5071–5080, (1999).

[4] W.-P. Dow, T.-J. Huang, *J. Catal.*, 160, 171–182, (1996).

[5] R. G. Silver, C. J. Hou, J. G. Ekerdt, *J. Catal.*, 118, 400–416, (1989).

[6] N. Jackson, J. G. Ekerdt, *J. Catal.*, 126, 31–45, (1990).

[7] R. J. Gorte, S. Park, J. M. Vohs, C. Wang, *Advanced Materials*, 12, 1465–1469, (2000).

[8] S. Park, R. Craciun, J. M. Vohs, R. J. Gorte, *J. Electrochem. Soc.*, 146, 3603, (1999).

[9] S. McIntosh, R. J. Gorte, *Chem. Rev.*, 104, 4845–65, (2004).

[10] E. I. Papaioannou, S. Souentie, a. Hammad, C. G. Vayenas, *Catal. Today*, 146, 336–344, (2009).

[11] I. Platzman, R. Brener, H. Haick, R. Tannenbaum, 1101–1108, (2008).

[12] Y. Zhu, K. Mimura, J. Lim, M. Isshiki, Q. Jiang, *Metallurgical and materials transaction*, 37A, (2006).

[13] S. Haleem, B. G. Ateya, *J. of Electroanal. Chem.*, 117, 309–319, (1981).

[14] P. van Manen, R. Weewer, J. de Wit, 139, 1130–1134, (1992).

[15] J. C. Yang, B. Kolasa, J. M. Gibson, M. Yeadon, *Appl. Phys. Let.*, 73, 2841, (1998).

[16] N. Birks, G. Meier, *Introduction to High Temperature Oxidation of Metals* (Edward Arnold, London, ed. 1, 1983), p. 198.

Chapter 6 Silver Thin Films Interfaced with Yttria-Stabilized Zirconia

The critical thickness of silver thin films on YSZ was determined to be 5.4 ±0.4 nm for a deposition rate of 0.5 $nm.s^{-1}$. Despite this, silver thin films were found to be thermally unstable below thicknesses of 600 nm for operation at 350 °C and so the behaviour of silver under polarization was investigated for an 800 nm film. With application of positive potential silver oxides were found to form along the three phase boundary and extend within the bulk of the electrode with increasing anodic hold times. This oxide forms according to a logarithmic rate expression with thick oxides being associated with reduction in current efficiency for subsequent oxide formation.

6.1 Introduction

Silver on yttria stabilized zirconia (YSZ) has been studied as a potential cathode material in solid oxide fuel cells (SOFC) due to its high catalytic activity and high oxygen solubility and mobility [1]. Unfortunately, due to its low melting point and high volatility, applications with temperatures greater than 850 °C are not suited to the thermally unstable silver films [2, 3]. As a result, intermediate temperature (475-500 K) micro-solid oxide fuel cells featuring silver have been studied [4].

According to Butler-Volmer equation, with decreasing temperatures, the charge resistance increases. This results in more ideally polarizable electrodes [5, 6], which are of interest for the electrochemical promotion of catalysis (EPOC) [7–11]. Early investigations of the electrochemical promotion of silver were carried out on thick silver paste films. Using potential

programmed desorption [12], potential programmed reduction [10] and surface enhanced Raman Spectroscopy [9], these studies demonstrated the presence of two types of adsorbed oxygen species: the first a chemisorbed O_{ADS} and the second a backspilled O^{2-} from the support.

In addition to this electrochemical activity on YSZ, silver has proven to be an effective catalyst in the epoxidation of ethylene [13, 14] and selective reduction of NOx [15]. Given the history of silver films with electrochemical promotion and the high electric conductivity, investigation of a well defined electrode is interesting.

6.1.1 Silver Electrodes in Aqueous Electrolytes

The electrochemical behavior of polarized silver films have not been investigated in solid electrolyte systems, but parallels may be drawn with Ag electrodes in aqueous systems [16, 17]. Cyclic voltammetry studies of silver electrodes in literature have been focused on aqueous systems in alkaline solution [18–20] for rechargeable silver oxide batteries. The anodic growth of oxides on silver electrodes in alkaline solution proceeds via a two step mechanism [21, 22] First, the formation of bulk Ag_2O occurs through creation of a AgOH or Ag_2O monolayer on the silver electrode and subsequent growth through a solid state diffusion limited mechanism until a 3D primary silver (I) oxide is formed [21]. Secondly, the formation of AgO proceeds through nucleation and crystal growth processes, which are slow and are observed only at low scan rates [21]. In spite of this two step mechanism, cyclic voltammograms in the literature show a complexe shape with more than two anodic peaks. Figure 6.1 shows a sample of the cyclic voltammograms obtained in 1.0 M NaOH between -1.68 V and 0.9 V, which identified 5 anodic peaks [18]. At -1.68 V, the electrode is reduced and exists as Ag^0 near the hydrogen evolution potential.

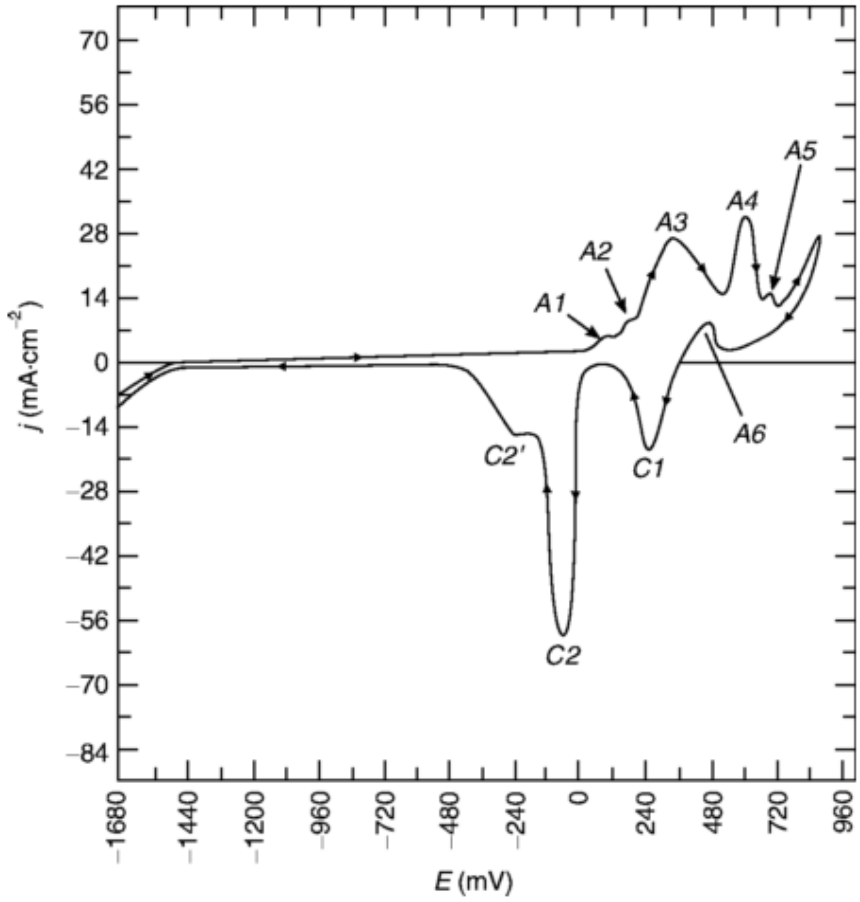

Figure 6.1 Cyclic voltammetry of silver electrode in 1.0 M NaOH between $E_{s,c}$=-1680 mV and $E_{s,a}$ = 900 mV at 25°C and 100 mV s^{-1}[18]

Work by Hepel *et al.* [20], Giles et al. [23] and Droog [24] have lead to the identification of three peaks associated with the formation of Ag_2O: the electrodisolution of surface $[Ag(OH)_2]^-$, electroformation of a base Ag_2O layer or O^- layer trapped at the silver surface and finally the electroformation of bulk Ag_2O through 3D growth into the silver lattice. These account for peaks A1, A2 and A3, respectively. Peak A1 represents the electro-dissolution of Ag to $[Ag(OH)_2]^-$ is observed and proceeds via equations (6.1) and (6.2).

$$Ag + 2OH^-_{ADS} \rightleftharpoons [Ag(OH)_2]^-_{ADS} + e^- \quad (6.1)$$

$$[Ag(OH)_2]^-_{ADS} \rightleftharpoons [Ag(OH)_2]_{AQ} + e^- \quad (6.2)$$

With increased potential, silver electrode forms a monolayer of Ag_2O according to equation (6.3), labeled as peak A2. Subsequent growth of bulk oxides proceeds solid state diffusion process and appears as a higher potential peak at A3.

$$2Ag + 2OH^- \rightleftharpoons 2Ag_2O + H_2O + 2e^- \quad (6.3)$$

Oxidation of the Ag_2O leads to the formation of AgO at high positive potential according to equation (6.4).

$$Ag_2O + 2OH^- \rightleftharpoons 2AgO + H_2O + 2e^- \quad (6.4)$$

With increased potential, oxygen evolution reaction occurs with the proposed simultaneous formation of Ag_2O_3 according to equation (6.5)

$$2AgO + 2OH^- \rightleftharpoons Ag_2O_3 + H_2O + 2e^- \quad (6.5)$$

On cathodic scan, three cathodic peaks are observed and a single anodic process. Peak A6 is attributed to the continuation of the nucleation and growth of Ag_2O associated with peak A3. Peak C1 described the electroreduction of AgO to Ag_2O, while peak C2 and C2' are related to the electroreduction of Ag_2O to Ag in a two-step process. Further investigations by Abd El Rehim *et al.* [18] found that in alkaline media and high positive switching potentials (Es), the formation of AgO proceeds via charge transfer and diffusion limited oxide growth mechanism, resulting in a peak and shoulder not observed at lower positive potentials (E_s<730mV). This is attributed to the thicker Ag_2O formed at potentials greater than 730 mV which stemming from the high solubility of oxygen in silver.

The presence of multiple oxidation states (Ag^+, Ag^{2+}, Ag^{3+}) as well as the sensitivity of oxide formation location in silver electrodes to changes in the potential window can be used to

understand high temperature electrochemical response of silver electrodes to polarization in gaseous environments.

6.2 Experimental

Yttria stabilized zirconia discs were synthesized as outlined in Chapter 3. Silver films were synthesized using evaporative physical vapor deposition with resistive heating of tungsten dimble boats (Kurt J. Lesker) at 2.5E-5 mBar in a BOC Auto306. Metal slugs (99.99% metal basis, Alpha Aesar) were heated until a deposition rate of 0.5 $nm.s^{-1}$ was achieved as measured in-situ with a quartz microbalance thin film monitor (Edwards, FTM5). Films of 50, 100, 400, 500 and 800 nm were deposited onto the YSZ and the cell assembled as outlined in Section 4.3 and placed in reactor setup shown in Figure 4.4 (with WE=Silver).

6.3 Characterization of Ag Electrode Deposited on YSZ

Scanning electron microscopy (SEM) was used to observe changes in morphology of the of the thin Ag films as a result of elevated temperatures and polarization. Imaging was performed with a JSM-7500F FESEM (JEOL) in LEI mode with an acceleration voltage of 1 kV, an emission current of 20 μA and working distance of 9 mm. In section 6.3.2 the percolation threshold of silver films on YSZ was found to be 3.0 ± 0.5 nm. As deposited silver films greater than 100 nm are continuous and show no exposed substrate, as seen in Figure 6.2a.

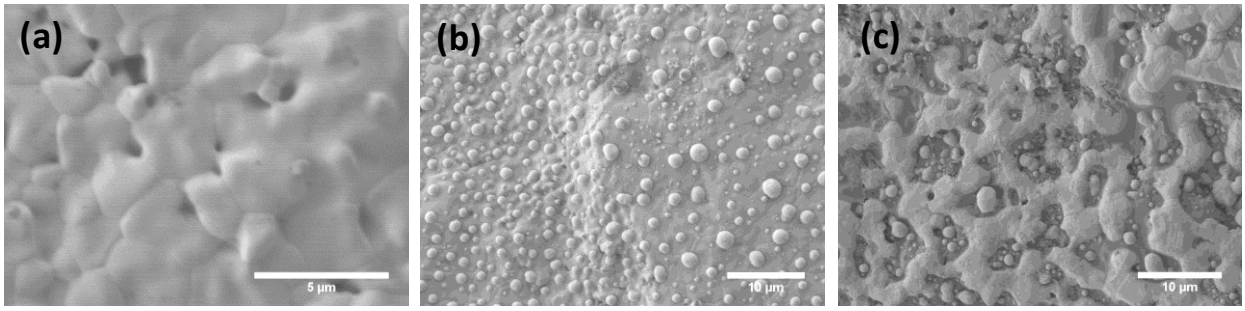

Figure 6.2 SEM of (a) as-deposited 100 nm silver film (b) used 100 nm silver film and (c) used 800 nm silver film on YSZ

Figure 6.2 shows the effects of thermal dewetting of silver films on YSZ. This phenomenon was investigated earlier by Simrick *et al.* [2]. The microstructure of heat-treated thin films was found to be a function of initial thickness of the film, annealing temperature and annealing time [2]. Thin films dewet or pull away from the substrate when annealed to lower interfacial surface energies, resulting in simultaneous grain coarsening and thermal grooving along grain boundaries. Film rupture is accompanied by hole growth forming electronically percolated channels and eventually single grain or multi-grain islands. Similar behaviour is seen in Figure 6.2b for 100 nm silver films which have been annealed at 550°C for 1 hour and subsequently polarized at 350°C in dilute oxygen in helium (20 kPa). In the thicker silver films, the change in microstructure is slower. The surface self-diffusion of silver is not dependant on film thickness, but, since there is more silver to move for film rupture to occur, thicker films are more thermally stable. Thick films result in thermally stable percolated networks with high three phase boundaries, as shown in Figure 6.2c for 800 nm silver film. The results presented in this chapter are therefore given for thermally stable 800 nm silver after pre-treatment at 550°C for 1 hour.

6.3.1 X-ray Photoelectron Spectroscopy

Further characterization was accomplished using X-ray photospectroscopy (XPS) measurements. These were used to determine surface composition and oxidation state of Ag film XPS measurements were performed with KRATOS Axis Ultra DLD with a Hybrid lens mode and conducted at 140 W and pass energy 20 eV using a monochromatic AlKα. Results were corrected for a C1s peak of 285 eV and are shown in Figure 6.3.

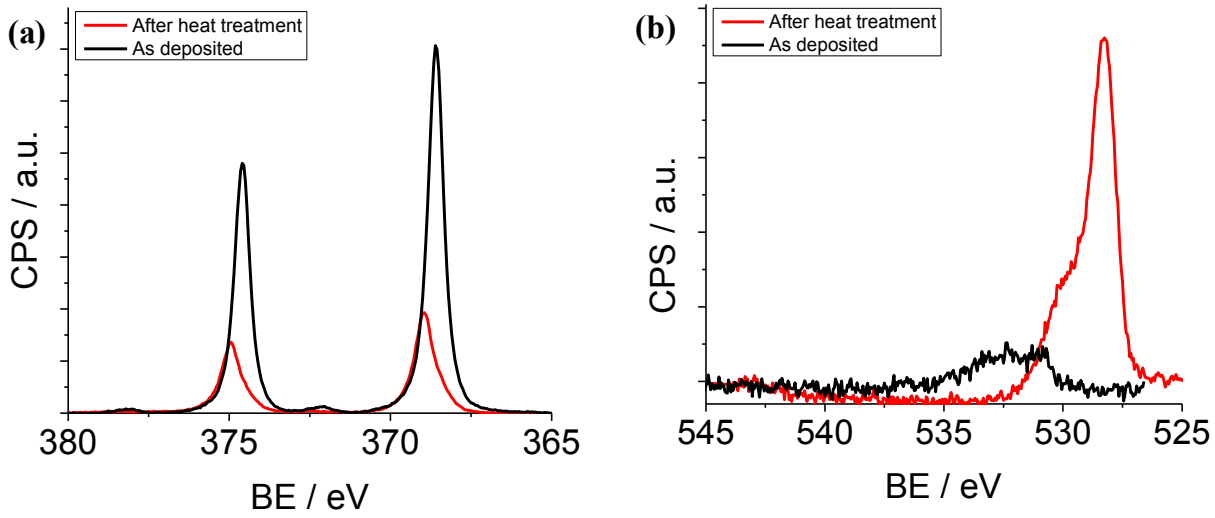

Figure 6.3 XPS of 100 nm (a) $Ag3d_{5/2}$ and $Ag3d_{3/2}$ peaks (b) O1s peak

A summary of the analysis of the XPS spectra for the Ag3d $_{5/2}$ and Ag3d $_{3/2}$ peaks is shown in Figure 6.3. After thermal treatment and polarization, there is a slight increase in the full width at half max (FWHM) from 0.658 eV to 0.890 eV. This indicates that the electrode remains in its metallic state. This is confirmed by the O1s peaks shown in Figure 6.3. Oxygen signal is very low in the as deposited sample, confirming that metallic Ag film completely covers yttria-stabilized zirconia support. After the heat treatment, O1s signal increases significantly indicating the presence of oxygen on Ag surface and/or uncovering the YSZ support, due to Ag film sintering as also confirmed by SEM.

6.3.2 *In-situ* Resistance

Critical Thickness

The critical thickness of thin silver films on YSZ was determined for a deposition rate of 0.5 $nm.s^{-1}$using the in-situ measurement technique described in Section 4.2. Figure 6.4 shows the results. Fitting this data to the scaling relation given in equation (2.56), the percolation threshold was determined to be 5.4 ± 0.4 nm.

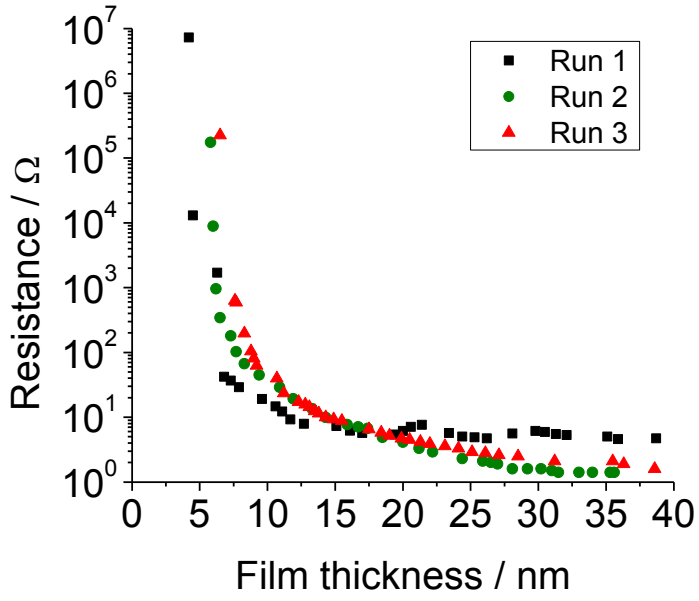

Figure 6.4 Insitu resistance measurements of silver during deposition at a rate of 0.5 $nm.s^{-1}$

Post-deposition Heat Treatment

Measurement of the film thickness dependence on thermal stability of silver thin films on YSZ were determined using in-situ resistance measurements. Pellets were prepared as outlined in Chapter 3 and were painted with two gold electrodes, as shown in Figure 4.3. Silver films were

deposited to thicknesses of 100, 370, 500 and 600 nm with a deposition rate of 0.5 $nm.s^{-1}$ and at a pressure of $2.5x10^{-5}$ mBar.

Electrical connections were done with gold wire and small NiCr clips. The cell was placed in a reactor shown in Figure 4.5. Helium (4.7 grade) and oxygen (4.7 grade) were controlled with MKS 1359C mass flow controllers.

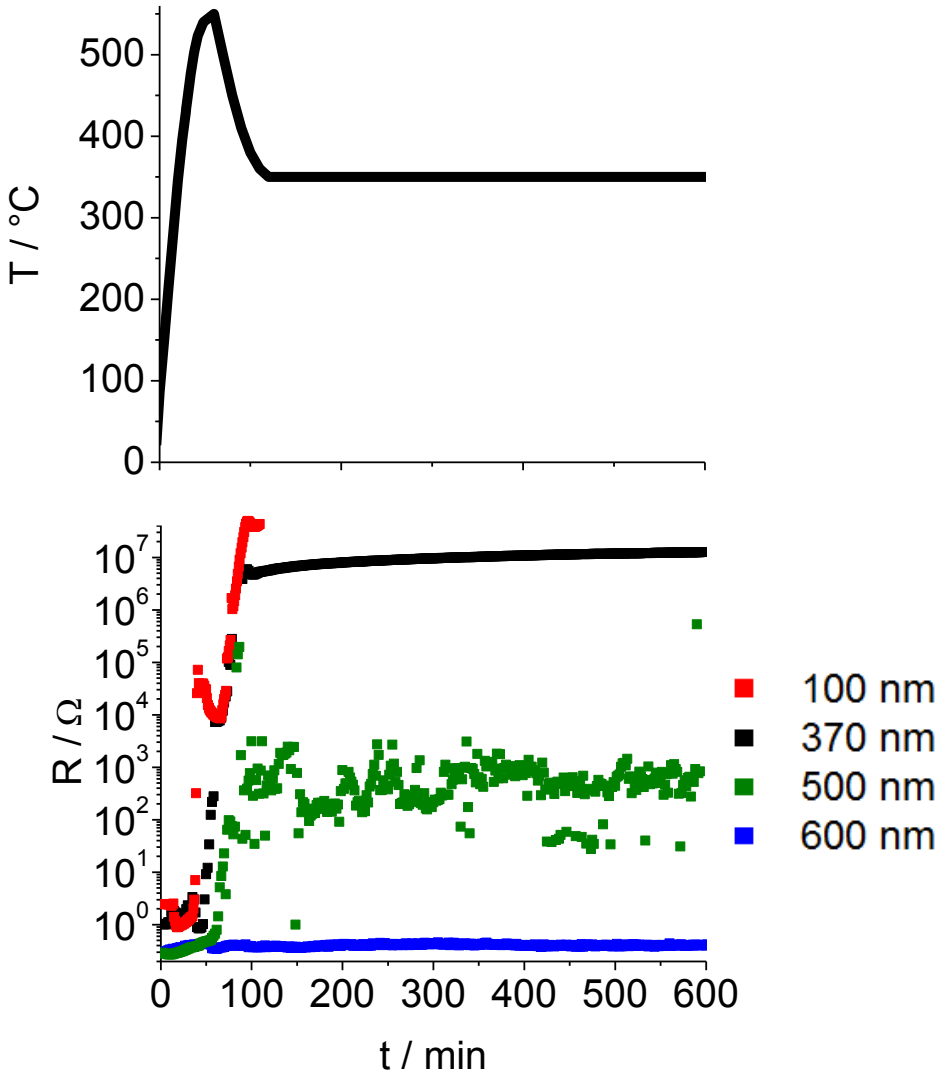

Figure 6.5 Effect of film thickness on the thermal stability of thin films.

The cell was heated to 550°C in air for the first hour to simulate the pre-treatment used in the electrochemically tested films. After this hour, the film was cooled to 350°C and placed in a dilute oxygen helium stream (P_{O2}=6 kPa , F_{TOT} = 50mL min^{-1}) to simulate operating conditions. From the results shown above, films of 500 nm became non-conductive within the first 100 min of the test, while the 600 nm film was stable for 49.5 hours (not shown)

6.4 Results and Discussion

Figure 6.6 shows a typical cyclic voltammogram of an 800 nm Ag thin film interfaced with YSZ at P_{O2}=6 kPa and T=350°C.

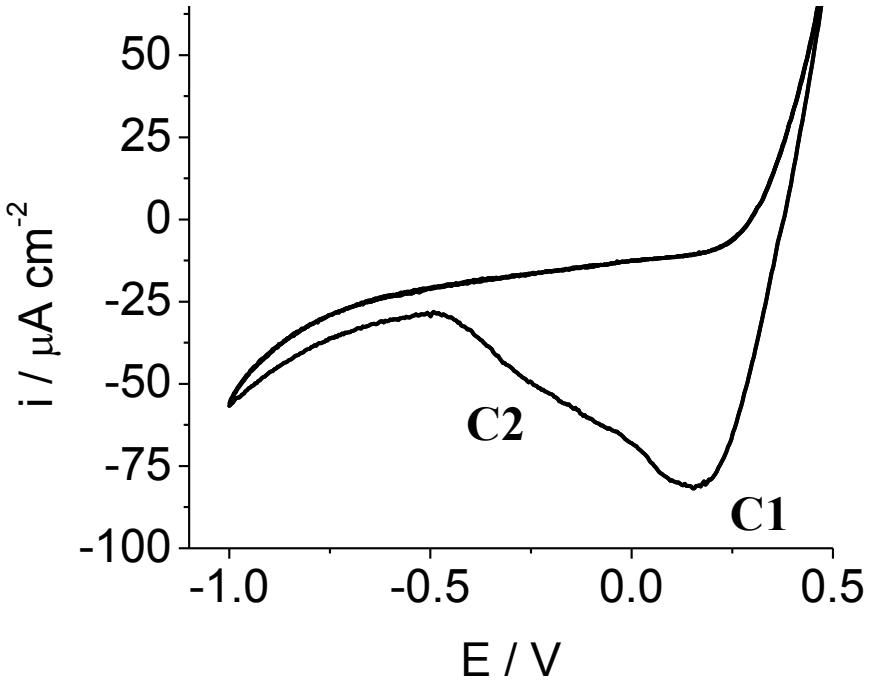

Figure 6.6 Cyclic voltammogram of 800 nm silver thin film on YSZ, T=350°C, v=20mV/s, E=-1.0V-1V, P_{O2}=6kPa

There is a cathodic peak, C1 at 0.15V with a shoulder, C2, at lower electrical potential, and no anodic peaks. Given that chemically formed oxides decompose at temperatures above 462 K

according to the Ellingham diagram, the film is assumed to be in the silver metal state (Ag^0) under open circuit conditions at 350°C. At a starting potential of 240 mV, both oxygen evolution at the three phase boundary and the electrochemical formation of Ag_2O occur. The silver oxide may be formed by the reaction of Ag with backspillover of O^{2-} from the YSZ at the three phase boundary to form Ag_2O at the three phase boundary according to equation (6.6). The grows outward from the three phase boundary, forming bulk Ag2O according to equation (6.7)

6.5 $$Ag + O^{2-}(YSZ) \rightleftharpoons Ag_2O_{tpb} + 2e^- \quad (6.6)$$

$$Ag_2O_{tpb} \rightleftharpoons Ag_2O_{bulk} \quad (6.7)$$

The electrochemically formed Ag_2O is subsequently reduced in peak C1 and shoulder C2. At E_i<400mVa neither peak is present. Above E_i=400mV, a small anodic peak at 120 mV appears. Moreover, dependence of the peak C1 and on the positive potential limit (Figure 6.7) clearly indicates that the oxidation of Ag takes place in the anodic scan, and probably overlaps with the O_2 evolution process (2.31)

Additionally, there is an exponential increase in the peak charge indicating an increase in oxides formed at higher starting potentials. A shift in the peak potential is expected when a passivating scale inhibits the formation of subsequent oxides, as was found for anodic formation of bulk Ag_2O in aqueous systems [25]. The peak shifts slightly toward more positive potentials, indicated a faster reduction, but increases after E_i = 900 mV

The absence of this indicates sub-monolayer formation of oxides either at the two phase boundary or extending outward from the three phase boundary to cover the films exposed surface. According to Faraday's law, the moles of the oxide in the monolayer can be calculated

from total charge of the cathodic peak and lies between 1.53 nmol.cm^{-2} (900 mV) and 2.83 nmol.cm^{-2} (1000 mV) according to Faraday's law (equation (4.5))

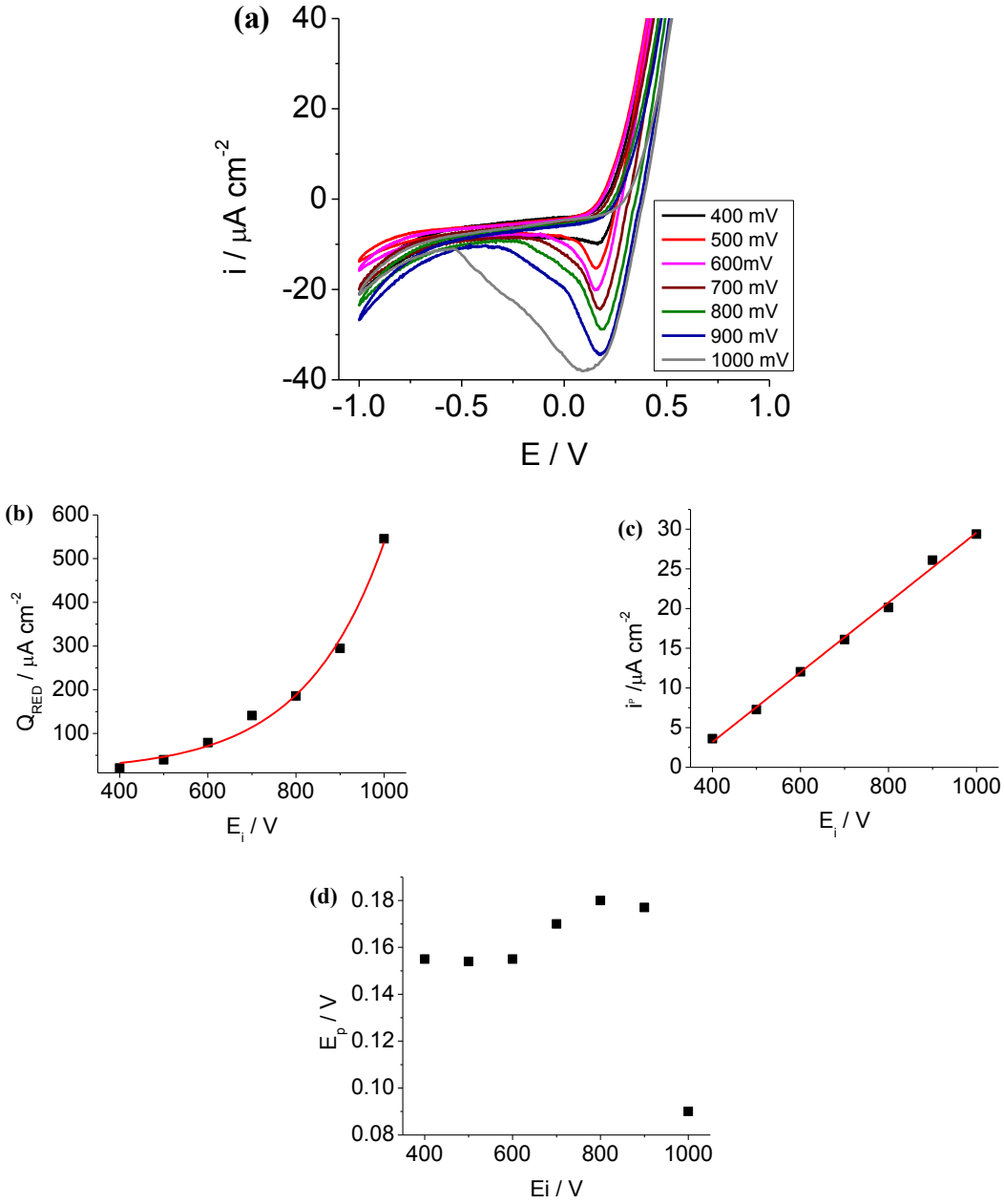

Figure 6.7 Effect of positive potential on CV of 800 nm silver film deposited on YSZ, (a) CV, third cycle, T=350°C, *v*=20mV/s (b) charge of reduction process (c) peak current and (d) peak potential

The kinetics of these processes can be determined by varying the scan rate, as shown in Figure 7.1. With increasing scan rate, there is an increase in peak current and a shift in the peak potential to more negative values.

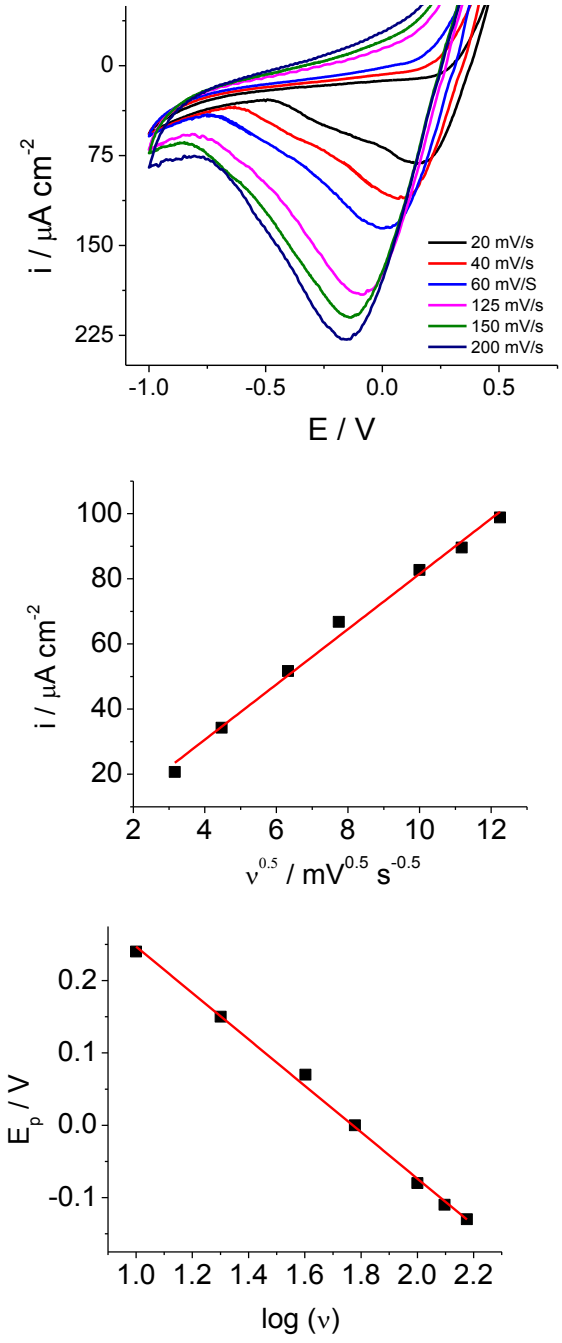

Figure 7.1 Effect of scan rate on the cyclic voltammogram of 800 nm Ag thin film on YSZ, T = 350°C, P_{O2} = 6 kPa, E_i = 1000 mV, E_s = -1000 mV

The relation of peak current is linear with respect to $v^{0.5}$, which is consistent with a diffusion limited processes according to the Sevcick equation. Furthermore, the change in scan rate is linear with the natural logarithm of the scan rate and agrees with equation (6.8), which described the irreversible reduction of an adsorbed electroactive species.

$$\Delta V_{WR} = -\left(\frac{RT}{\alpha_C n_C F}\right)\Delta \ln(\upsilon) \qquad (6.8)$$

Further information about the mechanism of anodic oxide formation can be determined by increasing the hold time at the start of the scan, as shown in Figure 7.2. Two regions of behavior can be observed in this data. The first region, at hold times below 60s, is characterized by increase in peak current and a shift in peak potential to more negative values as hold time is increased. During this stage, initial current is constant at an average of -163 μA cm^{-2} and is consistent with the formation of passivating oxide layer, though there is insufficient data to conclude whether mechanism follows parabolic or logarithmic growth mode. Above 60 s, there is a drop in initial current and a shift to more positive peak potentials. This results in low current efficiencies for the formation of oxides resulting from the inhibiting nature of Ag_2O scale.

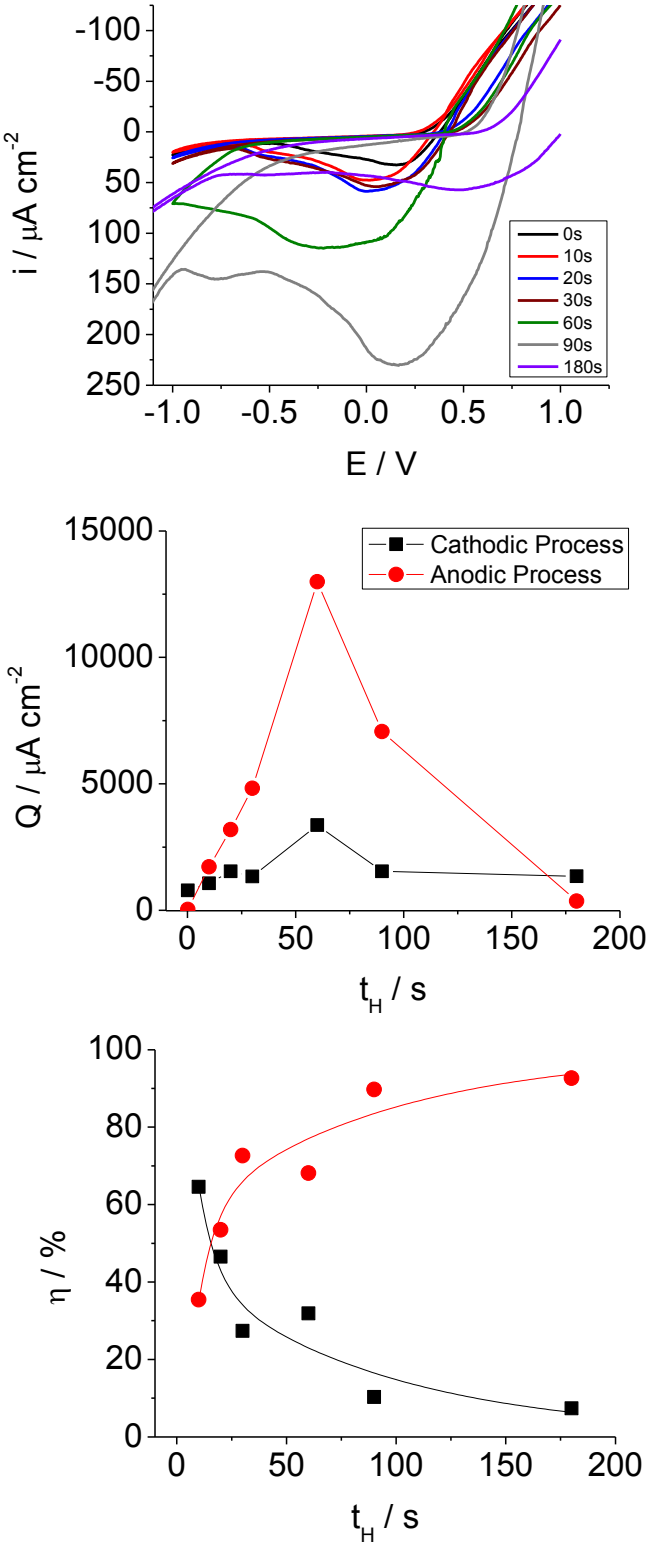

Figure 7.2 Effect of hold time for 800 nm silver film on YSZ, T=350°C, P_{O2} = 6 kPa = 20mV^{-1}

6.6 **Proposed Model**

A model for the oxide storage of silver on YSZ is presented below. In the literature, models for the O_2/Me, YSZ system behavior have been presented for nickel [26], palladium [27], platinum [17, 28] films based on cyclic voltammetry studies. The model below is discussed in relation to these studies.

The investigation of thick paste platinum film identified a single Pt/PtO pair wherein the anodic peak was suppressed at higher partial pressures due to the competitive nature of the electrochemical/chemical oxidation reactions on the electrochemically reduced film. The cyclic volatmmetry of sputtered nickel films (880 nm), presented by Souentis *et al.*, showed a single cathodic peak identified as the reduction of NiO, formed electrochemically at initial potentials in excess of 150 mV [26]. Silver similarly presented no anodic peak, but the presence of multiple cathodic peaks is consistent with sputtered platinum films studied by Falgairette *et al.*, wherein location specific oxides resulted in multiple adjacent cathodic peaks [28]. The backspillover of O^{2-} from the YSZ, may occur along the three phase boundary, at the two phase boundary of electrode and YSZ or may migrate through existing scale to form bulk oxides [29]. Based on the behavior of silver electrodes in aqueous alkaline systems [18] and the high oxygen mobility within silver [2], the formation of bulk silver is likely, however due to the insensitivity of peak A1 to changes in positive potential, it is likely that the bulk oxides are found in shoulder A2, while A1 is attributed to a surface oxide.

With increased initial potential, there is an increased oxide formation, which resulted in the nickel model as a linear increase in charge and decrease in peak potential towards more negative potentials [26]. A similar charge increase was observed for silver film without shift in

electrical potential. As a result, the oxide is assumed to be a sub-monolayer (charge transfer limited) for charges lower than 294 μC cm^{-2}.

With change in scan rate, silver was found to be in agreement with Sevcik equation for diffusion limited processes. With increased initial hold time, there is an increase in oxide formation until 60s, after which the current drops and electrochemical activity decreases on account of the presence of oxides at electroactive sites.

The platinum model presents a sub-monolayer to single monolayer formation of oxides along the three phase boundary which propagates along the interface between Pt and YSZ upon higher polarization times [30, 31]. This is due to the low oxygen solubility in platinum. The nickel model favors the formation of oxides along the interface according to Wagner's theory in which a passivating layer of oxides forms, preventing the formation of further oxides [26].

6.7 **Conclusion**

Thin silver films of 50 nm and 100 nm are thermally unstable at 350°C under low oxygen partial pressures. Solid electrolyte cyclic voltammetry has been used to illustrate the formation of Ag_2O with positive polarization from the electrochemically backspillovered O^{2-} species from the YSZ support. At low starting potentials (400 mV<E_i< 500 mV), a single cathodic peak is observed, corresponding to a submonolayer surface oxide. Increase in potential results in the appearance of a shoulder at lower potentials which corresponds to the formation of bulk oxides. For initial potentials greater than 900 mV, mechanism becomes diffusion limited and oxides form according to a logarithmic rate expression. This is corroborated by studies of the effect of scan rate above 900 mV, for which the peak current is linear was found to be linear with respect to $v^{0.5}$ according to the Sevcik-Randles equation. With increases in anodic polarization time,

thicker oxides form which suppress electroactive sites, resulting in reduced currents as well as reduced current efficiency for the formation of subsequent oxides.

6.8 **References**

[1] A. Cantos-Gómez, R. Ruiz-Bustos, J. van Duijn, *Fuel Cells*, 11, 140–143, (2011).

[2] N. J. Simrick, J. a. Kilner, a. Atkinson, *Thin Solid Films*, 520, 2855–2867, (2012).

[3] H. C. Kim, T. L. Alford, D. R. Allee, *Appl. Phys. Let.*, 81, 4287, (2002).

[4] J. H. Shim, Y. B. Kim, J. S. Park, J. An, T. M. Gür, F. B. Prinz, *J. Electrochem. Soc.*, 159, B541, (2012).

[5] J. Janek, M. Rohnke, B. Luerssen, R. Imbihl, *Phys. Chem. Chem. Phys.*, 2, 1935–1941, (2000).

[6] H. Pöpke, E. Mutoro, B. Luerßen, J. Janek, *Catal. Today*, 202, 12–19, (2013).

[7] N. Li, F. Gaillard, *Appl. Catal. B.*, 88, 152–159, (2009).

[8] F. Gaillard, N. Li, *Catal. Today*, 146, 345–350, (2009).

[9] D. I. Kondarides, G. N. Papatheodorou, C. G. Vayenas, X. E. Verykios, Ber. *Bunsenges. Phys Chem*, 5, 707-720, (1993).

[10] J. Yi, I. V Yentekakis, C. G. Vayenas, *J. Catal.*, 148, 240–251, (1994).

[11] S. Ladas, S. Kennou, S. Bebelis, C. G. Vayenas, *J. Phys. Chem.*, 97, 8845–8848, (1993).

[12] D. Tsiplakides, C. G. Vayenas, *J. Catal.*, 251, 237–251, (1999).

[13] C. Henriquesa, M. F. Portelaa, C. Mazzocchiab, *New Developments in Selective Oxidation II*, 499–506, (1994).

[14] P. Metcalf, P. Harriott, *Ind. Eng. Chem. Proccess Des. Develop.*, 11 (4), 478–484, (1972).

[15] N. Aoyama, K. Yoshida, A. Abe, T. Miyadera, *Catal. Let.*, 43, 249–253, (1997).

[16] D. R. Lowde, J. O. Williams, B. D. McNicol, *Appl. Surf. Sci.*, 1, 215–240, (1978).

[17] C. G. Vayenas, A. Ioannides, S. Bebelis, *J. Catal.*, 129, 67–87, (1991).

[18] S. S. Abd El Rehim, H. H. Hassan, M. A. M. Ibrahim, M. A. Amin, *Monatshefte fuer Chemie/Chemical Monthly*, 129, 1103–1117, (1998).

[19] P. G. Bruce, D. D. Macdonal, J. W. Tomlinson, *Electrochim. Acta*, 25, 563–573, (1980).

[20] M. Hepel, *J. Electrochem. Soc.*, 131, 1288, (1984).

[21] M. Fleishmann, D.J. Lax, H.R. Thirsk, Trans. Faraday Soc., 64, 3128 , 3128–3136, (1968).

[22] M. L. Teijelo, J. R. Vilche, A. Arvia, *J. of Electroanal. Chem.*, 131, 331–339, (1982).

[23] R. Giles, J. Harrison, *J. of Electroanal. Chem.*, 27, 161–163, (1970).

[24] J. Droog, P. Alderliesten, G. Bootsma, *J. of Electroanal. Chem.*, 99, 173–186, (1979).

[25] G. T. N. Burstein, R. C. Newman, *Electrochim. Acta*, 25, 1009–1013, (1980).

[26] S. Souentie, C. Falgairette, C. Comninellis, *J. Electrochem. Soc.*, 157, P49, (2010).

[27] F. M. Sapountzi, F. Dorado, S. Souentie, J. L. Valverde, in *7th international conference on environmental catalysis*, Lyon, France,2012, pp. 7–8.

[28] C. Falgairette, G. Fóti, *Catal. Today*, 146, 274–278, (2009).

[29] C. Falgairette, thesis, (2010).

[30] G. Fóti, A. Jaccoud, C. Falgairette, C. Comninellis, *J. Electroceram.*, 23, 175–179, (2007).

[31] A. Jaccoud, C. Falgairette, G. Foti, C. Comninellis, *Electrochim. Acta*, 52, 7927–7935, (2007).

Chapter 7 Summary of Conclusions

The objective of this work was to develop silver nickel and copper film electrodes interfaced with YSZ pellets, with controlled morphology and perform electrochemical characterization of the behaviour of these materials under polarization using cyclic voltammetry.

The work presented in this report appears in three major sections.

1. Synthesis of YSZ pellets (Chapter 3)
2. Synthesis and electrochemical characterization with cyclic voltammetry (Chapters 4-6)

The findings are summarized below.

PART 1: Synthesis of YSZ pellets

The objective of this chapter was to develop polycrystalline YSZ pellets with high densification and conductivity comparable to that found in literature. A sample of commercially produced sample was also used for comparison. Densification of greater than 98% was defined as an acceptable criterion for YSZ pellets used in EPOC studies [1–4]. Ionic conductivity was determined using electrochemical impedance spectroscopy (EIS) with frequency of 1 Hz to 100 kHz to evaluate grain boundary and bulk conductivities. These measurements were performed in air at temperatures of 300-400°C and values extrapolated to 1000°C to match literature values available for solid oxide fuel studies as literature data was unavailable at the temperatures of interest.

Pellets were produced from pressed and sintered 8 mol% YSZ (TOSOH) according to the process outlined by Gibson *et al.* [5]. The resulting pellets had average densification of 98.74 ± 0.002 % which was within the acceptable range, but lower than was found for commercially

produced pellet with densification of 100.000 ± 0.001%. This discrepancy is thought to be caused by the presence of sintering aids in the commercially produced pellet. The ionic conductivity of lab-produced pellets were comparable for those reported in the literature for similarly prepared pellets at 1000°C, at 10 μS cm^{-1} and 16 μS cm^{-1} respectively. Both conductivities were significantly smaller than those found for commercially produced pellet with ionic conductivity of 32 μS cm^{-1}.

PART 2: Electrochemical characterization using cyclic voltammetry

i. Nickel thin films

Nickel was selected as a material based on electrochemical and catalytic activity, high electrical conductivity and due to the existence of a model developed for sintered 880 nm film by Souentie *et al.*. The percolation threshold of nickel on YSZ was found to be 3.0±0.5 nm using i*n-situ* resistance measurements and so thin films of 50 nm and 100 nm were investigated in this work.

Oxidation of nickel in the literature both anodically in aqueous medium as well as chemically over a wide range of temperatures is well studied. Nickel is found to oxidize chemically and anodically to NiO, forming a compact stoichiometric scale. With higher potentials, electrochemically formed Ni^{3+} in the form of Ni_2O_3 is reported in aqueous medium.

In the model proposed by Souentie *et al.* [6], positive polarization causes NiO to form along the interface of YSZ and metal film, as shown in Figure 7.1 according to a parabolic rate expression consistent with Wagner's law.

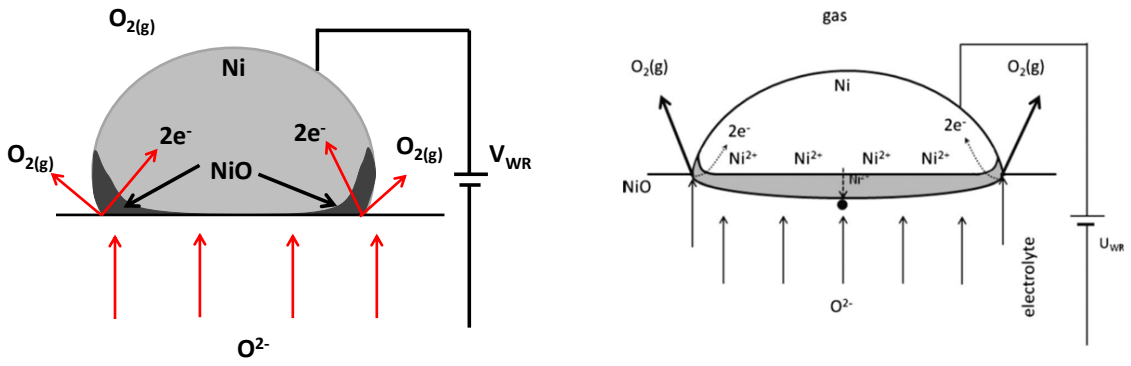

Figure 7.1 Proposed models for 50 nm evaporated nickel films and 880 nm sputtered nickel films [6]

Investigation of 50 nm nickel films found the oxides to form primarily at the three phase boundary according to a logarithmic rate expression consistent with Mott and Cabrera model for oxides smaller than 20 nm. With hold time at positive potentials, anodically formed oxides at the three phase boundary, the current efficiency decreased and the oxygen evolution reaction is favored. At 100 nm, oxides form both at the three phase boundary and along the Ni-YSZ interface, following neither parabolic nor logarithmic growth rates.

ii. Copper

Copper has high electronic conductivity and good catalytic activity. At elevated temperatures, Cu_2O forms spontaneous and thus electrochemical measurements are distorted by ohmic losses resulting from lower conductivity of the oxide. The percolation threshold of copper was found to be 5.0 ± 1.0 nm and so films of 50 nm and 100 nm were determined suitable for investigation. Preliminary cyclic voltammetry tests showed 50 nm copper films are not suitable for polarization due to a high ohmic loss associated with oxidation of the film. The 100 nm copper film show peaks associated with the reduction and oxidation of Cu_2O and CuO. At positive potentials, the film is oxidized to CuO at the three phase boundary, as shown in Figure

7.2, wherein it undergoes reduction first to Cu_2O and then subsequently to Cu according to a logarithmic growth rate expression. The peak associated with the reduction of Cu_2O to Cu is larger and so results in part from the reduction of native oxides. In addition to this, the copper thin films have poor chemical stability and function degrades rapidly over time.

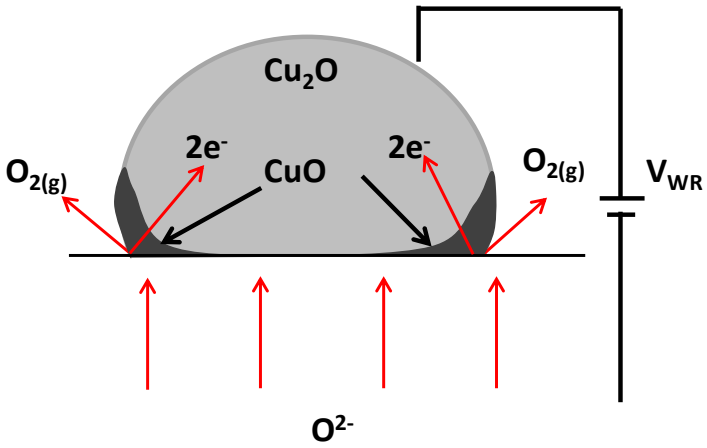

Figure 7.2 Model for 100 nm copper film

Control over the oxide state of copper is possible with polarization, but the low electronic conductivity of the native oxides under operating conditions make it an unfavorable option for electrochemical promotion.

iii. Silver

Silver was selected due to its high electronic conductivity and history as an electrochemically promotable substance. The percolation threshold was determined experimentally to be 5.4±0.4 nm. Despite this, preliminary tests demonstrated silver to be thermally unstable at 350°C, dewetting to form 1-2 μm isolated islands. The dependence of film thickness on the thermal stability of silver films was determined using insitu resistance measurements. Films of 600 nm or greater proved stable for 49.5h at 350°C under dilute oxygen

in helium gas mixture (P_{O2}=6 kPa). An 800 nm film was synthesized for electrochemical characterization.

At 350°C silver oxides are not thermodynamically stable, so the film is expected to be silver metal under operating conditions. With anodic polarization, the silver forms Ag_2O, first along the three phase boundary and then extends within the bulk of the electrode, as shown in Figure 7.3. The oxide forms according to a parabolic rate expression, but extended polarization results in reduced current efficiencies for subsequent oxide formation and the evolution of oxide is favored.

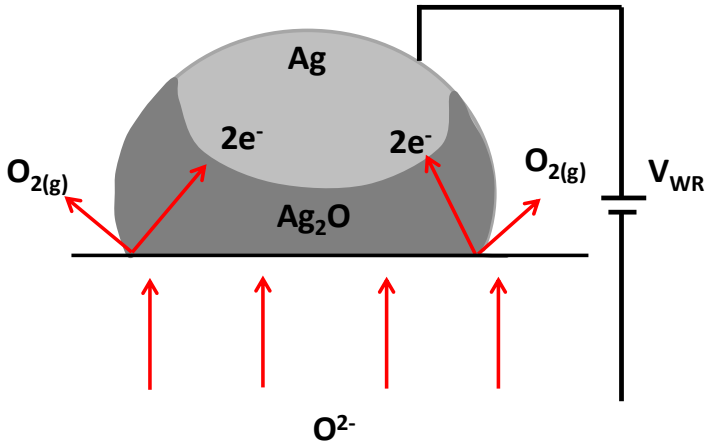

Figure 7.3 Model for oxide formation on 800 nm silver film

This behavior makes silver suitable for electrochemical promotion, but the thickness dependence of the thermal stability makes it impractical for industrial application without stabilization.

7.1 **References**

[1] P. Vernoux, F. Gaillard, R. Karoum, a. Billard, *Appl. Catal. B.*, 73, 73–83, (2007).

[2] B. Béguin, F. Gaillard, M. Primet, P. Vernoux, L. Bultel, M. Hénault, C. Roux, E. Siebert, *Ionics*, 8, 128–135, (2002).

[3] P. Vernoux, *J. Catal.*, 208, 412–421, (2002).

[4] A. Billard, P. Vernoux, *Top. Catal.*, 44, 369–377, (2007).

[5] I. R. Gibson, G. P. Dransfield, *J. Mat. Sci.*, 33, 4297–4305, (1998).

[6] S. Souentie, C. Falgairette, C. Comninellis, *J. Electrochem. Soc.*, 157, P49, (2010).